Electron Microscopical Investigations of Organic Solar Cells

Zur Erlangung des akademischen Grades eines
Doktors der Naturwissenschaften
von der Fakultät für Physik
des Karlsruher Instituts für Technologie (KIT)

genehmigte
Dissertation
von

Dipl.- Phys. Marina Pfaff

aus Kirchheim-Bolanden

Tag der mündlichen Prüfung: 15.11.2013

Referentin: Prof. Dr. D. Gerthsen
Korreferent: Prof. Dr. U. Lemmer

angefertigt am
Laboratorium für Elektronenmikroskopie
Karlsruher Institut für Technologie (KIT)

Contents

Preface

Renewable energies gained a lot in importance the last years. Worldwide the ecological awareness increases and much effort is put into projects to slow down the global warming and to prevent negative impacts with respect to the climate change. Furthermore the increasing scarcity of fossil fuels and the associated rising prizes force governments to think about alternatives for energy supply. Apart from hydro and wind power, solar power is the most important renewable energy technology. Worldwide photovoltaic systems with a capacity of 30 GW_p were newly installed in 2012, resulting in a global capacity of 102 GW_p [1]. Although this growth rate is impressive it is still by far not enough to reduce the carbon dioxide emissions because China and India alone are building four coal power plants every week [2]. Therefore it is essential to develop more efficient and cheaper solar cells to make them more attractive not only for industrial countries but also for newly industrializing economies.
Organic photovoltaics bear the potential of low-cost production. This is due to the fact that organic solar cells can be processed from solution and printed by roll-to-roll techniques with a high throughput and low material consumption [3]. In contrast to inorganic solar cells high temperatures are not needed for the fabrication. Thus, the energy consumption is significantly reduced, which results in lower costs and a better energy balance of the solar cells. Another advantage of organic photovoltaics is that the devices can be built on flexible and lightweight substrates, enabling new fields of applications.
The first heterojunction organic solar cell was already built in 1986 by C. W. Tang exhibiting a power conversion efficiency of 1 % [4]. Extensive international research on organic solar cells started after the developement of the bulk heterojunction (BHJ) concept in 1995 by Yu et al. [5] and Halls et al. [6]. Since then great success has been achieved concerning not only the efficiencies of the organic solar cells, but also the long-term stability of the devices and large-scale production techniques. The current efficiency record of 12 % was set by Heliatek in January 2013 [7].
The efficiency of BHJ organic solar cells is strongly correlated with the morphology of the absorber layer, which necessitates an optimized distribution of the donor and acceptor phases. A large interface between donor and acceptor components is required to efficiently dissociate photon-generated excitons into electrons and holes. On the other hand continuous conduction paths are necessary to transport the charges to the respective electrodes. The nanomorphology depends thereby on the tendency of the organic molecules to self-assemble, to crystallize and to phase separate. These properties can be influenced by changing the process conditions, for example the choice of the solvent, deposition temperature, the control of the drying kinetics and thermal post-treatment.
To control the influence of the fabrication parameters and to develop a fundamental understanding of the correlation between nanomorphology and efficiency of an organic solar cell, the application of electron microscopy is well suited. Transmission electron microscopy (TEM) cannot only be used for real-space imaging, it can also be applied to investigate the crystalline structure of a sample by electron diffraction or

dark-field (DF) imaging. However, TEM analysis is hampered by limitations such as electron radiation damage and especially poor contrast for samples containing materials that consist of light elements with only small variations in density. To overcome these problems low-energy scanning transmission electron microscopy (low-keV STEM) was applied in this work for nanomorphology investigations. Lowering the electron energy to values below 30 keV leads to a significant contrast enhancement and minimized knock-on damage caused by electron irradiation. Furthermore the use of a high-angle annular dark-field (HAADF) STEM detector provides images with a high atomic number contrast. In the course of this work low-keV HAADF STEM was used for the first time to investigate the nanomorphology of organic solar cell absorber layers. Since the contrast in the images is not intuitively interpretable a semi-empirical equation was developed to calculate the image intensity for different materials. It turned out that this equation can also be used to determine either the thickness or the density of a sample.

Another possibility to overcome the problem of poor contrast is the use of analytical methods like electron energy loss spectroscopy (EELS) and plasmon-loss energy-filtered transmission electron microscopy (EFTEM). Here, the image intensity is mainly determined by the electronic structure of the sample materials.

All standard TEM-based techniques only provide a two-dimensional projection of the examined volume. This limitation can be overcome by TEM tomography which facilitates the reconstruction of the three-dimensional sample structure.

Based on the application of different electron microscopy techniques a complete micro- and nanostructure analysis of organic absorber layers could be achieved.

In the course of this work four different material systems were investigated. Besides of organic solar cells based on the well-known donor polymer poly(3-hexylthiophene-2,5-diyl) (P3HT), and its selenium equivalent poly(3-hexylselenophene-2,5-diyl) (P3HS), absorber layers based on the new donor copolymer poly[*N*-9'-heptadecanyl-2,7-carbazole-*alt*-5,5-(4',7'-di-2-thienyl-2'-(3,5-difluoro-4-octyldodecyloxyphenyl)- 2'*H*-benzotriazole)] (PCDTPBt) and the small molecule donor material fluorenyl hexa-*peri*-hexabenzocoronene (FHBC) were investigated. As acceptor materials the fullerene derivatives [6,6]-phenyl-C_{61}-butyric acid methyl ester ($PC_{61}BM$) and [6,6]-phenyl-C_{71}-butyric acid methyl ester ($PC_{71}BM$) were applied. For all four material systems a correlation was established between the nanomorphology, the production parameters and optoelectronic properties.

The present work is composed of seven parts. In Chapter 1 the fundamentals of organic solar cells are outlined. In the following chapter an overview on the applied methods is given, including the current state of research. In Chapter 3 a semi-empirical formalism is developed which describes high-angle electron scattering at low electron energies in carbon-based materials. Moreover the applications of this formalism are presented.

In Chapter 4 the investigation of P3HT:$PC_{61}BM$ absorber layers of organic solar cells by low-keV STEM is presented. In the following chapter the nanomorphology of P3HS:$PC_{61}BM$ absorber layers is explored and correlated with the solar cell efficiency. In Chapter 6 organic solar cells based on the donor material PCDTPBt are investigated, whereby the findings from the electron microscopical investigations are used to further increase the performance of the organic solar cells. In the last chapter a complete micro- and nanostructure analysis of FHBC:$PC_{61}BM$ absorber layers is presented.

1 Fundamentals of organic solar cells

In this chapter the working principle of organic solar cells will be outlined. The materials investigated in this work and the different solar cell device architectures are presented. Finally, the different influences on the nanomorphology of the absorber layers are described and the current state of research on the investigated material systems is outlined.

1.1 Working principle

1.1.1 Conducting polymers

In general polymers have a low electrical conductivity and are considered as isolators. However, in 1977 H. Shirakawa, A. G. MacDiarmid and A. J. Heeger made a groundbreaking discovery, which was honored in 2000 with the Nobel Prize in chemistry [8]. They found out that the conductivity of polyacetylene films could be increased markedly by oxidating them with chlorine, bromine or iodine vapor [9]. For iodine the measured conductivity increased over seven orders of magnitude. This halogenation process was called 'doping' in analogy to the doping of semiconductors.

The physical basis of the electrical conductivity of polymers are conjugated double bonds which are alternating single and double bonds [10]. The electron orbitals of the carbon atoms in the conjugated double bonds are hybridized which means that one atom has three planar sp^2 orbitals and one vertical p_z orbital. Due to the overlap of the sp^2 orbitals strongly localized σ bonds are formed which are responsible for the binding of the atoms. The overlapping p_z orbitals cause a π bond. It is strongly delocalized, so that energy bands are formed over long polymer chains [11]. A schematic illustration a the double bond between two carbon atoms is displayed in Fig. 1.1.

The longer a polymer chain is, the more p_z orbitals contribute to the π electron band which causes a splitting of the energy eigenvalues into a quasi-continuous energy band [3]. In Fig. 1.2 the π orbital energy splitting is illustrated. In a non-excited molecule, the electrons will occupy the energetically lowest states. Important energy values to characterize an organic semiconductor are the highest occupied molecular orbital (HOMO) and the lowest unoccupied molecular orbital (LUMO) (Fig. 1.2). These terms can be related to the valence and conducting band in inorganic semiconductors.

The energy gap between the HOMO and the LUMO is typically in the range of 1.5-3 eV, thus electrons can be excited by visible and near ultraviolet (UV) light [12]. The excitation process results in the creation of a Frenkel exciton which is a bounded state of an electron and a hole. Due to the small permittivity, the Coulomb attraction between the charge carriers has a longer range in organic than in inorganic semiconductors. Furthermore the exciton is stronger localized on the molecular site [13] and, therefore, the binding energy of a Frenkel exciton is very high and lies between 0.3-1.4 eV [14, 15]. Internal electric fields are usually not strong enough to cause exciton dissociation [13]. Hence, the separation of electron and hole is only possible if one of the charge carrier can attain an energetically more favorable state. This can be realized by donor-acceptor transitions, which will be described in detail in the next section.

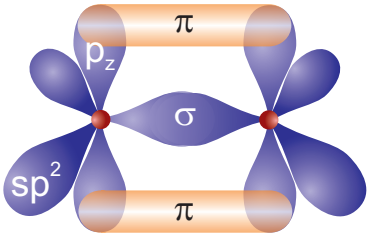

Figure 1.1: Scheme of the double bond of two carbon atoms with a localized σ bond between the sp^2 orbitals and delocalized π bonds between the p_z orbitals.

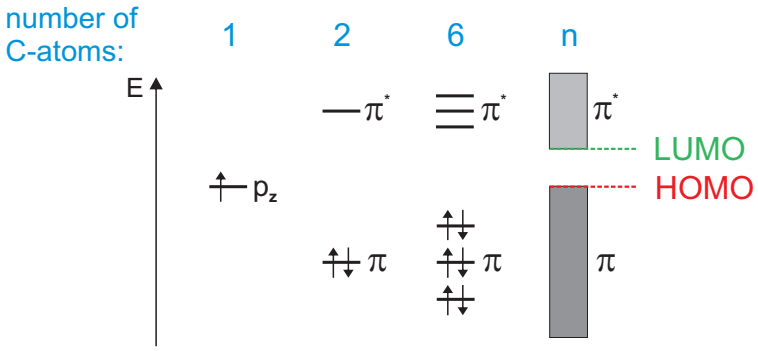

Figure 1.2: Scheme of the π orbital energy splitting for different numbers of bonded carbon atoms (not to scale). For a high number of adjacent atoms quasi-continuous energy bands are formed.

1.1.2 Bulk heterojunction

In organic semiconductors a donor-acceptor interface is needed for an exciton dissociation. In Fig. 1.3 the four consecutive steps in the generation of photo current from incident light are illustrated. An incident photon excites an electron into the LUMO of the donor, while a hole is created in the HOMO. The exciton then diffuses through the sample and if it reaches a donor-acceptor interface within its lifetime, the charges can be separated. The electron is thereby transfered from the LUMO of the donor into the energetically lower LUMO of the acceptor, while the hole stays in the HOMO of the donor. The charges are then transported to the respective electrodes. This happens mostly by hopping processes rather than by band conduction (like in inorganic semiconductors) [17]. Thus the charge carrier mobility is several orders of magnitude smaller than in inorganic semiconductors [18].

The exciton diffusion-length L_{ED} is in the range of 5-30 nm [19]. To ensure that all excitons in the absorber layer reach a donor-acceptor interface within their lifetime a special design of the absorber layer is necessary. In Fig. 1.4a the ideal donor-acceptor arrangement is displayed: the domain size is in the range of twice the exciton diffusion-length, the interface between the two materials is maximized and all domains connect to the respective electrode.

In 1995 Yu et al. and Halls et al. developed the so-called bulk heterojunction (BHJ) structure [5, 6]. For this structure the donor an acceptor materials are mixed and dissolved. The solution is then spincast onto the substrate. During the drying process the two materials segregate and domains are formed. An schematic illustration of a BHJ is displayed in Fig. 1.4b. In contrast to the ideal absorber layer structure it exhibits undesired features (marked with arrows in Fig. 1.4b). If an exciton is created in a

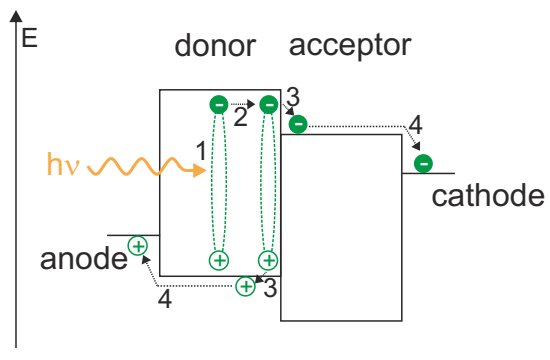

Figure 1.3: Schematic illustration of the four consecutive steps in the generation of photo current from incident light: (1) Photon absorption with formation of exciton; (2) Exciton diffusion to donor-acceptor interface; (3) charge-transfer of the electron to the LUMO of the acceptor; (4) Collection of the charge carriers at the electrodes.
(Figure is based on [16])

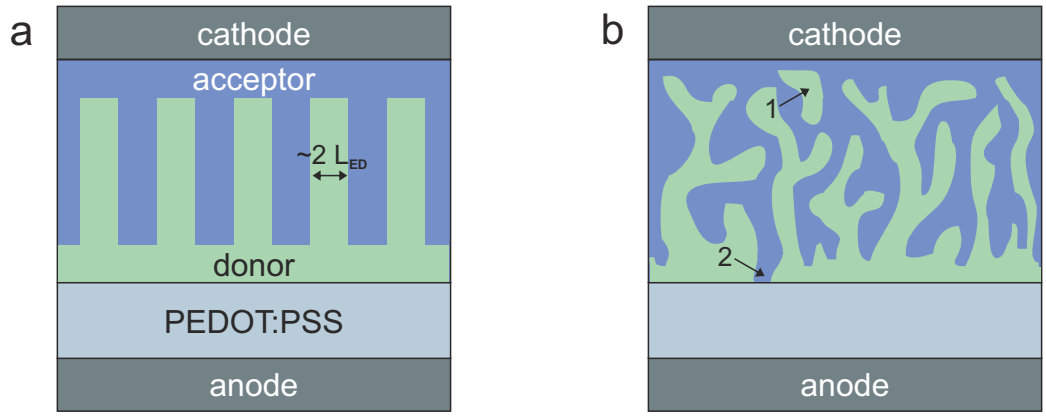

Figure 1.4: Schematic illustration of a) an ideal absorber layer structure and b) a bulk heterojunction (BHJ) with two undesired features marked with arrows: 1) an island without connection to the electrode and 2) a short-circuit between the electrodes.

domain without connection to the electrodes, the charges cannot be transported to the respective electrodes after dissociation and therefore do not contribute to the power generation. If a domain forms an interconnection between both electrodes, charge carriers can reach the wrong electrode and recombine with an opposite charge carrier [20]. These recombination losses reduce the short-circuit current (Chapter 1.1.3) and, therefore, the overall device performance.
As a result, the nanomorphology has to be optimized with respect to size, shape and distribution of the domains, to maximize the solar cell efficiency. This is usually realized by the variation of production parameters, e.g., the choice of the solvent or the drying conditions. The relation between production parameters, nanomorphology and solar cell efficiency will be discussed in detail in Chapter 1.4.

1.1.3 Solar cell key parameters

An important parameter to describe the quality of a solar cell is the external quantum efficiency η_{EQE}. It indicates the number of created charge carriers per incident photon and can be described by the following equation

$$\eta_{\mathrm{EQE}} = \eta_{\mathrm{A}} \cdot \eta_{\mathrm{ED}} \cdot \eta_{\mathrm{CT}} \cdot \eta_{\mathrm{CC}}. \tag{1.1}$$

The parameter η_{A} stands for the photon-absorption efficiency. If the organic absorber layer is thicker than the optical absorption length (≈100 nm), almost all photons are absorbed. This leads to an absorption efficiency of η_{A}=100 % [16]. η_{ED} stands for the efficiency of the exciton diffusion, i.e., for the fraction of excitons that reach an donor-acceptor interface within their lifetime. This efficiency strongly depends on the morphology of the absorber layer, which will be discussed in detail in Chapter 1.4. η_{CT} is the charge-transfer efficiency. It denotes the probability that an exciton is dissociated into an electron and a hole at the donor-acceptor interface. This process occurs very fast (typically in a few hundred femtoseconds), so that it happens before all other competing processes. Therefore η_{CT} can also be assumed to be 100 % [16]. η_{CC} stands for the charge-collection efficiency of the electrodes. It is typically high (≈100 %), due to the built-in electric field [16].

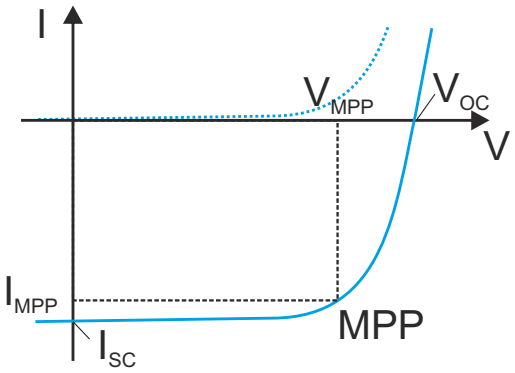

Figure 1.5: Current-voltage characteristic of an illuminated (full line) and an unilluminated (dashed line) solar cell.

The last three factors of Eq. 1.1 are often combined to the internal quantum efficiency η_{IQE}. It denotes the number of charge carriers leaving the cell over the electrodes with respect to the number of absorbed photons.

Considering influences on the external quantum efficiency, it becomes apparent that the optimization of η_{ED} is the main target in the improvement of organic solar cells. Park et al. first succeeded in fabricating a BHJ organic solar cell with a internal quantum efficiency close to 100 %, while the power-conversion efficiency (PCE) was 6.1 % for these devices [21].

The PCE η of a solar cell can be calculated by the fraction of the power generated by the solar cell P_{SC} and the incoming light power P_{Light}:

$$\eta = \frac{P_{\mathrm{SC}}}{P_{\mathrm{Light}}} = \frac{V_{\mathrm{MPP}} \cdot I_{\mathrm{MPP}}}{P_{\mathrm{Light}}} = \frac{FF \cdot V_{\mathrm{OC}} \cdot I_{\mathrm{SC}}}{P_{\mathrm{Light}}}. \tag{1.2}$$

V_{MPP} and I_{MPP} stand for the voltage and current at the maximum power point (MPP), which is marked in the current-voltage characteristic in Fig. 1.5. V_{OC} denotes the open-circuit voltage. It is mainly determined by the difference between the LUMO level of the acceptor and the HOMO level of the donor [22]. I_{SC} denotes the short-circuit current. It is determined by the amount of absorbed light and the internal conversion efficiency [23] which is directly related to the nanomorphology of the absorber layer. The fill factor FF is defined as:

$$FF = \frac{V_{\mathrm{MPP}} \cdot I_{\mathrm{MPP}}}{V_{\mathrm{OC}} \cdot I_{\mathrm{SC}}}. \tag{1.3}$$

It is a measure of how well the maximum power rectangle fits under the characteristic curve [24].

For the comparability of PCEs it is important to specify the exact measurement conditions. Normalized reference spectra are needed, since the absorption and, therefore, the external quantum efficiency η_{EQE} is a function of the wavelength of the incident light. Thus, the PCE depends on the type of incident spectrum. The most commonly used reference spectra are the 'air mass (AM)' spectra of the American Society for Testing and Material Standards (ASTM) [25]. These spectra consider the path of the sunrays through the atmosphere. According to the ASTM standard the light power per area is 1000 W/m^2.

1.2 Materials

1.2.1 Donors

In organic solar cells different kinds of organic semiconductors are applied as donor materials. A distinction is made between polymers, copolymers and small molecules. Representative of all these groups were investigated in this work.

Polymers

Polymers are chemical compounds which consist of long chains of identical single units. They are usually well suited for solution-processing, whereby the side chains are responsible for the solubility.

The semiconducting polymers investigated in this work are poly(3-hexylthiophene-2,5-diyl) (P3HT) and poly(3-hexylselenophene-2,5-diyl) (P3HS), shown in Fig. 1.6 which belong to the group of the polythiophenes. They are characterized by a facile synthesis, many modification capabilities, high environmental/thermal stability [26]. Solar cells based on these materials showed efficiencies of up to 5 %, demonstrated for example by Ma et al. for P3HT:[6,6]-phenyl-C_{61}-butyric acid methyl ester ($PC_{61}BM$) solar cells [27]. P3HT is the most studied donor semiconductor for organic photovoltaic and it often serves as reference material [26].

P3HT consists of an aromatic ring with one sulfur atom (thiophene) and an attached alkyl chain of carbon atoms (hexyl). This additional alkyl chain is responsible for the solubility in non-polar solvents. Charge transport is enabled by the four π electrons of the two double bonds and the two electrons of the sulfur p_z orbital. The coupling of the monomers can occur in different ways, depending on the production process. The most favorable configuration is the head-to-tail coupling [26]. The percentage of these couplings is called regioregularity (RR). The greater the RR, the better is the optical absorption and the field-effect mobility [28]. Another important influence on the performance of the solar cell is the molecular weight of the polymer which will be discussed in detail in Chapter 1.4.1.

The polymer P3HS is the selenium equivalent of P3HT. It exhibits a reduced optical band gap due to a deeper LUMO energy level resulting from a smaller ionization potential of selenium compared to sulfur [29]. The best P3HS:$PC_{61}BM$ cells up to now were fabricated by Ballantyne et al. [30]. They showed a PCE of 2.7 %. Although this value is relatively low compared to P3HT cells, it has to be noted that the short-circuit current was significantly increased. Since the open-circuit voltage was the same as for the P3HT reference sample, the lower PCE could be completely attributed to the low FF, which in turn is caused by an non-optimized morphology. This implies that P3HS as donor material still bears the potential for high efficiency solar cells [30].

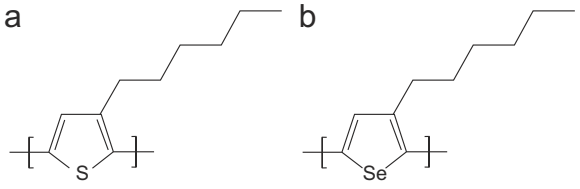

Figure 1.6: a) P3HT and b) its selenium equivalent P3HS.

Copolymers

A copolymer is a polymer composed of two different (or more) monomers. In organic photovoltaics so-called donor-acceptor compounds are applied. It was shown that by the combination of electron-poor (accepting) and electron-rich (donating) monomers the distance between the HOMO and the LUMO level can be reduced to shift the absorption edge toward lower energies [31].
The copolymer investigated in this study, belongs to the group of donor-acceptor compounds that contain a functionalized carbazole as donor unit. High efficiencies of up to 6.8 % could be achieved for different members of this group [32]. The copolymer examined in this work contains a phenylbenzotriazole as acceptor unit. It is called poly[*N*-9'-heptadecanyl-2,7-carbazole-*alt*-5,5-(4',7'-di-2-thienyl-2'- (3,5-difluoro-4-octyldode-cyloxyphenyl)-2'*H*-benzotriazole)] PCDTPBt. The molecule is displayed in Fig. 1.7. It was firstly synthesized by F. Pasker [33] who also provided the material for the nanomorphology investigations described in Chapter 6.

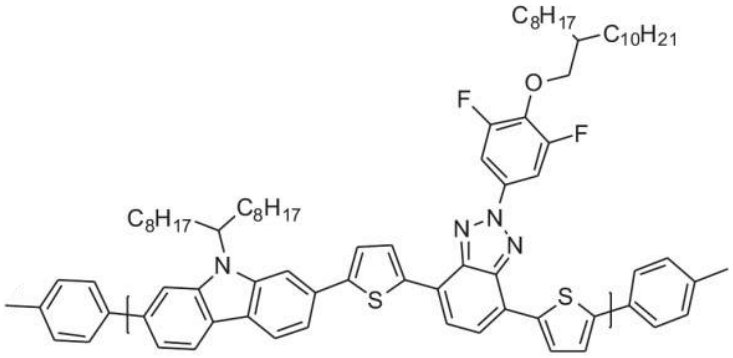

Figure 1.7: PCDTPBt molecule.

Small molecules

Small molecules applied in organic photovoltaics, exhibit a conjugated π electron system, like the already described semiconducting polymers. In contrast to polymers small molecules can be evaporated [34]. In solution-processed solar cells, small molecules with designated side groups are applied.
The small molecule investigated in this work is fluorenyl hexa-*peri*-hexabenzocoronene (FHBC), a planar aromatic molecule, which consist of a hexa-*peri*-hexabenzocoronene (HBC) core with flourenyl and alkyl side groups [35]. In Fig. 1.8 the FHBC molecule is displayed. HBC is a discotic polycyclic aromatic hydrocarbon with well-known liquid crystalline properties as a result of strong intermolecular association between the

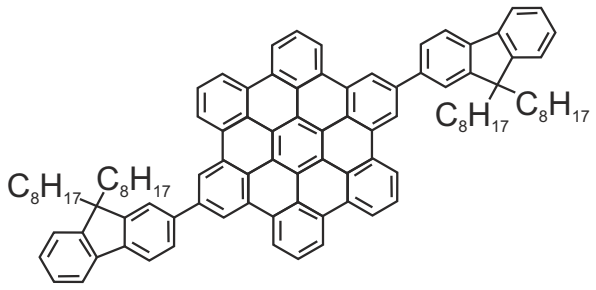

Figure 1.8: FHBC molecule.

molecules [35] The columnar stacking results in high intrinsic charge transport properties making HBC materials attractive for semi-conducting applications [35]. While photovoltaic response of HBC containing devices was first demonstrated in 2001 [36], the introduction of fluorene substituents on the HBC molecule resulted in a material that showed a promising device performance in combination with the fullerene electron acceptor $PC_{61}BM$ [35]. Despite the restricted spectral absorption of this FHBC material with absorption onset at 450 nm, PCEs of up to 1.5 % were recorded for FHBC:$PC_{61}BM$ devices with a maximum external quantum efficiency of 40 % at 400 nm [35]. Perhaps, the most interesting aspect of the device characteristics was the high fill factor FF of up to 65 %. The high FF value indicated that the transport of holes and electrons through the BHJ film is well-balanced, which was confirmed in charge mobility measurements [35, 37].

1.2.2 Acceptors

Fullerene derivatives are since their first application [5] the most frequently used acceptor materials in solution-processable organic solar cells [19]. Attempts to replace these derivatives by other electron-conduction materials, were rarely successful. This is due to the fact that fullerenes have many properties which are beneficial for the application in organic photovoltaics. They have for example a LUMO level that fits very well to the LUMO level of most conjugated polymers, which are used as donor materials [38]. Furthermore, fullerenes exhibit an ultrafast photoinduced electron transfer in combination with various conjugated polymers [39] and high electron mobilities of about 10^{-3} $cm^2/V{\cdot}s$ [40]. These mobilities are relatively isotropic due to the symmetry of the fullerene molecule [38].
To overcome the disadvantage of the low solubility of fullerenes, several derivatives have been developed. The most frequently used are $PC_{61}BM$ and [6,6]-phenyl-C_{71}-butyric acid methyl ester ($PC_{71}BM$). They are single isomers, synthesized by the addition of diazoalkane [41]. In Fig. 1.9 the fullerene derivatives $PC_{61}BM$ and $PC_{71}BM$ are presented, which are up to now the most common acceptor materials for organic solar cells.
While the LUMO levels of $PC_{61}BM$ and $PC_{71}BM$ are similar [42], the HOMO level of $PC_{71}BM$ (-5.9 eV [43]) is higher than the one of $PC_{61}BM$ (-6.1 eV [44]). The higher HOMO level of $PC_{71}BM$ can be related to a higher absorption coefficient at longer wavelengths [38, 45], which is related to the lower symmetry of the C_{70} molecule compared to the C_{60} fullerene [46]. Thus, solar cell devices comprising $PC_{71}BM$ usually exceed the ones with $PC_{61}BM$ in terms of the PCE and the I_{SC}. Nevertheless, $PC_{61}BM$ can be advantageous, due to the different solubility and therefore demixing behavior [46]. Last but not least $PC_{61}BM$ is less expensive than $PC_{71}BM$.

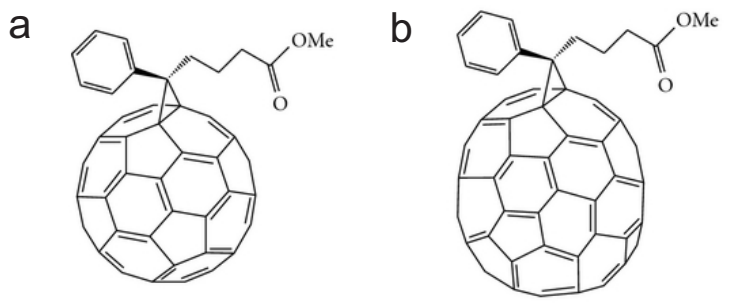

Figure 1.9:
the most frequently used acceptor materials in organic photovoltaics:
a) $PC_{61}BM$
b) $PC_{71}BM$.

1.3 Device architecture

The solar cells investigated in this work are based on two different device architectures, namely the standard and the inverted architecture, both displayed in Fig. 1.10. The difference between the two designs is the arrangement of the electrodes. In the standard architecture (Fig. 1.10a) the light enters the solar cell through the transparent anode, in the inverted architecture (Fig. 1.10b) through the transparent cathode. The charge carrier flux is correspondingly inverted.

The samples investigated in this work are mostly prepared on glass substrates, although it is also possible to use flexible materials like polyethylene terephthalate (PET). The substrate is for both designs covered with indium tin oxide (ITO) which belongs to the group of the transparent conductive oxides (TCOs). In the standard design it serves as anode, in the inverted architecture as cathode. Advantages of ITO are the low specific resistivity and the transparency in the visible spectrum [47].

In the standard architecture a hole-transport layer of poly(3,4-ethylenedioxythiophene): poly- styrenesulfonate (PEDOT:PSS) is deposited on the ITO anode. It serves as buffer and enhances the charge extraction from the absorber layer [48]. PEDOT:PSS is a p-doped material which has a high transparency for visible light. Furthermore it is water-soluble and exhibits a high conductivity [49]. The active layer is spincoated on top of the PEDOT:PSS layer. In an ideal BHJ solar cell the anode side of the absorber layer is donor- and the cathode side acceptor-rich (Chapter 1.1.2).

To extract efficiently the electrons from the photoactive layer, appropriate cathode materials have to be chosen. In the standard architecture metals with a low work function are applied. In this work calcium is used as cathode material. Since it oxidises very fast, a protection layer of aluminum is deposited on top of it [18]. Alternatively a combination of an electron-transport layer like TiO_x [50] and an aluminum anode can be applied.

In inverted solar cells it can be advantageous to cover the ITO by a transparent electron-transport layer. For this purpose the semiconductor ZnO was chosen in this work.

The next step in the fabrication of the solar cell is spin coating of the absorber layer.

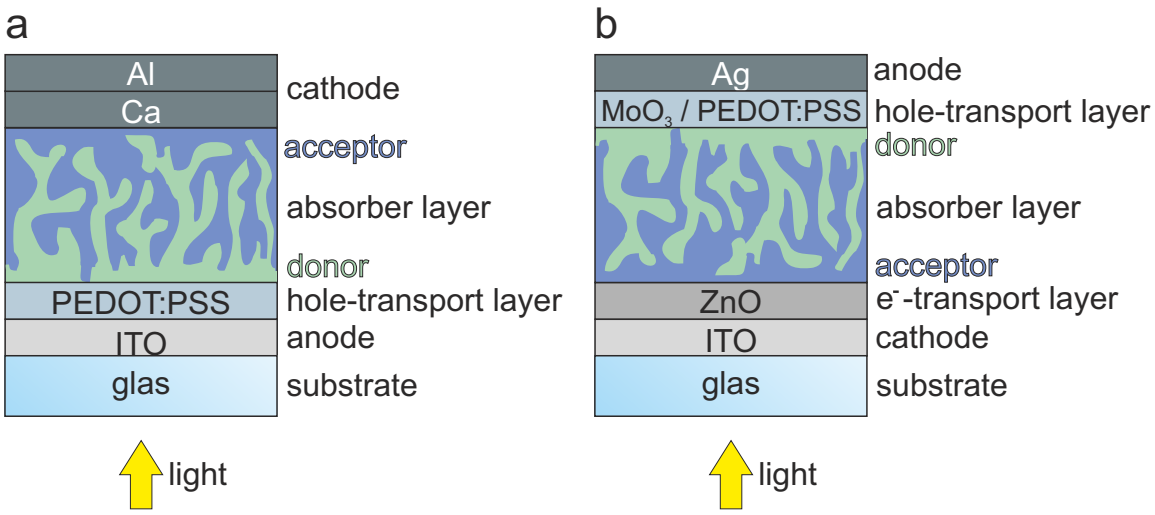

Figure 1.10: Schematic illustration of a) the standard and b) the inverted solar cell architecture.

On top of it a hole-transport layer is deposited. In this work inverted solar cells with hole-transport layers of either PEDOT:PSS or MoO_3 [51] are investigated. Silver is deposited as anode onto the hole-transport layer. With its high work function it is well suited to extract electrons [18].
Depending on the used donor and acceptor materials the standard or the inverted architecture can be more favorable. If for example the acceptor material shows a tendency to enrich at the bottom interface of the active layer the inverted architecture can result in a higher PCE [52].

1.4 Nanomorphology of absorber layers

As already mentioned, the nanomorphology of the absorber layer has a high impact on the performance of organic solar cells. Different influences on the nanomorphology and their correlation with the device performance are discussed in the following sections. Furthermore the current state of research concerning the investigated material systems is outlined.

1.4.1 Influence of material and fabrication parameters

Donor:acceptor mixing-ratio

An easy way to influence the nanomorphology is the variation of the mixing ratio of donor (D) and acceptor (A) material. The ideal D:A mixing ratio ranges from 1:0.7 to 1:4 for common polymer:fullerene blends [53]. Although the fullerene absorbs only a small fraction of the incoming light and a low content of about 5 % is sufficient for a complete exciton diffusion [54], a blend ratio of 1:4 can be necessary to form percolating paths to the electrodes [55].

Thermal annealing

Thermal annealing is a common method to modify the structure of the absorber layer by promoting phase separation and crystallization or aggregation of each component. It has the advantage that it can be applied independently of the film deposition technique [56].
In many organic photovoltaic (OPV) blend systems (like for example P3HT:$PC_{61}BM$) the crystallinity of the components and the degree of phase separation is relatively low after the spin coating process, which results in a low PCE. This is due to the fact that the drying process occurs typically very fast, so that the resulting nanomorphology is not in a thermodynamic equilibrium [53]. By heating the sample over the glass transition temperature T_g, the molecules can rearrange and crystallize. As a result an improvement of the long-wavelength absorption and charge-carrier mobility can be observed [53]. Furthermore a donor:acceptor structure with interconnected pathways to the electrodes is formed [56]. Many examples for a PCE-enhancing effect of annealing can be found in literature for various material systems (reviewed e.g. in [20, 53, 56])
In contrast, some OPV blends incorporating donor polymers with low degree of crystalline order (e.g. samples with MDMO-PPV[1] [57] or PCDTBT[2] [21]) do not show an

[1] poly(2-methoxy-5-(3'-7'-dimethyloctyloxy)-1,4-phenylenevinylene
[2] poly[N-9'-heptadecanyl-2,7-carbazole-*alt*-5,5-(4',7'-di-2-thienyl-2',1',3'-benzothiadiazole)]

improved device performance after annealing. Therefore other possibilities to change the nanomorphology like the choice of solvent or the blend composition have to be considered [53].

Solvent annealing

The so-called solvent annealing process is not an annealing in the proper meaning of the word, because no heating of the sample is involved. For a solvent annealing treatment the spin coating duration is kept short, so that the resulting deposited layer is still wet. The sample is then slowly dried under a Petri dish in solvent vapor [58]. In this saturated solvent atmosphere the polymers can reorganize and crystallize [53]. During a long drying process the system is approaching the structure of thermodynamical equilibrium. However, the ideal morphology does usually not correspond to the equilibrium state and has therefore to be found by elaborate experiments or on the basis of phase diagrams [59].
One advantage of solvent annealing compared to thermal annealing is its compatibility with devices fabricated onto flexible substrates that may degrade or warp at typical thermal annealing temperatures [53].

Molecular weight

The molecular weight (MW) can be either described by the number-average molecular weight M_{n}, which is just the arithmetic mean, or the weight-average molecular weight M_{w}. The latter can be found by choosing randomly monomers and determining the molar mass of the associated polymers. The mean value obtained by this procedure is then M_{w}. The two values are related to each other by the polydispersity index (PDI) which is defined as: $PDI = M_{\mathrm{w}}/M_{\mathrm{n}}$ and gives an indication for the width of the molecular weight distribution [60].
The MW and the PDI are important parameters to control electronic, optical and electrochemical properties of a polymer. Furthermore the two parameters have a high influence on the nanomorphology of the absorber layer and therefore the transport properties [26]. For many polymers applied in organic solar cells an improvement of device performance is observed for an increased MW [32]. This enhancement is attributed to a better light absorption in the UV-visible region and a more efficient hole transport along the polymer backbones [26, 32]. Nevertheless, in some cases a higher MW also lead to a decreased efficiency. This was attributed to the fact that higher MW fractions can posses a higher degree of entanglement, which hinder the carrier transport along one polymer chain and between different chains [32].

Choice of solvent

In solution processable photovoltaics the solvent has a high impact on the nanomorphology of the absorber layer. Depending on the choice of solvent phase separation and molecular self-organization can be either promoted or hindered [56]. Solvent properties, such as boiling point, vapor pressure, solubility, and polarity have an considerable impact on the final film morphology [20]. If for example a fast evaporating solvent is used, there is only a short time for demixing processes and a rearrangement of the molecules. As a result a very fine phase separation can be expected.

Processing additives

Processing additives are solvents that are mixed to a small percentage with the main solvent to change the drying kinetics of the film. They are commonly used for blends with low band-gap polymers for which thermal annealing often does not lead to an enhanced device performance [61].
The most effective approach is to use additive solvents with a selective solubility for one of the active layer components. An example is the use of 1,8-diiodooctane (DIO) which is usually mixed with chlorobenzene (CB) or 1,2-dichlorobenzene (DCB). It has a higher boiling point than the most host solvents and it is known to preferentially solubilize $PC_{61}BM$. Therefore the $PC_{61}BM$ stays longer in solution during the drying process than the donor polymer. Hence it has more time to reorganize which results in a BHJ structure with domain sizes in the range of the exciton diffusion length [62, 63]. For example, Lou et al. [64] reported a smaller domain size in blends of the low band-gap material PTB7[3] and $PC_{71}BM$ fabricated with DIO as processing additive. They concluded that the DIO selectively dissolves $PC_{71}BM$ aggregates and allows them to diffuse into the PTB7 domains. Therefore not only the domain size, but also the polymer-fullerene interface was optimized.

1.4.2 Current state of research

P3HT:PCBM blends

The highest PCEs could be obtained for P3HT:$PC_{61}BM$ solar cells with a mixing ratio of 1:0.8 [27]. However, it has to be noted that different information about the ideal mixing ratio of P3HT:$PC_{61}BM$ absorber layers can be found in literature. This is due to the fact that the binary phase diagram of P3HT:$PC_{61}BM$ blends exhibits an eutectic composition which depends on the molecular weight of the P3HT [65, 66]. While Müller et al. found that the optimum composition for device performance is slightly hypoeutectic when expressed in terms of the polymer component [65], Nicolet et al. stated that the eutectic composition yields optimal photovoltaic properties [66]. At this point an annealed and subsequently cooled down sample exhibits a finely intermixed structure, because the two materials of the blend solidified simultaneously. For a non-eutectic composition primary crystals of the majority component are formed during the cooling process, which in the end are surrounded by a matrix of both components [66].
It is well known that thermal annealing can significantly enhance the performance of P3HT:$PC_{61}BM$ solar cells. In experiments of Ma et al. annealing for 30 min at 150 °C increased the device performance from 0.28 % to 5.00 % [27]. It was found that high-MW P3HT requires longer annealing times at higher temperatures than low-MW P3HT to form an ideal BHJ structure. This was ascribed to the stronger degree of aggregation of the long polymer chains which prevent phase separation and diffusion of $PC_{61}BM$ molecules [26, 67].
High-MW P3HT-based organic solar cells exhibit in general a better device performance [26, 58]. The reason for this is not only the enhanced absorption due to the increased conjugation length of the polymer, but also the different crystallization behavior of high-MW P3HT. The charge carrier mobility increases significantly with the molecular

[3] Poly[[4,8-bis[(2-ethylhexyl)oxy]benzo[1,2-b:4,5-b']dithiophene-2,6-diyl][3-fluoro-2-[(2-ethylhexyl)carbonyl]thieno[3,4-b]thiophenediyl]]

weight of the P3HT. This is surprising since the crystallinity is much higher in low-MW P3HT films, due to highly crystalline P3HT nanorods [26, 68]. Hiorns et al. assigned the low charge carrier mobilities to the poor connectivity between the nanorods and insulating grain boundaries between misoriented neighboring crystals [67]. Although the crystalline regions are smaller in high-MW P3HT samples, their interconnectivity is improved due to the long polymer chains [68, 69].
The P3HT nanorods are formed by π-π stacking of the polymer chains [69, 70]. Thereby the backbones of the polymers are oriented perpendicular to the nanorod axis. Thus, the π-π stacking direction is parallel to the length of the nanorods. The width of such a nanorod is typically in the range of 15 nm which is significantly shorter than the average conjugation length of the P3HT chains. Therefore Ihn et al. concluded that the polymer chains are folded along the edges of the nanorods [71].
Besides of the formation of P3HT nanorods, some groups observe large $PC_{61}BM$ crystals upon annealing [72, 73]. The size of these crystals depends on the annealing time and temperature and ranges from several µm up to mm, leading to short circuits and, finally, destruction of the device.

P3HS:PCBM blends

For P3HS:$PC_{61}BM$ devices the highest efficiencies were found for a $PC_{61}BM$ content of 52 % [30] or 41 % [74]. The deviation between these two values can probably be attributed to the different MWs of the used P3HS. It was shown as expected that P3HS has similar properties like its thiophene analogon P3HT [30, 75]. X-ray diffraction (XRD) measurements revealed that P3HS also exhibits an improved π-π stacking upon annealing [30]. Furthermore the phase diagramm determined by differential scanning calorimetry (DSC) showed that P3HS:$PC_{61}BM$ blends display a simple eutectic phase behavior similar to that reported for the P3HT:$PC_{61}BM$ [75]. Lilliu et al. [76] examined pure P3HS and P3HS:$PC_{61}BM$ samples with grazing incident X-ray diffraction (GIXD) and found that the chrystalline structure was very similar to the one of P3HT. Furthermore a detailed analysis of the GIXD peaks revealed domain sizes of about 20 nm.
By combining various optical spectroscopy techniques such as optical microscopy, Raman, and fluorescence mapping Ballantyne et al. showed that P3HS:$PC_{61}BM$ blends exhibit a lower degree of polymer purity in the P3HS-rich domains than comparable devices fabricated of P3HT:$PC_{61}BM$ [75]. Optical spectroscopy was used in this work as well. With respect to the spacial resolution it is noted, that it is limited by the diffraction limit being two orders of magnitude lower than the resolution in electron microscopy. It is therefore not possible to image by optical spectroscopy the BHJ structure with typical domain sizes in the range of a few 10 nm.
Recently Tsoi et al. studied the nanomorphology of P3HS:$PC_{61}BM$ and P3HT:$PC_{61}BM$ films with Raman spectroscopy and observed that the replacement of the sulfur atom in P3HT by the heavier selenium atom increases the tendency of the molecules to form phases with improved order. However, the overall fraction of ordered phase is much lower in P3HS- than in P3HT-based films [77].
To analyze the miscibility of P3HS and several fullerene derivatives (including $PC_{61}BM$) Treat et al. investigated P3HS/fullerene bilayer samples by high-angle annular dark-field (HAADF) scanning transmission electron microscopy (STEM) at 300 keV [74].

The images of the annealed samples show a network of P3HS, similar to the structures observed in low-MW P3HT:$PC_{61}BM$ samples.

FHBC:PCBM blends

Experiments of Wong et al. revealed that solar cells with the small molecule FHBC as donor and $PC_{61}BM$ as acceptor show the highest efficiency for a mixing ratio of 1:2 [35, 78]. It was further demonstrated that thermal annealing at 150 °C for 15 s leads to an increased device performance. This was attributed to an increase in the domain size (investigated by atomic force microscopy (AFM)) and an improved crystallinity of the BHJ phases. Wide-angle X-ray scattering (WAXS) experiments were performed to gain insight in the molecular organization of pure FHBC, which shows a well ordered columnar discotic liquid crystalline organization of the molecules. The FHBC molecules self-assemble via π-π stacking into columnar stacks, which in turn arrange in a hexagonal arrangement. A scheme of this arrangement is displayed in Fig. 1.11.

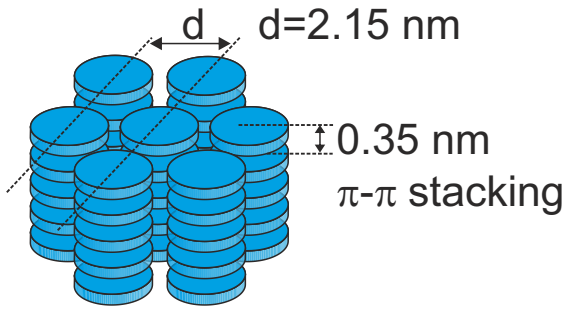

Figure 1.11: Hexagonal arrangement of the FHBC stacks which are formed by π-π stacking of the molecules.
(Fig. is based on [78])

2 Experimental techniques

In this chapter the methods and instruments applied in this work are described. First, the different sample preparation procedures are outlined, then the application of the electron microscopical techniques for the investigation of organic solar cell samples will be presented, including low-energy scanning transmission electron microscopy (low-keV STEM), transmission electron microscopy (TEM), energy-filtered transmission electron microscopy (EFTEM), electron energy loss spectroscopy (EELS) and electron tomography. In parallel the current state of research in the investigation of BHJ nanostructures with these techniques will be outlined.

2.1 Sample preparation for electron microscopy investigations

2.1.1 Plan-view samples

The easiest way to prepare electron transparent samples from an organic solar cell, is the direct lift-off of the absorber layer. This method takes advantage of the water solubility of the PEDOT:PSS layer, which is positioned underneath the absorber layer in a solar cell with standard design (Chapter 1.3). Since the evaporated metal electrodes cover only a part of the absorber layer (Fig. 2.1a), it is not necessary to remove them for the sample preparation. The absorber layer is cut with a scalpel into small squares. By dropping deionized water onto this position of the device, the PEDOT:PSS can be dissolved and the squares of the absorber layer float on the surface of the water droplet. By means of a wire loop (Fig. 2.1a) and by exploiting the surface tension of the water it is possible to pick up the squares and transfer them onto a transmission electron microscopy (TEM) copper grid (Fig. 2.1b). The TEM grids have a diameter of 3.05 mm and a mesh number of 150. After complete drying of the sample, the grid can be mounted into the sample holder of the microscope.
Besides the fact that this preparation method is fast and easy it has the advantage that the electron-microscopy sample can be taken from the original solar cell device (if it has a standard architecture). The disadvantage is that the sample thickness is predetermined by the thickness of the absorber layer. If thin samples are desired, the fabrication process has to be changed which in turn can have an effect on the nanomorphology of the absorber layer. Furthermore the images obtained from plan-view samples are always a projection along the thickness of the absorber layer which means that information about the vertical structure of the absorber layer cannot be obtained.

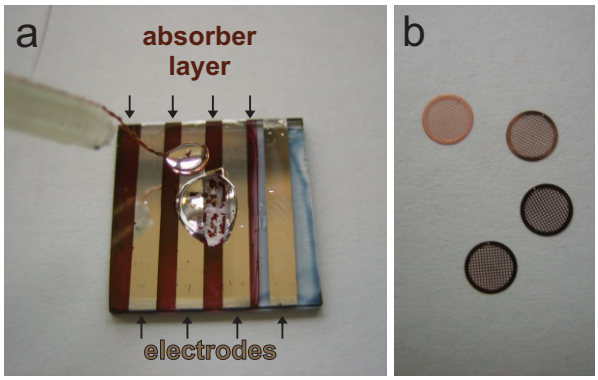

Figure 2.1: Plan-view sample preparation: a) Photo of a solar cell device with a water droplet on top which dissolves the PEDOT:PSS. A wire loop is used to pick up the floating pieces of the absorber layer and transfer them onto TEM grids, which are displayed in b).

2.1.2 Ultramicrotomy cross-section samples

To investigate the vertical structure of absorber layers cross-section samples have to be prepared. For this purpose ultramicrotomy was applied, where a sample is cut into thin sections with a diamond knife [79]. Since the glass substrate of the solar cells cannot be cut, pieces of the absorber layer were transferred onto a PET foil (similar to the plan view sample preparation in the previous section). The foil is subsequently embedded in two-component adhesive (Uhu Plus Endfest 300). The sample is then

oriented, so that the vertical direction of the absorber layer is perpendicular to the cutting direction. After pre-trimming the embedded sample with a glass knife into a pyramidal shape, the diamond knife can be applied to cut sections with thicknesses ≥50 nm. A scheme of the cutting process is displayed in Fig. 2.2. In the course of this work the wet sectioning technique was used. A water reservoir is attached to the diamond knife, so that the sections float on the water surface after the cutting process. Four to six sections are then arranged with an eyelash into a group on the water surface, before they are picked up with a small metal loop (similar to the wire loop described in the previous section). With this loop the sections are then transferred onto TEM grids lying on filter paper [79].

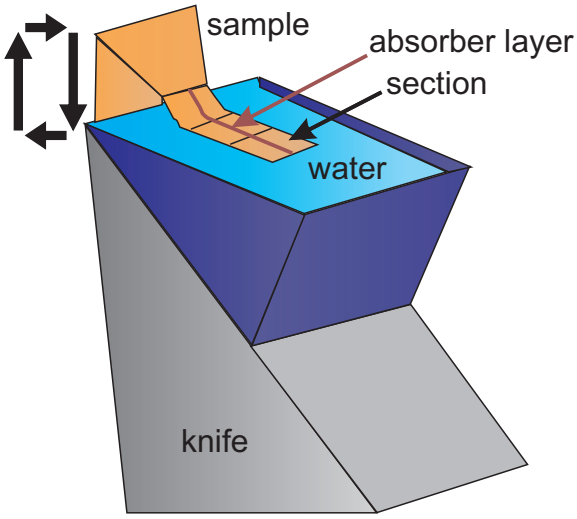

Figure 2.2: Working principle of the wet sectioning technique in ultramicrotomy.

2.1.3 Focused ion beam cross-section samples

Another common technique to prepare cross-sectional samples is the use of focused Ga^+-ion beams (FIB). In this work the FEI Dual Beam Strata 400S was used for sample preparation and thickness determination. It is a combination of a conventional scanning electron microscopy (SEM) system (described in detail in Chapter 2.2) and a FIB column which is installed under an angle of 52 ° with respect to the electron beam. The combination of these two systems has the advantage that the FIB process can be supervised using the SEM signals. In the FIB collumn Ga^+-ions are produced, accelerated and focused onto the sample surface. The beam can either be positioned on one spot or scanned over a larger sample area. The energy of the ions is typically between 2 and 30 keV. The ion current can be varied by choosing different apertures and ranges from 1 pA to over 20 nA [80]. A FIB system can be used for imaging, nanomilling or patterning by material deposition [81]. For the imaging mode the secondary electrons (SEs) generated by the ions are detected like in SEM [81, 82]. The nanomilling process is based on the fact that incident ions sputter atoms from the sample surface due to their high momentum transfer [82, 83]. For the deposition of material by FIB a precursor gas is inserted into the chamber close to the sample surface via a gas injection system (GIS). The gas is then decomposed by the ions, leaving behind the deposition material on the sample surface [81, 82].

TEM sample preparation

For the preparation of cross-section samples several elaborate milling and deposition steps are applied, which are presented in Fig. 2.3. After the deposition of a platinum protection layer and two markers, trenches are milled leaving behind a thin lamella (Fig. 2.3a). As a next step the sample is tilted and the lamella is cut free, except for two small bars. The micro manipulator needle is then connected to the lamella by depositing a small amount of platinum at the contact point (Fig. 2.3b). The remnant bars are also milled away, so that the lamella can be lifted out (Fig. 2.3c) and transferred to a dedicated copper sample-holder (Fig. 2.3d). (The bright large structure in the upper left corner of Fig. 2.3d is the GIS nozzle.) After connecting the lamella to the sample holder by deposition of platinum at the contact points, the manipulator needle can be cut off (Fig. 2.3e). Subsequently the lamella must be further trimmed, thinned and polished with the ion beam (Fig. 2.3f). Depending on the material, it is feasible to prepare samples with a thickness below 50 nm. Furthermore it is possible to cut wedge-shaped regions into the lamella to realize a constant increase of the sample thickness. The sample displayed in Fig. 2.3f exhibits six thin windows with wedge shape.

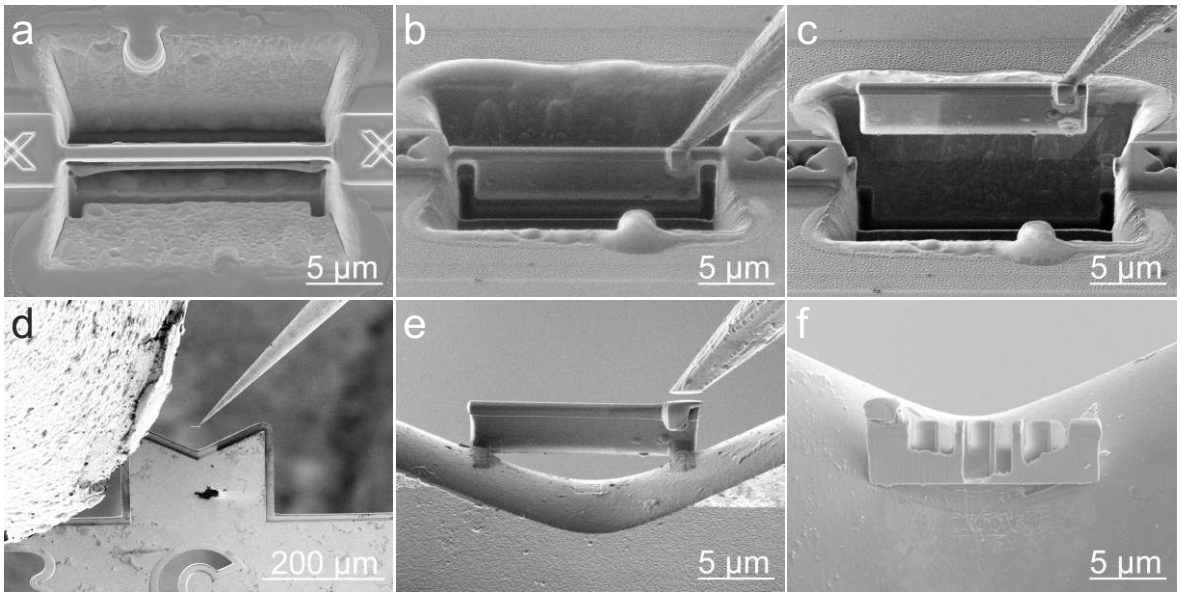

Figure 2.3: Different steps of the FIB cross-section sample preparation: a) milling of trenches; b) cutting free of the lamella and attachment of the manipulator needle; c) lift out of the lamella; d) transfer to the sample holder (the GIS nozzle is visible in the upper left corner); e) Attachment of the lamella to the sample holder and removal of the manipulator needle; f) thinned and polished wedge-shaped sample windows in the lamella.

Thickness determination

In the course of this work FIB is also used to determine the thickness of either free-standing thin films on copper grids or layer systems on substrates.
As a first step the samples are coated with a plasma-sputtered platinum protection layer. In the case of the free-standing films, the sample is covered with platinum from

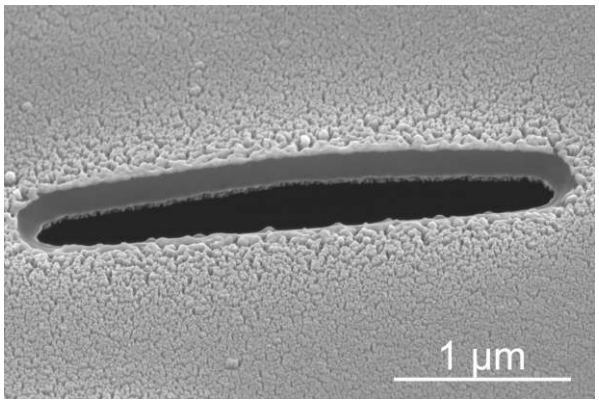

Figure 2.4: SE image of a FIB cut for thickness determination in a P3HS film covered on top and bottom with a thin platinum protection layer.

the bottom side. Then a rectangle is milled with FIB into the sample to obtain cross-section perspective and to measure the film thickness. In Fig. 2.4 an SE image of a FIB cut in a P3HS film is displayed. The platinum protection layers appear bright in the image, in contrast to the darker P3HS film. The thickness of the P3HS film can be easily measured by considering the tilt angle of 52°.

2.2 Scanning electron microscopy

Scanning electron microscopy (SEM) is a common technique to image and analyze the surface properties of bulk samples [84]. In a scanning electron microscope the sample surface is scanned pixel by pixel with a focused electron probe. The interaction of the incident electrons with the sample material gives rise to different signals which can be used for image formation [79, 85]. The most frequently used signals are SEs, backscattered electrons (BSEs) and X-rays.
SEs are mainly valence electrons from atoms close to the surface and are released due to inelastic scattering with the incident electrons. SEs are characterized by a small energy (<50 eV) and originate from a very thin surface layer only a few nm in thickness [79]. Furthermore, the SE yield (number of SEs per primary electron) is strongly determined by the local inclination of the sample surface with respect to the incident beam, which causes a high SE intensity at surface edges ('edge effect') [79]. Thus, SEs are well suited to image the topography of the sample [84].
BSEs have energies higher than 50 eV. They are generated by scattering of the primary electron in the Coulomb field of an atomic nucleus [79]. The BSE yield strongly depends on the mean atomic number of the sample material, so BSEs can be used for material-sensitive imaging [84]. Due to the higher energy of BSEs compared to SEs, the detected BSEs stem typically from deeper regions of the sample.
For the acquisition of SEs and BSEs different detectors are available. In this work a through-the-lens detector[4] was used. The detector is located inside the electron column of the microscope above the objective lens, which results in a high collection efficiency [84]. SEs and BSEs can be separated by applying a bias voltage [80].
X-rays are generated by inelastic interactions of the incident electrons with the orbital electrons of the sample atoms. If an electron from an inner orbital is excited to a higher state, the empty state is filled by another electron from a higher orbital, releasing the excess energy as either a photon or an Auger electron. Since the energies of emitted

[4]also called in-lens detector (depending on the manufacturer)

X-rays are characteristic for each element, the X-ray signal can be used to analyze the composition of a sample [79]. X-rays leaving the sample can originate from even deeper regions than BSEs due to their lower absorption, which results in a lower lateral resolution in the order of 1 µm.
In general the resolution of SEM is limited by the beam diameter of the electron probe and the interaction volume, i.e., the region of the sample from which the detected signal originates [85]. For modern field-emission gun (FEG) microscopes a resolution better than 1 nm can be achieved in SE images [86].

2.3 Scanning transmission electron microscopy at low and high electron energies

In general, a distinction is made between high-energy STEM (high-keV STEM) and low-energy STEM (low-keV STEM). High-keV STEM is an established technique which is usually carried out in a transmission electron microscope with a STEM unit [79]. Typical operating energies are 80-300 keV. Low-keV STEM is commonly performed in a scanning electron microscope equipped with a STEM detector, working with energies lower than 30 keV. Low-keV STEM is a relatively new technique, because for a long time it was not beneficial to use a scanning electron microscope in transmission mode, due to the low resolution (≈10 nm) compared to TEM. This changed with the use of FEGs for scanning electron microscopes and the development of improved electron optics [87].
In this work low-keV STEM was used for the first time to investigate the nanomorphology of organic solar cell absorber layers. Although low-keV STEM is a very promising technique only a few applications can be found in literature. It has to be noted that up to now no specific term for this technique was established. Abbreviations like TSEM[5], LVSTEM[6] or STEM-in-SEM are also used [87].

Working pinciple of STEM

In STEM the sample surface is scanned with a focused electron beam. The detector is positioned directly below the sample and collects the transmitted electrons as a function of the beam position. In contrast to TEM no image-forming lens system is required. This has the advantage that the aberrations caused by imaging lenses do not play a role in STEM [79]. The resolution of the microscope is only limited by the beam diameter and the interaction volume of the incident electrons in the sample [85, 87]. A scheme of the STEM setup is depicted in Fig. 2.5. A STEM detector is usually divided into three different segments. The bright field (BF) detector is positioned on the optical axis and collects only electrons that are unscattered or scattered into very small angles. The annular dark-field (DF) detector is positioned concentrically around the BF segment, which collects electrons with intermediate scattering angles. Electrons scattered into large angles are detected by the HAADF segment. Imaging with the HAADF detector is based on incoherent scattering. This is caused on the one hand by the geometry of the detector, which averages over a large detection angle range, and on the other hand by thermal diffuse scattering (electron scattering in crystals by phonons) [88, 89]. HAADF

[5]Transmission scanning electron microscopy
[6]Low-voltage STEM

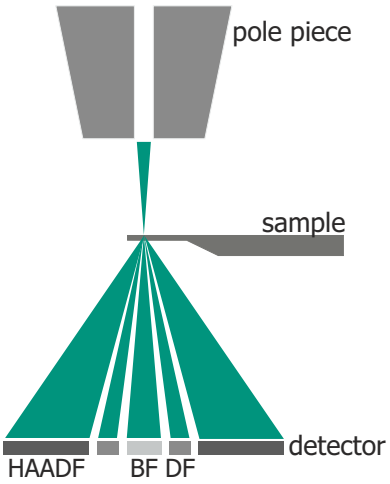

Figure 2.5: Scheme of the STEM setup: The focused electron beam is scanned along the sample surface. For every point on the sample surface the detector underneath the sample records the intensity of transmitted electrons. The detector is divided into different segments: the bright field (BF), the dark-field (DF) and the high-angle annular dark-field (HAADF).

STEM images are therefore intuitively interpretable, because there is no influence of coherent interferences of electron waves on the image formation. Scattering into large angles is mainly based on the interaction of the electrons with the nucleus of the target atoms [90]. Since the screening of the nucleus by the shell electrons decreases with increasing scattering angle (Eq. 3.1), the image intensity depends strongly on the atomic number of the sample material. For this reason HAADF STEM is often called Z-contrast imaging [87].

Low-keV STEM

The low-keV STEM experiments in this work were carried out with a FEI Dual Beam Strata 400S microscope. It is equipped with a STEM unit, which includes a flip stage and a retractable STEM detector. In the course of this work two different STEM detectors were applied, the STEM II and the STEM III detector (FEI Company), which are depicted in Fig. 2.6. In contrast to the STEM II detector, the BF and DF rings of the STEM III detector are subdivided into two and three rings, respectively. The HAADF ring is composed of six azimuthal segments instead of twelve. Furthermore the spacings between the different detector segments are smaller. The exact dimensions of the HAADF detector segments are listed in Table 2.1. The collection angles can be varied by changing the working distance (WD), i.e., the distance between sample and

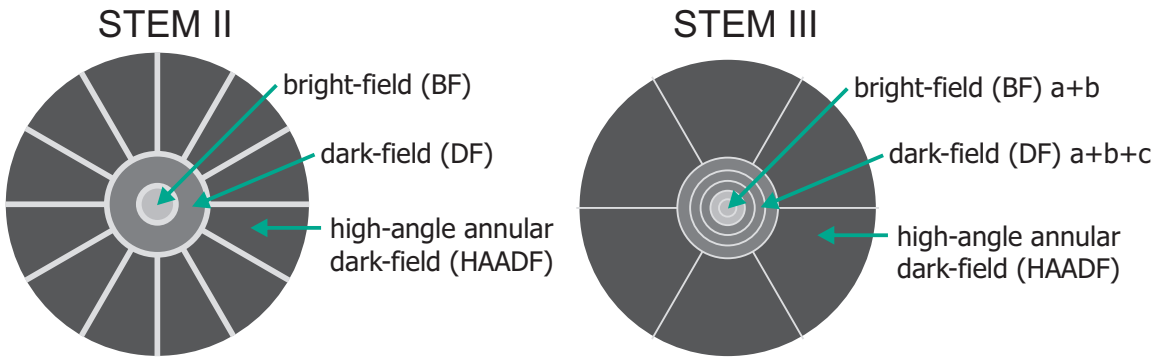

Figure 2.6: Design of the STEM II and the STEM III detector (scheme is not to scale).

	HAADF				
detector model	$r_{\min}$ [mm]	$r_{\max}$ [mm]	area [mm^2]	$\theta_{\min}$ [rad]	$\theta_{\max}$ [rad]
STEM II	2.60	11.10	365.84	0.20	0.71
STEM III	2.33	10.00	297.17	0.17	0.63

Table 2.1: Dimensions of the STEM II and III HAADF detector segments with the inner and outer radius $r_{\min}$ and $r_{\max}$. $\theta_{\min}$ and $\theta_{\max}$ are the minimum and maximum detection angles for a working distance (WD) of 5 mm.

pole piece of the objective lens. Since the distance between detector and pole piece is fixed, a change of the sample height results in both, a change of the WD and a change of the sample detector distance, which in turn changes the collection angles. In Table 2.1 the inner and outer detection angle is listed for a WD of 5 mm, which was used in this work.

For soft matter samples the contrast in TEM is mainly due to differences in the mass thickness. It is usually very low at typical TEM electron energies (80-300 keV), because the materials are mainly composed of light elements like carbon, hydrogen or oxygen. Moreover, the density of these materials is usually similar. Mass-thickness contrast is on the one hand based on different densities in the sample, and on the other hand on local variations of the sample thickness. Therefore it has always to be kept in mind that thickness variations could be a source of contrast in the images.
A possibility to enhance the contrast of soft matter samples is the reduction of the electron energy, which is an important motivation for the application of low-keV STEM. The contrast increases with decreasing electron energies due to higher scattering cross-sections [87, 91]. Delong et al. showed that a decrease of the acceleration voltage from 100 kV to a few kV increases the contrast of a 20 nm thin carbon film by almost one order of magnitude [92]. The use of small accelerating voltages does not only offer advantages. The resolution of the microscope is decreased at larger wavelengths [87]. Besides, the high image contrast results from a strong interaction between the electron beam and the sample, which can also cause ionization damage in samples with small electical conductivity. Furthermore, contamination is more pronounced at lower energies (see Chapter 2.7).
The first applications of low-keV STEM (as from 1968) were mainly experiments with biological samples which did not require a high resolution (reviewed in [87]). In 1974 Wall et al. investigated uranium and mercury samples at 30 and 40 keV in a dedicated STEM instrument with a tungsten field emission source and achieved a resolution of 3 Å [93]. After the upcoming of FEG-SEM and the improvement of the electron optics, low-keV STEM was also applied for the investigation of polymer samples. In the year 2000 Lednický et al. investigated blends of different polymers at 25 keV at a microscopic scale [94]. They showed that a density difference of only 0.04 g/cm^3 is sufficient to cause visible contrast between the different phases in the blends. Williams et al. studied blends of the semiconduction polymers F8BT[7] and PFB[8] by an environmental scanning electron microscopy (ESEM) instrument equipped with a simple two-segment

[7]poly(9,9'-dioctylfluorene-co-benzothiadiazole)
[8]poly(9,9'-dioctylfluorene-co-bis-N,N'-(4- butylphenyl)-bis-N,N'-phenyl-1,4-phenylenediamine)

BSE detector. The images exhibited a high contrast and a good signal-to-noise ratio and structures with a size of a few µm could be easily resolved [95]. Faucheu et al. also used a BSE detector in an ESEM instrument to investigate 100 nm small latex spheres with different surfactants [96]. Recently Guise et al. demonstrated the capabilities of low-keV STEM by comparing low-keV STEM images with high-energy TEM images of different polymer systems [97]. Although the resolution of low-keV STEM was not as good as in TEM at high electron energies, it was sufficient to resolve the structures in many polymer systems. They demonstrated that low-keV STEM is especially useful for samples with low contrast and for beam sensitive materials. Furthermore low-keV STEM allows a much faster and cheaper imaging, especially if sample holders with several sample positions are used. Another advantage of low-keV STEM is the quick change of the imaging parameters for contrast optimization. This concerns the electron energy, WD and consequently the detection angle range.
Up to now relatively few methodological studies on low-keV STEM have been published, although the technique is particularly promising for the quantification of image information. Merli et al. and Morandi et al. used low-keV STEM to analyze dopant profiles in semiconductors [98–100]. Volkenandt et al. applied low-keV STEM to determine the thickness of a GaAs TEM sample and the composition of InGaAs in an InGaAs/GaAs heterostructure by comparing experimental low-keV STEM data with the results of Monte Carlo (MC) simulations [101].

High-keV STEM

Although high-keV STEM is a very common technique in inorganic material science [102], it is only rarely applied for the investigation of polymers and carbon-based materials due to knock-on damage. Loos et al. [103] and Sourty et al. [104] showed the versatility of high-keV STEM for imaging different polymer systems composed of carbon and lighter elements with only small differences in atomic number and material density. For all polymer systems excellent contrast could be achieved between the components. Moreover, interfaces in high-keV STEM images appeared much clearer than in BF TEM images which have to be acquired under defocused conditions for sufficient contrast (see Chapter 2.4).
In direct comparison with low-keV STEM, high-keV STEM has a better resolution, due to the higher electron energy. Although the contrast is more pronounced at lower energies, the usage of high-keV STEM can be advisable if particularly small sample structures are of interest. Furthermore contamination and ionization damage are reduced at higher electron energies (see Chapter 2.7).

2.4 Transmission electron microscopy

In contrast to SEM and STEM, in TEM the entire sample region of interest is illuminated with a defocused electron beam, which is formed by a condenser-lens system. Another difference to STEM is that an image-forming lens system below the sample is needed [79]. It consists of at least three lenses: an objective lens, an intermediate lens and a projector lens. The objective lens forms the first diffraction pattern in the back focal plane and the first intermediate image in front of the intermediate lens. Depending on the excitation of this lens it either magnifies the the diffraction pattern (diffraction mode) or the intermediate image (imaging mode). Either the diffraction

pattern or the image is further magnified by the projector lens [105]. Finally the transmitted electrons are detected with an electron-sensitive charge-coupled-device (CCD) camera [106].
In the imaging mode an objective aperture can be inserted in the back focal plane (diffraction plane) to select the electrons contributing to the image. In the BF mode all electrons except for the unscattered electrons are blocked. In DF mode only electrons with a certain scattering vector are chosen.
In diffraction mode apertures can be inserted in the first intermediate image plane to select the sample area from which the diffraction pattern is acquired. Consequently this technique is called selected area electron diffraction (SAED) [105, 106]. It allows structure determination from small sample regions.
In TEM a fundamental distinction is made between two kinds of contrast mechanism: amplitude and phase contrast. Amplitude contrast is a comprehensive term for contrast mechanisms which are based on the variation of the amplitude of the electron wave. One of these mechanisms is mass-thickness contrast, which is based on incoherent elastic Rutherford scattering. If a sample area is thicker or has a higher mass (higher density or atomic number), more electrons are scattered and do not contribute to the BF image, i.e., the sample region appears darker than the surroundings. The other representative of amplitude contrast is diffraction contrast. It is based on coherent elastic Bragg diffraction where the scattering occurs at distinct angles, depending on the crystalline structure of the sample [106].
Phase contrast is based on the phase differences of the electron waves transmitted through a specimen. This is exploited for example in high-resolution transmission electron microscopy (HRTEM), were a large objective aperture is used to select several Bragg beams. The interference pattern of these beams reflects the periodicity of the crystal lattice of the sample. Nevertheless, it must be noted that the interference pattern is not a direct image of the sample structure and cannot be intuitively interpreted. This is due to the contrast-transfer function, which contains the imaging properties of the transmission electron microscope. It describes the phase shift on the object wave-function which depends on the lens aberration, defocus and spatial frequency [106]. Due to the form of the contrast transfer function mixing of phase and amplitude contrast occurs.
A more detailed description of TEM can be found for example in the textbooks of Williams and Carter [106], Reimer [105] and Michler [79].

TEM studies on polymer samples

A major part of the nanomorphology studies of organic solar cell absorber layers are carried out with TEM. However, TEM imaging is hampered by limitations such as knock-on damage, which will be discussed in detail in Chapter 2.7. Even more limiting is the poor contrast of samples containing materials that consist of light elements with only slightly different densities as summarized by Drummy and Kübel [107]. There are several approaches to increase the contrast of soft-matter samples including staining with heavy elements [85], phase-plate imaging [79] or low-energy TEM [108]. The most common method is to work under defocused conditions [79, 85, 109]. At Scherzer focus, which is usually considered as the condition for optimum phase transfer and therefore for high resolution, low spatial frequencies hardly contribute to the image. This is due to the sinusoidal shape of the phase contrast transfer function. By increasing the

defocus the passband of spatial frequencies contributing to the image can be shifted to lower spatial frequencies. The required defocus values depend on the typical feature sizes in the sample [79]. For typical BHJ solar cell samples, the needed defocus is rather large and in the range of a few µm. However, enhancement of comparably large objects by defocussing is accompanied by a loss of resolution and a strong delocalization of the image information. This impedes not only the interpretation of the TEM images but also accurate size measurements.
Despite of the limitations of TEM for the analysis of soft matter samples, numerous TEM studies were published regarding the nanomorphology of organic solar cell absorber layers. Probably the most investigated system is P3HT:PC_{61}BM. Applying BF TEM different groups showed the formation of P3HT nanorods upon annealing [110–113]. Furthermore large PC_{61}BM crystals could be observed with BF TEM [114]. Nevertheless, it has to be noted that TEM investigations fail for P3HT:PC_{61}BM layers without pronounced phase separation. This is related to the three-dimensional domain distribution that leads to the superposition of the weak contrast features along the electron-beam path through the sample. The averaging effect prevents a clear distinction of small-scale features in the two-dimensional projection of a TEM image.
While BF TEM is the most common mode to investigate the morphology of BHJ solar cells, DF TEM is only rarely employed [85]. This is due to the fact that polymer crystals are usually very sensitive to electron irradiation and relatively long exposure times are necessary to record DF TEM images. Only few examples for DF imaging of polymer samples can be found in literature [115–118]. DF TEM can be used to analyze the size and the orientation of crystalline domains [85], information that is not accessible via BF TEM.
To analyze the crystalline structure of BHJ absorber layers, SAED was be applied. In nanocrystalline or amorphous materials Debye-Scherrer rings are observed in the diffraction pattern [105]. For textured materials with a preferential orientation of crystallites arcs instead of full rings appear [106]. The width of the diffraction rings gives information about the degree of crystallinity, the strain and the size of the grains [106]. For the investigation of the BHJ morphology in organic solar cell absorber layers SAED is particularly useful because the typical π-π stacking distances of polymers can be measured from the diffraction patterns [36, 119–121].
To image the lattice of the polymer nanocrystals in real space, HRTEM images have to be acquired. This technique is also strongly limited by the beam sensitivity of the sample, but nevertheless, several examples of HRTEM on polymers or organic molecules can be found in literature, outlined for example in the review of Martin et al. [122]. There are also some HRTEM investigations on organic solar cell materials. Kalita et al. and Reyes-Reyes et al published for example HRTEM images of small PC_{61}BM nanocrystals in P3HT:PC_{61}BM blends [123, 124], while Drummy et al. imaged the (100)-lattice planes of P3HT with low-dose HRTEM [125].

2.5 Electron energy loss spectroscopy and energy filtered transmission electron micrsocopy

To overcome the problem of low contrast for soft matter samples in conventional TEM, energy-filtered transmission electron microscopy (EFTEM) can be applied [126]. EFTEM is related to electron energy loss spectroscopy (EELS), were the energy dis-

tribution of the transmitted electrons is detected. In EFTEM a certain part of the electron energy loss (EEL) spectra is selected with an energy slit and only electrons with a specific energy loss are used for imaging. If materials exhibit different energy losses, they can be differentiated by this material sensitive imaging technique.
There are two approaches to distinguish between the different phases in polymer samples: core-loss or plasmon-loss imaging. If one of the phases contains a heteroatom, which cannot be found in the other phase, the core-loss ionization edge of this heteroatom can be used for EFTEM imaging. For this purpose an energy slit is positioned on the ionization edge to let only electrons with this specific energy contribute to the image. Applying this technique Kozub et al., for example, showed the formation of P3HT nanorods upon annealing in P3HT:$PC_{61}BM$ blends [127]. They exploited the fact that P3HT contains a sulfur heteroatom, while $PC_{61}BM$ is only composed of carbon, hydrogen and oxygen.
If no characteristic heteroatoms are present in one of the phases, the plasmon loss imaging technique has to be applied. Here, the distinction is based on the fact that the plasmon-loss energies of the two examined absorber materials are slightly different and can be selected by the energy slit. Plasmons are collective oscillations of the conductive- or valence-band electrons with an energy that is strongly related to the electronic structure of the materials. Besides, the intensity of the plasmon peak is about 100 times higher than the intensity of the core loss edges, so the signal-to-noise ratio of the images is significantly better. Hence, plasmon-loss imaging is often applied in addition to core-loss imaging. For example several groups applied plasmon-loss imaging for the analysis of P3HT:$PC_{61}BM$ blends [125, 128–130], although P3HT contains a sulfur-heteroatom. An other EFTEM investigation was published by Schindler et al., who analyzed the different phases in zinc phthalocyanine (ZnPc):C_{60} blends by plasmon loss imaging [131].

2.6 Electron tomography

Standard TEM-based techniques only provide a two-dimensional (2D) projection of the examined volume. This limitation can be overcome by TEM tomography which facilitates the reconstruction of the three-dimensional (3D) sample structure from a series of 2D projections. Three-dimensional reconstruction requires the acquisition of an image series where the sample is tilted with respect to the electron beam, usually in the range of at least $\pm 70°$ [132]. After the alignment of the images a 3D model of the sample can be reconstructed with a resolution of about 1 nm not only in-plane, but also in z-direction [133].
To reconstruct a 3D volume from 2D projections the images have to fulfill the 'projection requirement'. It states that the intensity of a 2D projection must be at least a strictly monotonic function of the material properties projected by the electron beam [132, 134]. This is valid for BF images of amorphous materials, because a higher mass-thickness results in a darker image. The advantage of using the BF TEM mode for a tomogram are short exposure times and therefore lower beam damage and contamination. For polymer samples this is a very important aspect, which will be further discussed in Section 2.7. The disadvantage of this imaging mode is the low contrast and therefore the required defocus, which can cause reconstruction artifacts [128, 135]. To overcome this, HAADF STEM can be applied which provides a strong Z-contrast.

However, this scanning technique requires much longer acquisition times per image and is therefore not suitable for beam-sensitive samples and materials that are prone for contamination. It turned out that for the FHBC:$PC_{61}BM$ samples investigated in this work (see Chapter 7), the BF TEM mode was better suited, because in STEM mode the contamination significantly degrades the image contrast already after a few image acquisitions. To enhance the contrast it is also possible to use EFTEM images for tomography. As already mentioned in Section 2.5 the image contrast in the EFTEM mode results from differences in composition or electronic structure of the different phases. Although the exposure time is increased compared to conventional BF TEM it is still shorter than the exposure times needed in STEM mode EFTEM allows images to be taken in Gaussian focus [128].
To reconstruct the 3D volume several methods can be applied. Most common are the weighted back-projection (WBP), the algebraic reconstruction technique (ART) and the simultaneous iterative reconstruction technique (SIRT) [136], which are reviewed for example by van Bavel et al. [132]. The reconstruction methods are all based on the 'central slice theorem'. It states that the Fourier transform of an object's projection under a certain angle is a 2D cut under the same angle through the 3D Fourier transform of the object [137].
In this work the SIRT algorithm was chosen to reconstruct 3D volumes. It is an iterative method for which in each iteration step the reconstructed volume is re-projected in different angles and compared with the original projections. The differences of the images are then used to further adjust the reconstructed volume. The iterations are repeated until the image information is no longer increasing, which is typically the case after at least 15 iterations [132]. These steps require high computing power, nevertheless SIRT is commonly applied due to the high signal-to-noise ratio of the reconstructed images and only limited edge artifacts [132, 138].
Several examples for tomograms of organic photovoltaic materials can be found in literature. Van Bavel et al. investigated the formation and vertical distribution of P3HT nanorods in P3HT:$PC_{61}BM$ blends depending on the film thickness and blend composition [139–142]. In addition they imaged the 3D structures of BHJs based on different donor materials like the copolymer PF10TBT[9] or MDMO-PPV[10] [142]. Azimi et al. reconstructed the vertical distribution of Si-PCPDTBT[11] crystals in blends with $PC_{61}BM$ and bis-$PC_{61}BM$ [143], while Hou et al. analyzed the nanomorphology of blends containing the polymer TQ1[12] and $PC_{71}BM$ [144]. Herzing et al. and Pfannmöller et al. applied plasmon-loss EFTEM and electron spectroscopic imaging (ESI) tomography to reveal the 3D structure of P3HT:$PC_{61}BM$ blends [128, 129]. Roehling et al. increased the contrast of the tomogram by using HAADF STEM and endohedral fullerenes (which contain a heavy Lu_3N cluster within the fullerene cage) instead of conventional $PC_{61}BM$ in blends with P3HT [145]. Like Pfannmöller et al. they evidenced a mixed fullerene-polymer phase besides of two pure phases.

[9] poly[9,9-didecanefluorene-alt-(bis-thienylene)benzothiadiazole]
[10] poly[2- methoxy-5-(3',7'-dimethyloctyloxy)-1,4-phenylene vinylene]
[11] (poly[(4,40-bis(2-ethylhexyl)dithieno[3,2-b:20,30-d]silole)-2,6-diyl-alt-(4,7-bis(2-thienyl)-2,1,3-benzothiadiazole)-5,50-diyl])
[12] poly[2,3-bis-(3-octyloxyphenyl)quinoxaline-5,8-diyl- alt - thiophene-2,5-diyl]

2.7 Beam damage and contamination in electron microscopy

Beam Damage

The dominating effects of the interaction of electrons with organic matter are ionization and knock-on damage. Ionization damage is caused by inelastic scattering processes, which can lead to ionization and therefore to the break of chemical bonds and a displacement of atoms in the sample. Knock-on damage is caused by collision processes, also resulting in a displacement of atoms. Additional effects like chain scission or cross-linking, mass loss, heat generation and charging-up can also occur [79, 146]. In general knock-on damage increases for higher electron energies, while ionization damage is more intense at low electron energies [146]. Furthermore the impact of ionization also depends on the electrical conductivity of the sample. While in conducting materials the ionization can be quenched by the conduction electrons, the excitation can cause irreversible bond breaking in insulators or semiconductors [146]. According to Banhard knock-on damage is the most substantial radiation effect in carbon nanostructures, although he also mentioned the sensitivity of, e.g., fullerenes towards ionization damage at low electron energies in the range of 1 keV [146].
The stability of organic materials under electron irradiation is typically described by the critical electron dose. It is the number of electrons per illuminated sample area which leads to a significant change of measurable sample properties, shown for example by fading of diffraction rings of crystalline samples [122]. Drummy et al. summarized the critical electron dose measurements of different groups in a review and concluded that beam damage of crystalline polymers and small molecules is most significant at electron energies around 5 kV [108]. The reason for this is the strong interaction of the incoming electrons with the sample atoms at these low energies, which is also responsible for the higher contrast in low-keV STEM. Besides, in a good approximation polymers with a high thermal stability also exhibit a high electron beam stability [122] and it was shown that the beam sensitivity of a polymer decreases with increasing carbon content [79].
All electron-beam-induced damages happen within very short times scales. This means that it is usually not possible to investigate samples without damages. Nevertheless beam damage is often a smaller problem than one could initially assume. Even if the sample is strongly altered on molecular scale, the supramolecular structure e.g. the morphology of the sample often remains unchanged. This is particularly the case for amorphous polymers, where the image contrast is only based on differences in the mass-thickness [79].
The situation, however, is different if the crystallinity or the electronic structure of the polymer samples are of interest. In crystalline polymers the electron exposure can lead to an amorphization of the irradiated areas [132]. This hinders not only the direct imaging of lattice planes by HRTEM, but also the acquisition of electron diffraction patterns or DF TEM images. If the electronic structure of a sample is changed due to the electron irradiation, a change in the low-loss region of EEL spectra can be observed [147].
There are several approaches to avoid beam damage. The first is to chose an appropriate electron energy for investigated sample. If knock-on damage prevails, the electron energy has to be reduced [146]. If ionization is the predominant damaging effect, an

increased electron energy can be beneficial [79]. There are also some cases reported where the use of STEM resulted in a reduced beam damage compared to TEM [79]. Furthermore, low-dose techniques can be used. This involves for example focusing at a sample area adjacent to the final position of interest and the use of shutters before and after the image acquisition [85]. Another possibility to reduce irradiation damage is to cool the sample in a liquid-nitrogen-cooled sample holder. At lower temperatures amorphization, chain scission and cross-linking is reduced [79, 85].

Contamination

Even at high vacuum there are always hydrocarbon molecules left in the microscope chamber and on the sample surface [84, 148]. They stem either from the oil of the vacuum diffusion pumps, the grease of the vacuum seals or they have already been on the sample before it was loaded into the microscope. The bonds of hydrocarbon molecules can be cracked by electrons which leads to polymerization by cross-linking. Due to the high surface mobility of the hydrocarbons, further molecules can diffuse to the illuminated area and attach to the carbon atoms [84]. Moreover, hydrocarbons from the environment can be adsorbed and cracked. Thus a carbon-rich film is formed in the illuminated or scanned area [148]. In Fig. 2.7 a SE SEM image of a previously illuminated and contaminated area is presented. The contamination appears darker in SE images and, depending on the thickness of the contamination layer, the resolution of the image can be significantly decreased. At low current density the thickness of the contamination layer is proportional to the dissipated energy. The following proportionality between contamination thickness t_c and electron energy E was found [149]:

$$t_c \propto E^{-0.8}. \tag{2.1}$$

Accordingly, contamination is stronger for lower electron energies and is more pronounced in low-keV STEM than in conventional STEM.
There are several approaches to decrease contamination depending on the kind of microscope and sample material. By using a cold-trap the number of hydrocarbons in the vicinity of the sample can be reduced. This is possible in TEM and SEM and is independent of the sample material. Another possibility is to cool the sample itself, which decreases significantly the mobility of the hydrocarbons. It was also shown to be advantageous to preirradiate a larger sample area to crack and immobilize the adsorbed hydrocarbons before a smaller sample area is imaged [84]. Depending on the sample material it can be advisable to clean the sample before the examination in the microscope. This can either be done by solvents or by plasma etching. Since the samples investigated in the course of this work do not resist this kind of treatments,

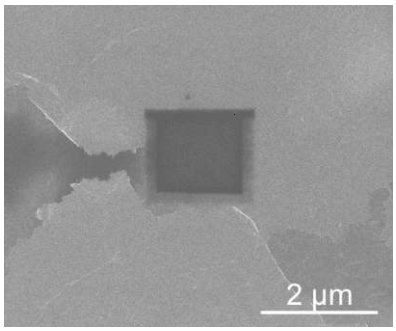

Figure 2.7: SE image of a previously scanned and therefore contaminated area on an amorphous carbon film.

contamination effects were often not avoidable. A useful application of contamination will be presented in Chapter 3. The increased thickness of a contaminated area is used to analyze contrast inversion in HAADF mode which depends on the sample thickness.

3 Low-energy electron scattering in low-density materials

Results are presented in this chapter concerning quantitative electron scattering in amorphous carbon and carbon-based materials, which are obtained by HAADF STEM at low energies ($\leq$30 keV). Experimental HAADF STEM intensities from samples with well-known composition and thickness are compared with results of Monte Carlo (MC) simulations and empirical equations describing multiple electron scattering. A well-defined relationship is found between the maximum HAADF STEM intensity and sample thickness. This relationship is exploited to derive a quantitative description for the mean quadratic scattering angle and for the calculation of the transmitted HAADF STEM intensity as a function of the relevant materials parameters and electron energy. The formalism can be also applied to determine sample thicknesses by varying the primary energy of the incident electrons.

3.1 Theoretical background

3.1.1 Electron scattering cross-sections

The scattering cross-section is a measure for the probability that a scattering process occurs. It is given in cm^2 and represents the area around the target in which a scattering process occurs. A distinction is made between elastic and inelastic scattering. Elastic scattering is an interaction in which the kinetic energy and the momentum of the impact partners are conserved. For inelastic scattering this is not the case.

Elastic scattering

The first equation for the description of the differential elastic cross-section was developed 1911 by Rutherford [150]. In this classically derived equation the screening of the Coulomb potential by the shell electrons is neglected, which results in a divergence of the equation for small scattering angles θ. The screening of the nucleus can be calculated on the basis of the quantum mechanical Schrödinger equation and leads to the following modification of the Rutherford cross-section for electrons scattered at atoms

$$\frac{d\sigma_{el}}{d\Omega} = \frac{e^4 Z^2}{4(4\pi\epsilon_0)^2 m^2 v^4} \frac{1}{[\sin^2(\theta/2) + \sin^2(\theta_0/2)]^2} \tag{3.1}$$

where e stands for the elementary charge, Z for the atomic number of the target material, m for the mass and v for the velocity of the incident particle. Furthermore the characteristic angle $\theta_0 = \lambda/2\pi R$ is introduced. It is related to the screening length R of the atom and the de Broglie wavelength λ of the electron. R can be calculated by $R = a_H Z^{(-1/3)}$, were a_H is the Bohr radius [84].

Although this equation is sufficiently adequate for many applications there are still deviations between calculated and measured values especially at large scattering angles. To overcome this problem, quantum mechanical Mott cross-sections have to be used [151]. They account not only for relativistic effects but also the spin of the scattered electron. In particular for heavy target atoms and low electron energies, Mott cross-sections should be more accurate than the classical screened Rutherford model. According to Reimer [84] the difference between the two cross-sections is minimal for light target atoms and electron energies between 3-30 keV (typical SEM energies). Browning et al. [152] state that screened Rutherford cross-sections give acceptable results for high energies and low atomic numbers, while Mott cross-sections are required for low to medium incident energies (0.1-30 keV) and high atomic number. Shimizu and Ze-Jun [153] are more specific and suggest the use of screened Rutherford cross-sections in the energy range of 1-20 keV for elements with $Z \leq 13$.

In contrast to the Rutherford cross-sections, analytical expressions are not available for the Mott cross-sections. Tabulated Mott cross-sections are obtained by solving the Dirac equation. For this purpose, a precise knowledge of the scattering amplitudes is necessary, which can be determined numerically by an expansion into Legendre polynomials [84]. The cross-sections used in this work were calculated by Czyżeweski et al. [154].

Inelastic scattering

In inelastic scattering processes the kinetic energy of the incoming electron is partially transferred to the target atom during the scattering, which is then excited. One distinguishes between the following excitation mechanisms [84][106]:

- Phonon excitation in solids and excitation of oscillations in molecules. The energy loss E_{loss} is in the range of 20 meV and 1 eV. It is the most frequent inelastic excitation and leads to the heating of the target.
- Plasmon excitations, i.e., collective longitudinal oscillations of the free-electron gas in metals or single valence electron excitations in insulators. ($0 < E_{\text{loss}} < 50$ eV).
- Inter- and intra-band transitions of electrons in the outer shells. ($0 < E_{\text{loss}} < 50$ eV).
- Ionization of inner-shell electrons or excitation of electrons into higher binding states. ($E_{\text{loss}} > 50$ eV).

Similar to elastic scattering a differential inelastic cross-section can be defined. For this purpose the Møller formula is usually employed, which describes the energy loss due to electron-electron collisions [155].

3.1.2 Semi-empirical equations for multiple scattering

Under typical experimental conditions it is very difficult to realize single-electron scattering. Even in thin samples most of the electrons experience several scattering processes. Thus special mathematical models are needed to calculate the energy loss and the angular distribution of the transmitted electrons. The limitations of these models define the maximum sample thickness, which can be described by multiple scattering approaches [84]. An important parameter to describe plural and multiple scattering is the mean free path length Λ. It determines the decrease of the incoming electron current I_0 along the transmission through the sample. The electron intensity which is transmitted through a sample with the thickness t can be written as exponential function:

$$I = I_0 \, \mathrm{e}^{\left(-\frac{t}{\Lambda}\right)} = I_0 \, \mathrm{e}^{(-N\sigma_t t)} = I_0 \, \mathrm{e}^{-p}. \tag{3.2}$$

The mean free path length is related to the total cross-section σ_t and the number of atoms per unit volume N. p is the number of collisions. On the basis of this value it can be evaluated if models for single ($p = 1$), plural ($p < 25$) oder multiple ($p > 25 \pm 5$) scattering need to be employed. For more than approximately 30 collisions the angular distribution of the transmitted electrons is not Gaussian anymore [84].
According to Reimer the mean free path length of electrons with 5 keV in carbon is 2.3 nm [84]. The thickness of the absorber layers of organic solar cells is typically in the range of 50-150 nm and the average number of collisions between 22 and 65. Thus for the description of the scattering, theories of plural and multiple scattering have to be used.

Angular distribution of transmitted electrons

For single scattering the angular distribution of the transmitted electrons depends on the normalized differential cross-section, which is called the single scattering func-

tion S_1:

$$S_1 = \frac{1}{\sigma}\frac{d\sigma}{d\Omega}. \tag{3.3}$$

A scattering function for m-fold scattering S_m is obtained by the m-fold self convolution of the single-scattering function S_1. The probability for m-fold scattering can be described by Poisson coefficients and the angular distribution can be written as

$$I(\theta)\mathrm{d}\Omega = I_0\mathrm{d}\Omega \sum_{m=0}^{\infty} \frac{p^m}{m!}\, e^{-p} S_m(\theta). \tag{3.4}$$

p denotes the number of collisions as defined in Eq. 3.2. (For a detailed derivation of this equation see [84].) To calculate the angular distribution analytically it is necessary to find an easier expression for the equation above. Goudsmit & Saunderson expanded therefore the scattering function into a series of Legendre polynomials [156]. These calculations are correct as long as the following two approximations apply, which are usually valid for plural scattering ($p < 25$). First, there is a negligible energy loss of the electrons, which means that the cross-section does not change through the sample. Second, the single-scattering angles are small.

When Goudsmit & Saunderson developed this equation in 1940 it was impossible to calculate numerically a solution, due to the lack of computing power. Even nowadays it is complex and very time-consuming [157]. Nevertheless, to be able to describe multiple scattering, several approximations and simplifications of Eq. 3.4 were introduced, which are listed and described in detail in [84].

Another approach to calculate the angular distribution of the transmitted electrons was the development of semi-empirical equations, based on the assumption that the angular distribution is Gaussian. This is the case if the scattering processes are independent of each other and if scattering into large angles and energy loss can be neglected [84]. The normalized electron intensity scattered into $d\Omega$ is described accordingly by the following equation

$$\frac{I(\theta)}{I_0} = \frac{\mathrm{d}\Omega}{2\pi\overline{\theta^2}}\, \mathrm{e}^{-\theta^2/2\overline{\theta^2}} \quad [158]. \tag{3.5}$$

$I(\theta)$ is the intensity scattered into the angle θ, I_0 is the intensity of the incident electrons and $\overline{\theta^2}$ the mean quadratic scattering angle.

Based on the screened Rutherford cross-section Bothe [159] developed by means of error theory the following semi-empirical term for $\overline{\theta^2}$

$$\overline{\theta^2_{\mathrm{B}}} = 10^9 \left(\frac{3.6Z}{E}\right)^2 \frac{\rho t}{A} \qquad [\mathrm{rad}^2]. \tag{3.6}$$

The electron energy E is given in eV and the mass thickness ρt in kg·m^{-2}. Z is the atomic number and A the atomic mass number. The factor 3.6 in the numerator was determined by comparing the theoretical equations with measurements of Crowther, which were performed at electron energies between 150 and 240 keV [160]. According to Cosslett & Thomas Eq. 3.6 is not valid for elements with $Z < 13$ and low electron energies [158].

To describe the angular distribution of the transmitted electrons at low energies,

Cosslett & Thomas proposed a modified equation

$$\overline{\theta_{\mathrm{C}}^2} = 1.2 \cdot 10^6 \, \frac{Z^{1.5}}{E} \frac{\rho t}{A} \qquad [\mathrm{rad}^2] \tag{3.7}$$

considering large angle scattering as well. Eq. 3.7 is in good agreement with experimental data for elements with $Z \geq 13$ as shown by Cosslett & Thomas.
However, the validity of Eqs. 3.6 and 3.7 has not been tested up to now for low atomic number materials and low electron energies.

3.1.3 Monte-Carlo simulations

Alternatively to the equations described in the previous section, low-energy electron scattering can be modeled by MC simulations, which is well established for samples with higher atomic numbers [161][101]. Statistically relevant results are obtained by applying suitable cross-sections to a large number of electrons subjected to several and multiple scattering processes and calculating their trajectories through the sample. Different simulation packages are available which differ in the used cross-sections and descriptions for the energy loss of the electrons. The simulations in this work were performed with the NISTMonte package [162]. Screened Rutherford cross-sections [150] and calculated Mott cross-sections of Czyżewski et al. [154] are applied (Chapter 3.1.1). To describe the energy loss of the electrons, usually the continuous slowing down approximation in the form of the energy loss equation of Bethe is implemented [163]. It is based on the Møller formula which combines the different inelastic scattering mechanisms, mentioned in section 3.1.1 [155]. An important variable in this equation is the mean ionization potential J, which depends on the atomic number Z of the sample atoms. For electron energies below the mean ionization energy of the sample Joy & Luo introduced an energy-dependent correction for J [164]. For the ionization potential several semi-empirical expressions exist, which differ significantly [162].
The MC simulations yield the angular and energy distribution of the electrons leaving the sample. To calculate the transmitted STEM intensity the total number of transmitted electrons is summed up in an angular range covered by the real STEM detector. The resulting number of electrons normalized with respect to the incident electrons can be set in relation to the measured intensity, if the characteristics of the semiconductor STEM detector are taken into account. The response of a semiconductor detector in terms of the collection current I_{cc} in dependence of the electron intensity I is given by

$$I_{\mathrm{cc}} = I \cdot G \cdot \epsilon_{\mathrm{c}}, \tag{3.8}$$

where G represents the gain of the detector and ϵ_c the charge collection efficiency [84]. If the range of the detected electrons lies completely in the depletion layer of the semiconductor detector, ϵ_c is near unity [84]. The gain G can be described by the following equation

$$G = \frac{\bar{E} - E_{\mathrm{th}}}{\bar{E}_{\mathrm{i}}} \cdot (1 - \eta_{\mathrm{c}}), \tag{3.9}$$

where E_{th} represents the threshold energy for electron detection which was determined to be 3 keV in this work. $\bar{E}$ is the mean energy of the incoming electrons, $\bar{E}_i$ the mean energy for electron-hole pair excitation (3.6 eV in silicon) and η_{c} the electron backscatter coefficient. The last term in Eq. 3.9 takes into account that electrons backscattered

from the detector do not contribute to the STEM intensity. The fraction of these electrons depends on their impact angle α and the atomic number Z of the detector material. It can be calculated by the following equation of Arnal et al. (described in [84])

$$\eta_c = (1 + \cos\alpha)^{-\frac{9}{\sqrt{Z}}}. \tag{3.10}$$

Thus the modification of the transmitted electron intensity by a semiconductor detector can be calculated and has to be taken into account if simulations are compared with experimental data.

3.2 Samples and experimental techniques

Samples

To analyze high-angle scattering at low electron energies three different materials with low atomic numbers and densities were studied: amorphous (a-)carbon, P3HT and the epoxy resin EPON^{TM}(Momentive Specialty Chemicals Inc.).
Amorphous carbon films were prepared by electron-beam evaporation on mica substrates with thicknesses of 50, 70, 100, 130, 160 and 190 nm, determined by FIB cross-sectioning. According to literature the density of amorphous carbon can vary considerably [165]. In this work a value of 1.9±0.3 g/cm^3 is assumed. The error limits take these variations of the density into account.
The polymer P3HT acquired from Rieke Metals was used as a second test material. The samples were fabricated by M. Klein at the Light Technology Institute (LTI), Karlsruhe Institute of Technology (KIT). As mentioned in Chapter 1.2 P3HT is employed in organic solar cells as absorber material. The thicknesses of the films were varied by choosing different concentrations of the solvent and spin coating velocities in the production process. The thickness of the films (twelve samples with thicknesses from 35 to 355 nm) was measured with a Dektak XT profilometer from Bruker and in addition on the basis of FIB-prepared cross-sections (Chapter 2.1.3).
To examine the polymer and carbon films by STEM, they were floated off the substrate with deionized water and transferred onto conventional copper TEM grids according to the procedure described in Chapter 2.1.1. In addition to the thin-film samples, wedge-shaped samples were prepared by FIB-milling. For this purpose, a platinum protection layer was deposited on the bulk samples to protect them from irradiation damage.
A wedge-shaped EPON sample with a wedge angle of 10° was studied as third test specimen. It was prepared by ultramicrotomy in the group of R. Reichelt (Institut für medizinische Physik und Biophysik, Westfälische Wilhelms-Universität, Münster, Germany).
The chemical compositions and the densities of the three different sample materials are listed in the following table:

material	composition	density[g/cm^3]
a-carbon	C	1.90±0.30
P3HT	$C_{10}H_{14}S$	1.08±0.10
EPON	$C_{113}H_{111}O_{24}$	1.25±0.10

Table 3.1: Composition and density of a-carbon, P3HT and EPON. The density of P3HT was measured by He-pycnometry.

Electron Microscopy

STEM and SEM imaging was carried out in the FEI Strata 400S dual-beam scanning electron microscope, as described in Chapter 2.3. For the analysis of the electron scattering at low electron energies the semiconductor STEM II detector was used. Images were taken at WD=5 mm which corresponds to a collection angle range from 0.2 to 0.7 rad. STEM imaging was carried out with electron primary energies between 3 and 20 keV in steps of 0.25 keV. An electron energy of 3 keV represents the lower limit for achieving visible contrast with the used detector. It has to be noted that HAADF

STEM imaging with a semiconductor STEM detector demands careful setting of gain and brightness to avoid oversaturation of the detector.

3.3 Experimental results

To quantitatively analyze low-energy electron scattering, the STEM intensity has to be measured on the basis of samples with known thickness and composition. Apart from thin-film samples with constant thickness, samples with a wedge-type thickness profile prepared by FIB milling were investigated. These samples show a well-defined thickness profile and allow the measurement of the STEM intensity within a wide range of sample thicknesses. Fig. 3.1 shows a top-view SEM image of an a-carbon wedge. The wedge angle is not constant and decreases from 22° at the thin edge to 18° at a larger distance from the edge. An error of ±3° was assumed for the wedge angle because the top view only shows the thin platinum coating on top of the carbon film, which is deposited for protection of the carbon layer during FIB milling (Chapter 2.1.3). It has to be also noted that the sample is not infinitesimal thin at the wedge edge.

Figs. 3.2a-c show three HAADF STEM cross-section images of the a-carbon wedge, which were taken at primary electron energies of 7, 10 and 13 keV. The supporting mica substrate and the platinum protection layer are indicated in Fig. 3.2a. Caused by the FIB-milling process delamination occurs leading to a gap between the substrate and the carbon layer. Intensity line profiles were taken along the carbon layer, which are displayed in Figs. 3.2d. The HAADF STEM intensity increases from the thin edge of the sample to a maximum, which depends on the electron energy. For thicker regions the intensity is reduced again. For higher energies the maximum is shifted towards thicker regions of the wedge. The dependence of the maximum intensity and corresponding sample thickness was systematically measured as a function of the electron energy between 3 and 15 keV. The maximum intensity and corresponding sample thickness can be considered as point of contrast inversion, which will be denoted as inversion point in the following.

The same behavior of the HAADF STEM intensity can be observed in MC simulations (based on Rutherford cross-sections), which is demonstrated in Fig. 3.3 for the relevant scattering angle range and primary electron energies. The intensity (normalized here by the number of incident electrons) shows maxima at a thickness, which is dependent on the primary electron energy. The position of the inversion point shifts with decreasing primary energy towards smaller sample thicknesses. The general behavior of the HAADF STEM intensity as a function of the thickness can be understood in the following way. The large-angle scattering probability is low for thin samples leading to low HAADF STEM intensities. More electrons contribute to the HAADF signal with increasing sample thickness because multiple scattering occurs into large angles which

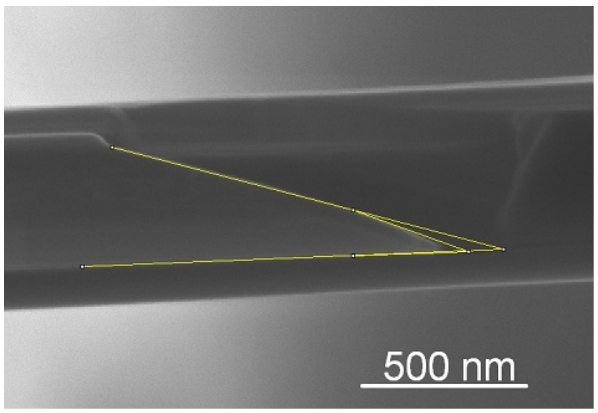

Figure 3.1: Secondary electron SEM image showing top-view perspective of the wedge-shaped a-carbon sample. The yellow lines mark the measured wedge angle: 22° at the thin edge, 18° at larger distance from the edge.

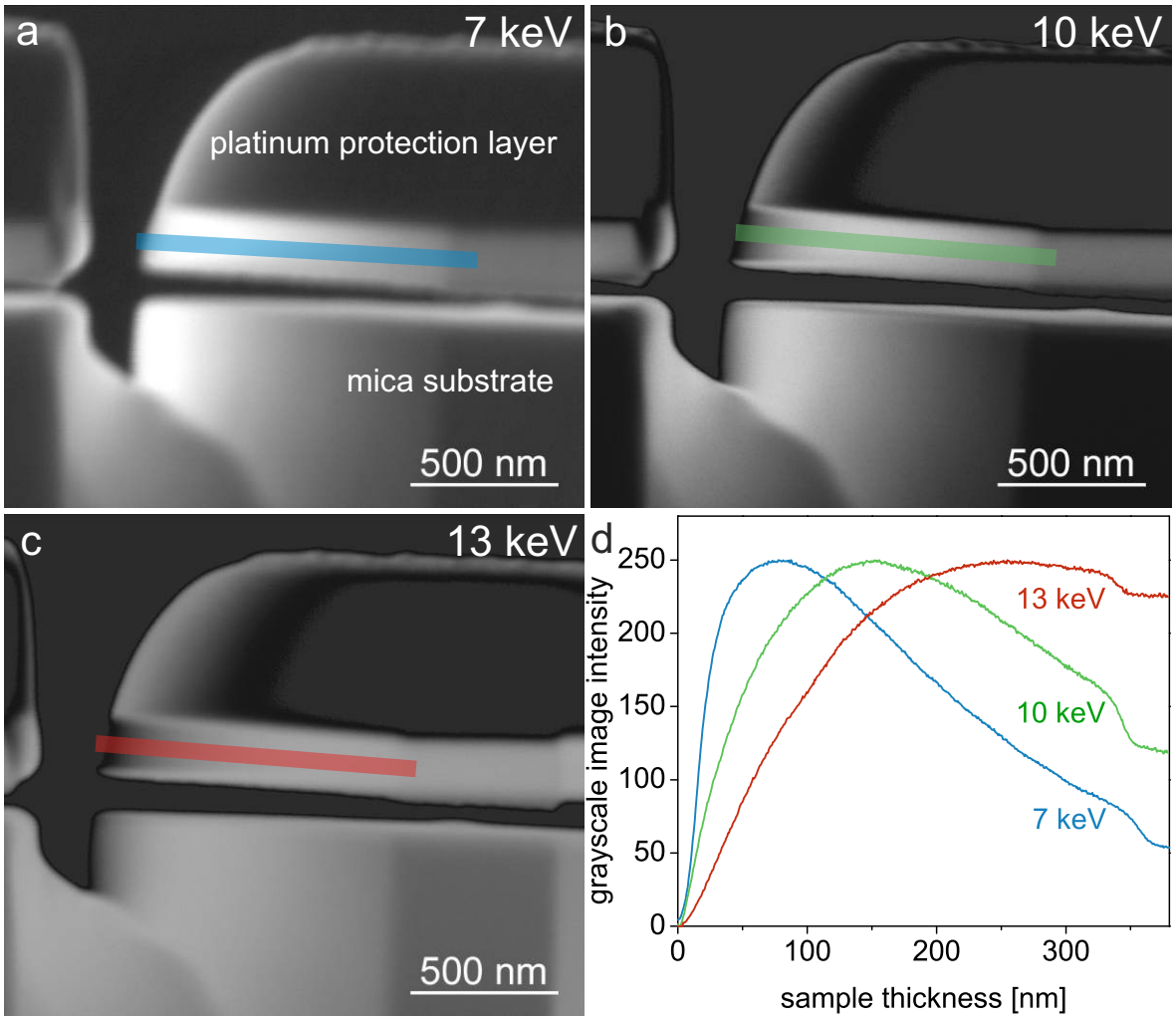

Figure 3.2: a)-c) Cross-section HAADF STEM image of the a-carbon wedge at 7, 10 and 13 keV. The position and the width of the intensity line scan is indicated by the blue, green and red stripes. d) Normalized HAADF STEM intensity as a function of the sample thickness along the line scans in a)-c).

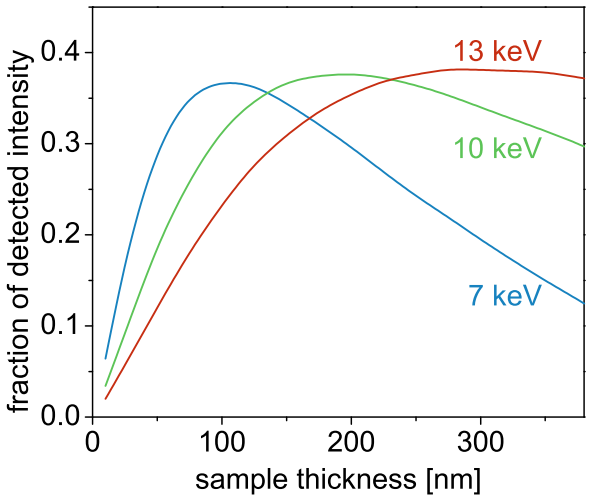

Figure 3.3: MC simulation of the HAADF STEM intensity normalized with respect to the incident intensity I_0 for carbon films plotted against the sample thickness for different electron energies. (For the simulations screened Rutherford cross-sections were employed.)

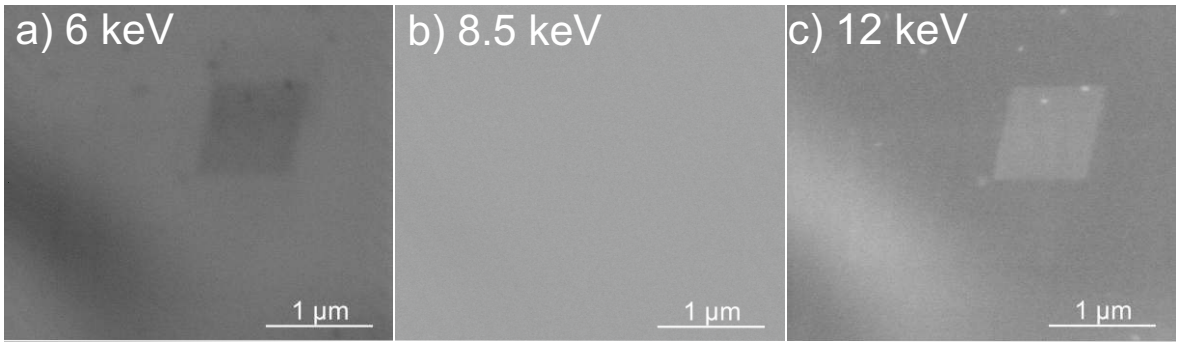

Figure 3.4: HAADF STEM images of a carbon layer with 130 nm thickness, which contains a contaminated, slightly thicker area used for reference. Images are taken at different electron energies.

is accompanied by energy loss. With further increasing thickness, backscattering and absorption reduces the overall number of electrons transmitted through the sample. This leads to the reduction of the HAADF (and also BF) intensity. An example for the intensity reduction beyond the inversion point can be seen in Figs. 3.2a-c. The platinum protection layer of the wedge-shaped carbon sample appears for the most part darker than the carbon, although platinum is characterized by a much higher scattering power. This is due to the inversion point of the HAADF intensity at very small thicknesses, which results in a bright contrast of the Pt layer only at the edge of the wedge-shaped sample.

Contrast inversion can be also observed for a-carbon films with constant thickness if the electron energy is varied. Fig. 3.4 shows HAADF STEM images of the a-carbon film with a homogeneous thickness of 130 nm, taken at different electron energies of 6 keV (Fig. 3.4a), 8.5 keV (Fig. 3.4b) and 12 keV (Fig. 3.4c). A contaminated area with a thickness in the order of a few nm is present in the investigated area. The contamination was produced by scanning the respective area with a higher magnification and a slow scanning rate. The rhombic shape of the area is probably due to drift of the sample during the slow scanning process. The contaminated area appears darker than the rest of the sample for E=6 keV. The contrast disappears completely at 8.5 keV. Contrast inversion is observed for 12 keV where the contaminated area appears brighter than the surrounding carbon films. Minimum contrast is correlated with the maximum of the curves for the HAADF STEM intensity displayed in Fig. 3.2d. Due to the flatness of the curve around the maximum small thickness variations do not induce different HAADF STEM intensities. The maximum HAADF STEM intensity is shifted to larger sample thicknesses at higher electron energy which yields brighter contrast for the contaminated and slightly thicker sample region in Fig. 3.4c. For small electron energies the opposite behavior is observed because the image intensity is determined by the descending branch of the curve. The dark area in the lower left part of Fig. 3.4a results from a local corrugation of the film. In this region the film is not oriented perpendicular to the electron beam, which locally increases the sample thickness.

The electron energy at minimal contrast was determined for all a-carbon thin-film samples with thicknesses between 50 nm and 190 nm and the a-carbon wedge. The data is compiled in Fig. 3.5. The error bars in y-direction take the inaccuracy of the thickness measurement in account. For the carbon films x-error bars are included. They account for the fact that the energy of minimal contrast is determined visually by increasing

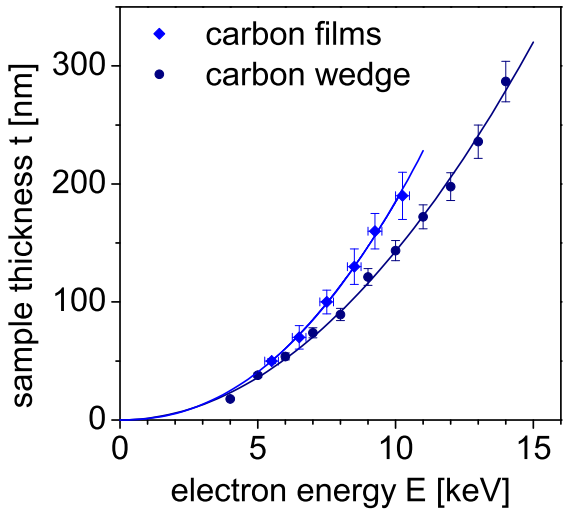

Figure 3.5: Relation between sample thickness and electron energy at the inversion point for a-carbon. Comparison of film samples and the wedge sample. Power-law functions of the form $y=a\cdot x^b$ were used to fit the experimental data.

the energy in steps of 0.25 keV. To find an analytical relation between thickness and electron energy at the contrast inversion point, different basic functions were fitted to the experimental data. The best agreement was found for a power-law function $y=a\cdot x^b$, which is plotted in Fig. 3.5. The fit yields an exponent of b=2.19±0.12 for the a-carbon films and a slightly smaller exponent of b=1.99±0.12 for the a-carbon wedge. The slope of the curves is different although the same material is analyzed. This deviation originates most likely from different sample preparation methods. The carbon wedge was prepared by FIB milling which leads to implantation of Ga and slightly increased values for mean atomic number Z and mean atomic mass number A. Due to this deviation the carbon wedge was not used for a quantitative analysis of the electrons scattering at low electron energies.

HAADF STEM images of the P3HT films with different thicknesses were taken at electron energies between 4 and 15 keV in steps of 0.25 keV. The image in Fig. 3.6a taken at 8 keV shows intensity variations which are related to thickness fluctuations of the film with t=190 nm. The feature in the middle of the image is a dirt particle which was used to align and focus the image after changing the electron energy. For 13 keV(Fig. 3.6c) the contrast of the image is clearly reversed in comparison to the image taken at 8 keV. Minimum contrast occurs for 10.75 keV (Fig. 3.6b).

Thickness and electron energy at the contrast inversion point were determined for all P3HT samples and plotted in Fig. 3.7. The errors bars represent the deviation of the thickness measurements and the inaccuracy of the contrast inversion energy determination. A power-law function with an exponent of b=1.88±0.13 yields the best fit of the experimental data.

The EPON wedge-sample was examined analogously to the carbon wedge. In Fig. 3.8 an HAADF STEM image taken at 10 keV is displayed. Starting at the edge of the wedge the intensity increases, reaches a maximum and then decreases again, which can be seen in the corresponding grayscale intensity line scan in the right part of the figure. The position of the line scan is marked in the HAADF STEM image with an orange stripe. The thickness at the inversion point was determined as a function of the electron energy and plotted in Fig. 3.9. Since the EPON is sensitive towards high-energy electron irradiation, a degradation of the sample during the measurements

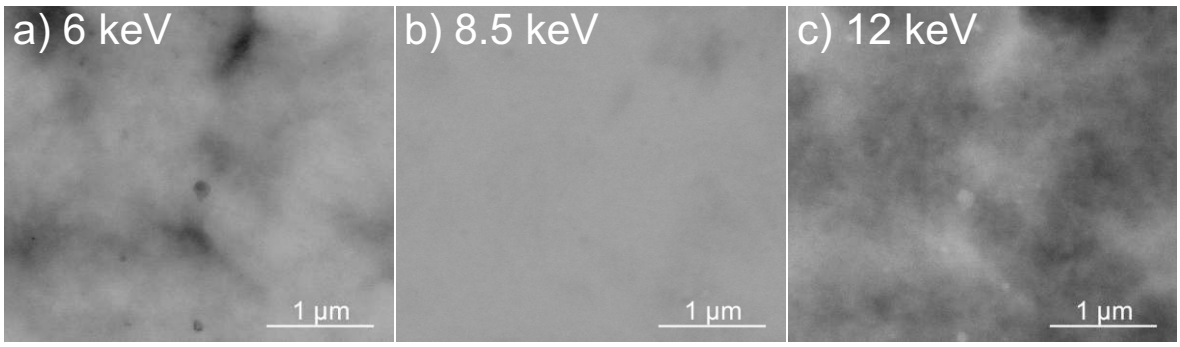

Figure 3.6: HAADF STEM images of a P3HT film with 190 nm thickness taken at different electron energies. The structures visible in a) and c) can be correlated to thickness variations of the film.

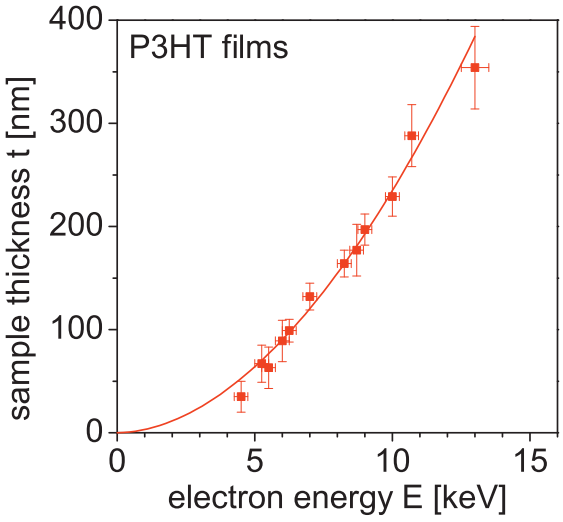

Figure 3.7: Relation between sample thickness and electron energy at the inversion point for P3HT. A power-law function $y=a \cdot x^b$ was used to fit the experimental data.

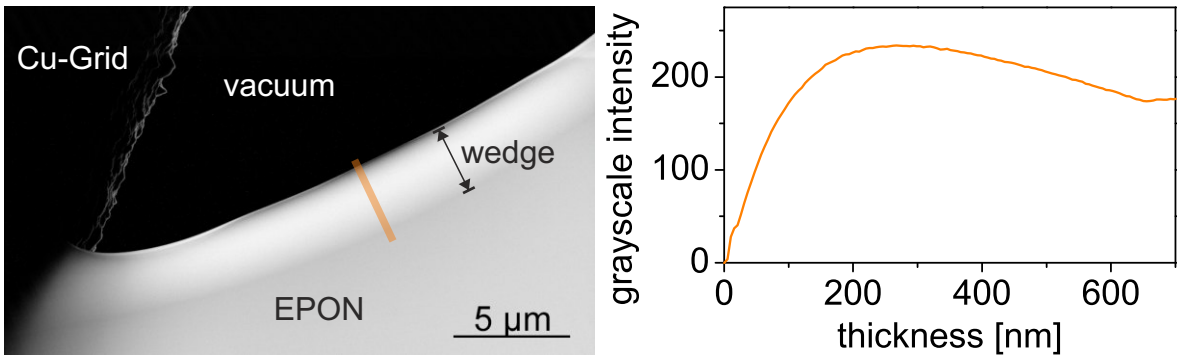

Figure 3.8: HAADF STEM image taken at 10 keV of the EPON wedge. The position of the grayscale intensity line scan on the right is marked with an orange stripe in the HAADF STEM image.

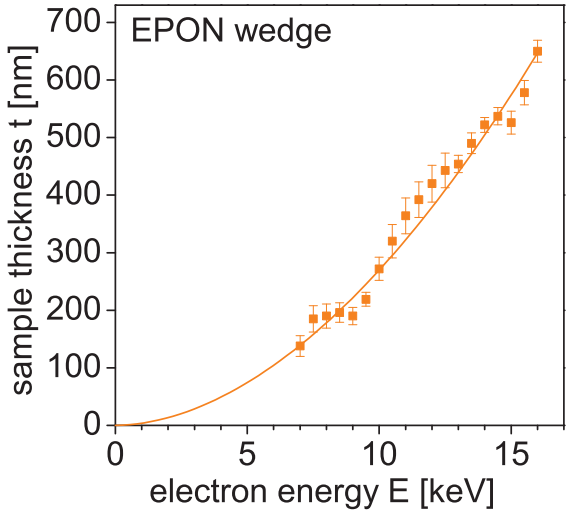

Figure 3.9: Relation between sample thickness and electron energy at the inversion point for EPON. A power-law function $y=a \cdot x^b$ was used to fit the experimental data.

could be observed. To obtain representative results for different electron energies, the position of the measurement was changed frequently. Nevertheless errors caused by this degradation cannot be completely avoided.
The fitted power-law function yields an exponent of $b=1.86 \pm 0.07$.

3.4 Discussion

The experimental data in the previous section clearly shows that a well-defined relationship exists between the electron energy and the sample thickness at the maximum HAADF intensity, which determines contrast inversion. This characteristic behavior can be exploited to analyze low energy electron scattering in a-carbon, P3HT and EPON. Even more interestingly, it serves as a basis for precise thickness determination of electron transparent samples if the composition of the specimen is known. A systematic analysis of the experimental data is presented in the following to elaborate an adequate description for sample thickness determination. For this purpose, the semi-empirical descriptions presented in chapter 3.1.2 are used. The results are compared with MC simulations, described in chapter 3.1.3.

3.4.1 Comparison of experimental data, Monte-Carlo simulations and semi-empirical equations

The electron-energy dependence of the thickness at the inversion point can be well described by a power-law function with an exponent of approximately 2 for all investigated materials. In table 3.2 the values of the fitted exponents are summarized.
First MC simulations were tested, to model the experimental data and determine the thickness at the maximum HAADF intensity as a function of the electron energy applying either Mott or Rutherford differential cross-sections. The results of the MC simulations are displayed in Fig. 3.10. For a-carbon (Fig. 3.10a) both curves for the different cross-sections lie above the measurements. The exponent of the fitted power-law function is 1.66±0.04 for the Mott and 1.70±0.04 for the Rutherford cross-section, which is significantly smaller than the experimentally determined value. For P3HT (Fig. 3.10b) there is also a significant discrepancy between measured data and MC simulations with fit exponents of 1.68±0.03 for the Rutherford and 1.57±0.04 for the Mott cross-sections. Only for EPON (Fig. 3.10c) a reasonable agreement is obtained between measurements and MC simulations applying Rutherford cross-sections with 1.69±0.03. The fit exponent for the Mott cross-section is 1.62±0.03. The fitted exponents of all the MC simulations are summarized in Table 3.2. Apart from EPON, MC simulations based on Mott or Rutherford cross-section are not well suited to describe quantitatively multiple low-energy electron scattering. A larger disagreement exists between the experimental results and the MC simulations based on Mott cross-sections, which is in accordance to the results of other groups (Chapter 3.1.1).
In the following, the experimental data is compared with the predictions based on

samples	experimental data	MC simulation with Rutherford cross-sections	MC simulation with Mott cross-sections
a-carbon (films)	2.19±0.12	1.70±0.04	1.66±0.04
P3HT	1.88±0.13	1.68±0.03	1.57±0.04
EPON	1.86±0.07	1.69±0.03	1.62±0.03

Table 3.2: Exponent of the fitted power-law function for the experimental data and the MC simulations, applying Rutherford and Mott cross-sections

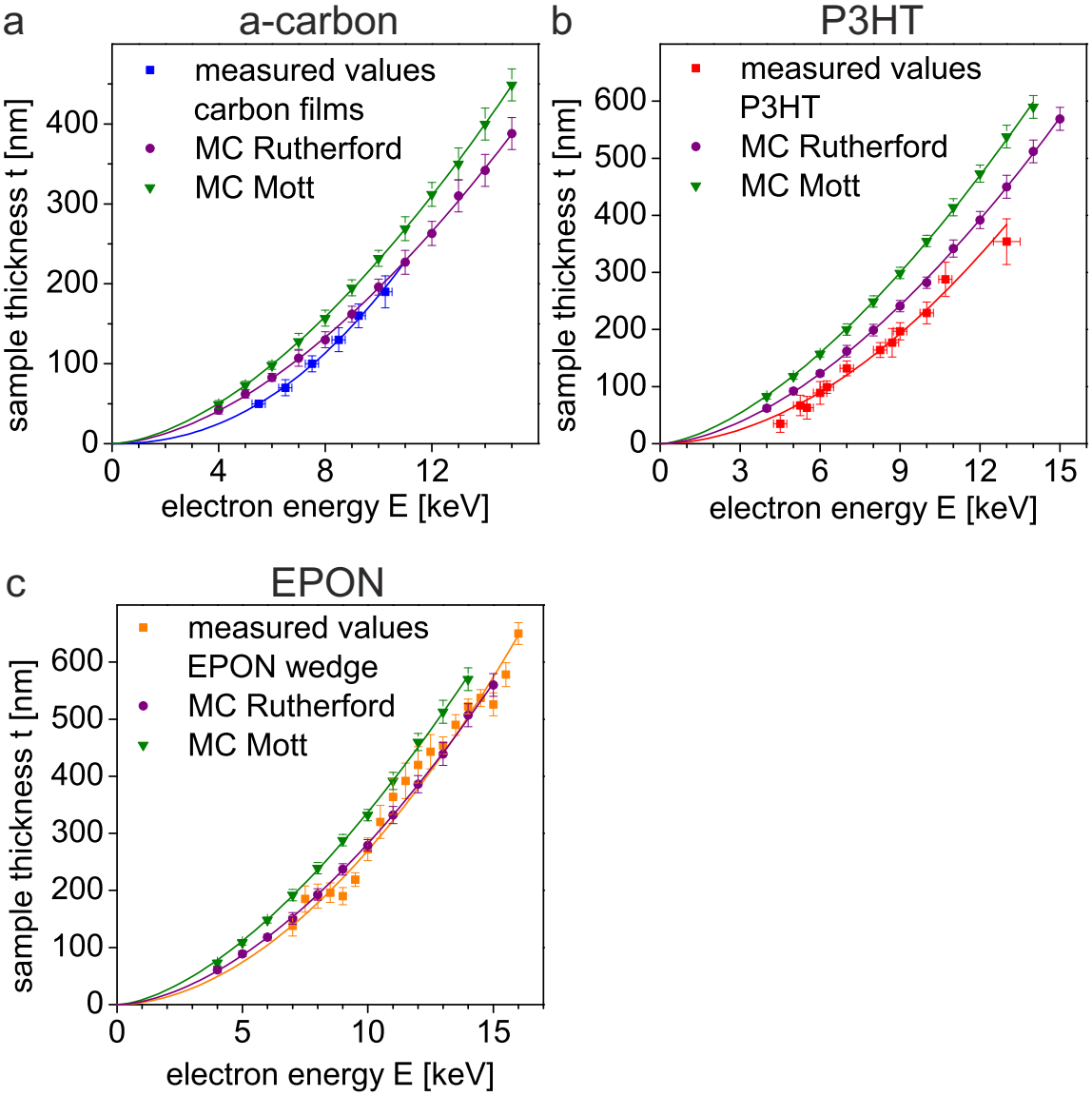

Figure 3.10: Relation between sample thickness and electron energy at the inversion point for a-carbon (film samples), P3HT and EPON. Comparison of experimental data with MC simulations (Mott and Rutherford cross-sections).

the semi-empirical equations of Cosslett & Thomas (Eq. 3.7) and Bothe (Eq. 3.6). To obtain an analytical expression for the maximum HAADF STEM intensity as a function of energy and thickness Eq. 3.5 is integrated over the relevant scattering angle range. As a result the normalized HAADF intensity can be written as

$$\frac{I_{\mathrm{HAADF}}}{I_0} = e^{-\theta_1^2/2\overline{\theta^2}} - e^{-\theta_2^2/2\overline{\theta^2}}, \tag{3.11}$$

with the mean quadratic scattering angle $\overline{\theta^2}$ and the angles θ_1 and θ_2, which denote the minimal and maximal scattering angle covered by the HAADF STEM detector. To find the maximum of the HAADF STEM intensity, this function has to be differentiated

material	Z_m	A_m
P3HT	5.02	6.65
EPON	4.81	7.51

Table 3.3: Mean atomic number Z_m and mean atomic mass number A_m of P3HT and EPON.

with respect to $\overline{\theta}$. The following expression of the mean quadratic scattering angle is obtained:

$$\overline{\theta^2} = \frac{\theta_1^2 - \theta_2^2}{4 \ln(\theta_1/\theta_2)} \tag{3.12}$$

Substitution of $\overline{\theta^2}$ by the expression suggested by Cosslett & Thomas (Eq. 3.7) in Eq. 3.12 leads to the following equation which relates the thickness t at maximum HAADF STEM intensity with the electron energy E:

$$t = \frac{\theta_1^2 - \theta_2^2}{4 \ln(\theta_1/\theta_2)} \cdot \frac{A}{Z^{1.5} \cdot \rho \cdot 1.2 \cdot 10^6} \cdot E. \tag{3.13}$$

This equation suggests a linear relation between sample thickness and electron energy at the contrast inversion point, which does not adequately describe the exponent of the power-law functions for the experimental results. It can be concluded that Eq. 3.7 and therefore Eq. 3.13 are not well suited to describe multiple electron scattering in low Z materials at low electron energies.
Substitution of $\overline{\theta^2}$ in Eq. 3.12 by the expression suggested by Bothe (Eq. 3.6) yields

$$t = \frac{\theta_1^2 - \theta_2^2}{4 \ln(\theta_1/\theta_2)} \cdot \frac{A}{Z^2 \cdot \rho \cdot 12.96 \cdot 10^9} \cdot E^2, \tag{3.14}$$

which suggests that the thickness at the inversion point is proportional to E^2. This is in a good agreement with the experimentally determined exponents. However, for a-carbon the calculated curve lies considerably below the measured data, which is shown in Fig. 3.11a.
To plot Eq. 3.14 the atomic number Z and the atomic mass number A is needed. Since P3HT and EPON consist of more than one element, mean values have to be calculated. For the atomic number, the root mean square is used. This is due to the fact that the screened Rutherford cross-section (on which the Bothe equation is based) contains Z^2. Since the cross-sections of the different atoms are added, the root mean square seems expedient. The atomic mass number is not contained in the cross-section. It is related to the mean free path length and therefore appears in the Bothe equation (Eq. 3.6). Since it is a linear factor, the arithmetic mean value is used for further calculations. In Table 3.3 the values for the sample materials are given.
Eq. 3.14 is plotted for P3HT and EPON in Figs. 3.11b and c. For both materials the calculated curve lies considerably below the experimental data. The original Bothe expression is therefore not suitable to describe high-angle scattering in low-Z materials at low electron energies. Nevertheless the equation shows the right E^2 dependency and the dircrepancy with respect to the measurements is in the same order of magnitude for all examined materials. This indicates that the introduction of a correction factor in the equation could be beneficial.

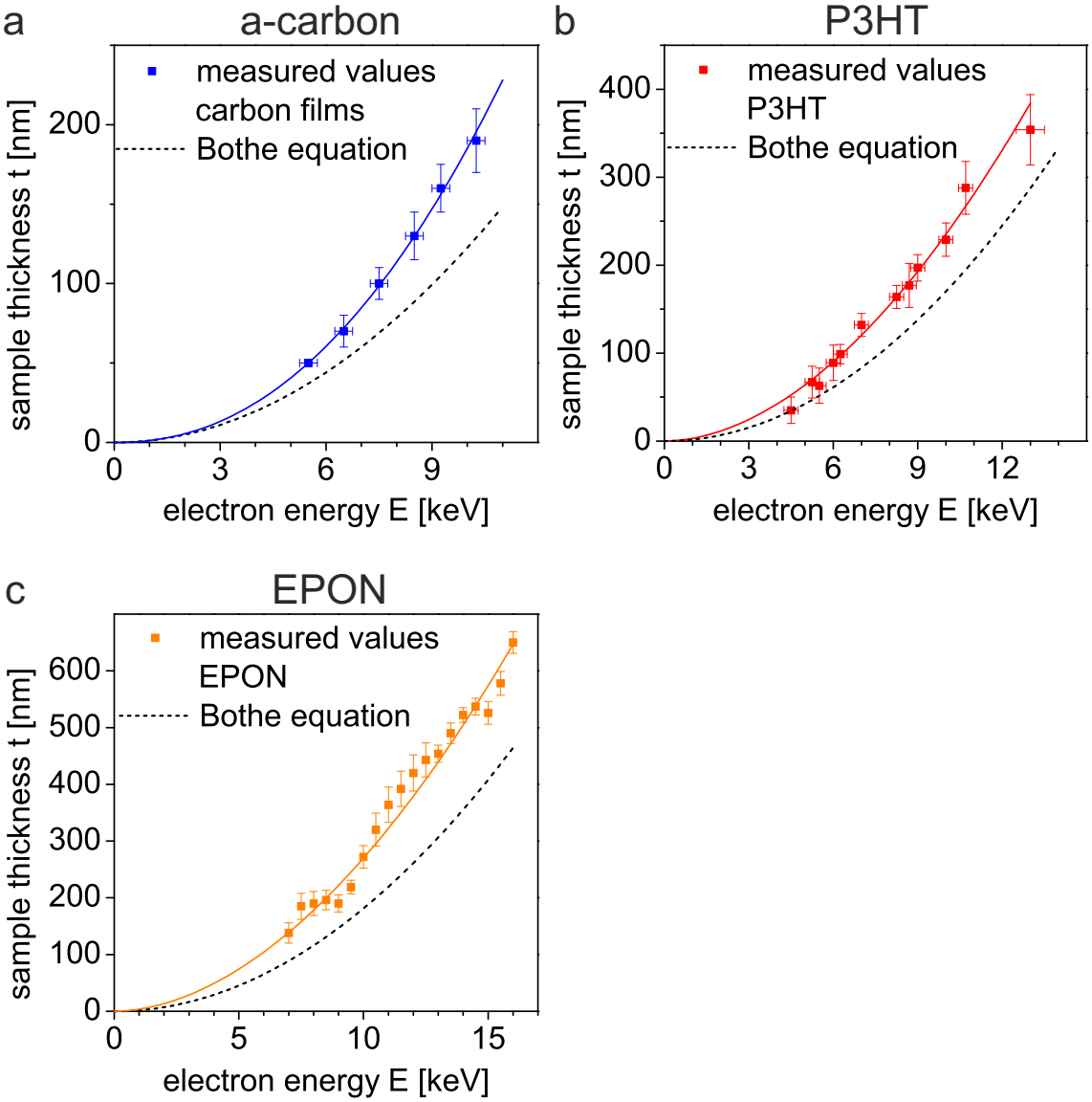

Figure 3.11: Relation between sample thickness and electron energy at the inversion point for a) a-carbon (film samples), b) P3HT and c) EPON. Comparison of experimental data with the Bothe equation

To adjust Eq. 3.14 to the measurements a correction factor CF is introduced:

$$t = \frac{\theta_1^2 - \theta_2^2}{4 \ln(\theta_1/\theta_2)} \cdot \frac{A}{Z^2 \cdot \rho \cdot \mathrm{CF} \cdot 10^9} \cdot E^2, \tag{3.15}$$

In the original equation CF is 12.96. Bothe himself adjusted this value to obtain optimum agreement with experimental data. To find the best correction factor for our measurements, a cubic function was fitted to the experimental data. The slope of the curve can then be identified with the prefactor of E^2 in Eq. 3.15. It is therefore possible to calculate CF for every sample material. The results are shown in table 3.4.

As the correction factors for the different materials are similar, an averaged correction factor of 9.15 is proposed for the description of electron scattering in low Z materials for

material	CF
a-carbon	9.35±1.48
P3HT	9.15±0.89
EPON	9.11±0.77

Table 3.4: Adjusted correction factors CFs for a-carbon, P3HT and EPON.

low electron energies between 4 and 15 keV. The comparison of the measured relation between electron energy and sample thickness at the inversion point and the calculated curves with the adjusted correction factor is summarized in Fig. 3.12.
The mean quadratic scattering angle can now be calculated by the following equation [159]:

$$\overline{\theta^2_{\mathrm{CF}}} = 9.15 \cdot 10^9 \left(\frac{Z}{E}\right)^2 \frac{\rho t}{A} \qquad [\mathrm{rad}^2]. \tag{3.16}$$

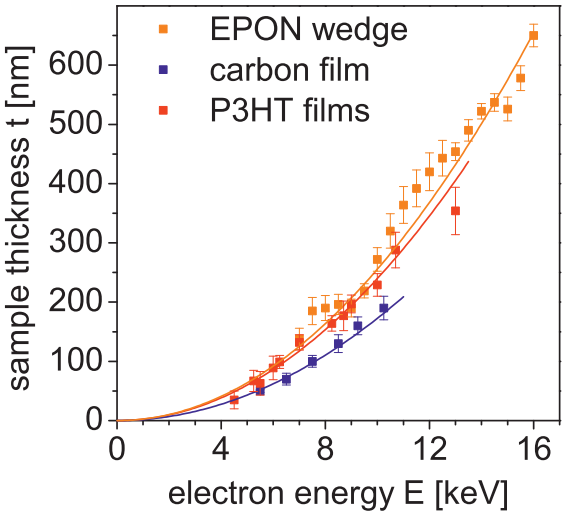

Figure 3.12: Relation between sample thickness and electron energy at the inversion point for amorphous carbon, P3HT and EPON. Comparison of experimental data (squares) and curves calculated on the basis of Eq. 3.15 with CF=9.15.

3.4.2 Applications of the semi-empirical equation

The adjusted semi-empirical equation of Bothe can now be used to calculate HAADF STEM intensities. Due to the contrast inversion described in Chapter 3.3, it is not possible to intuitively interpret HAADF STEM images. In this context the calculations are particularly useful. They enable a correlation of sample composition to image intensities for a certain electron energy and sample thickness. To get the HAADF STEM intensities, the mean quadratic scattering angle (Eq. 3.16) has to be inserted into Eq. 3.11. Examples for HAADF STEM intensity calculations will be shown in Chapters 4.2 and 5.2.2.
Another application of the semi-empirical equation is the determination of either the sample thickness or the density of the sample material. For thickness determination all sample parameters like composition and density have to be known. Experimentally, the electron energy is adjusted to achieve minimum contrast. Eq. 3.15 with a correction factor of 9.15 then yields the sample thickness. The precision of this method for sample thickness determination depends strongly on the accuracy of the sample parameters. If these parameters are well known and the energy at contrast inversion point can be determined with an error of less than ±5 % the error of the calculated thickness is smaller than ±10 %.

For density determinations Eq. 3.11 has to be rearranged:

$$\rho = \frac{\theta_1^2 - \theta_2^2}{4 \ln(\theta_1/\theta_2)} \cdot \frac{A}{Z^2 \cdot t \cdot \mathrm{CF} \cdot 10^9} \cdot E^2 \tag{3.17}$$

Theoretically it is sufficient to determine the contrast inversion energy for one sample with a precisely known thickness. To enhance the quality and the reliability of the measurement it is nevertheless useful to examine a set of samples with various thicknesses. Examples for this density determination method will be shown in Chapter 5.2.1.

4 Nanomorphology of poly(3-hexylthiophene-2,5-diyl)-based organic solar cell absorber layers

In the following chapter the investigation of P3HT:$PC_{61}BM$ absorber layers of organic solar cells is presented. The nanomorphology of P3HT:$PC_{61}BM$ blends was studied as a function of the processing parameters and for P3HT with different molecular weight (MW). For this purpose STEM at low electron energies was applied in a scanning electron microscope. This method exhibits sensitive material contrast in the HAADF mode, which is well suited to distinguish materials with similar densities and mean atomic numbers. The images taken with low-energy HAADF STEM are compared with conventional TEM and atomic force microscopy images to illustrate the capabilities of the different techniques. For the interpretation of the low-energy HAADF STEM images, the semi-empirical equation developed in Chapter 3 is used to calculate the image intensities. The experiments show that the nanomorphology of the P3HT:$PC_{61}BM$ blends depends strongly on the MW of the P3HT. Low-MW P3HT forms rod-like domains during annealing. In contrast, only small globular features are visible in samples containing high-MW P3HT, which do not change significantly after annealing at 150 °C up to 30 min.

4.1 Materials and methods

Samples

Solar-cell absorber layers were fabricated by M. Klein (LTI, KIT). The samples were prepared under inert conditions on indium tin oxide-coated glass substrates. After depositing a 45 nm layer of PEDOT:PSS (Clevios VPAI4083, Heraeus), the polymer:fullerene solution was spin-coated at 1000 rpm for 70 s. For all sets of samples, P3HT:$PC_{61}BM$ with a mixture of 1:1 was dissolved in DCB (anhydrous, 99.8%, Sigma-Aldrich). Different P3HT batches were used with a weight average molecular weight of M_w=20 kg/mol and M_w=50 kg/mol purchased from Rieke Metals. $PC_{61}BM$ (99.5%) was purchased from Solenne BV. Annealing treatments were carried out at at 150 °C for up to 30 min. The thickness of the samples was measured with a Bruker Dektak XT profilometer (Bruker). The thickness was 92±13 nm for the 20 kg/mol samples and 100±14 nm for the 50 kg/mol samples. Additional P3HT:$PC_{61}BM$ samples (50 kg/mol) were prepared that were dried slowly after spin-coating by storing them in a petri dish according the so-called solvent annealing process described in Chapter 1.4.1. The thickness of these samples was 126±46 nm.
Plan-view samples of the photoactive layers were prepared by the procedure described in Chapter 2.1.1.

Instrumentation

Conventional BF TEM images were taken in a Philips CM200 FEG/ST at 200 keV with a liquid nitrogen cooling holder and a small objective aperture. Low-keV STEM imaging was carried out in a FEI Strata 400S dual-beam SEM. It is equipped with a 16-bit semiconductor STEM II detector, which is positioned below the sample holder. The design of the detector is described in detail in Chapter 2.3. Images were taken with a working distance of 5 mm, which corresponds to a collection scattering-angle range between 0.2 and 0.7 rad. All images were taken with the same contrast and brightness settings to ensure comparability. The contrast of some images was enhanced by setting the minimum (black) and maximum (white) image intensities according to the minimum and maximum gray values of the histogram. The same postprocessing was performed if images are directly compared.
AFM topography images were taken with an Asylum Research MFP-3D in the AC mode.

4.2 Calculation of the low-keV high-angle annular dark-field scanning transmission electron microscopy intensity

The interpretation of low-keV HAADF STEM images requires the calculation of the image intensity for the examined materials. For this purpose the semi-empirical description of electron scattering in low Z materials at low energies developed in Chapter 3 is employed. The exact procedure of the HAADF STEM intensity calculation is described in detail in Chapter 3.4.2.

Table 4.1 lists the material parameters of $PC_{61}BM$ and P3HT, which were used to calculate the HAADF STEM intensity. A P3HT density of 1080 kg/m^3 was used for the calculations. It was measured by He-pycnometry for P3HT with a MW of 43 kg/mol. In the literature a value of 1100±50 kg/m^3 is reported, but the MW of the P3HT is not mentioned in this work [166]. The influence of the MW on the density is therefore not known. However, Eq. 3.16 depends only linearly on the density, and a small deviation would only slightly change the results. The calculation of the mean square scattering angle $\overline{\theta^2_{\mathrm{CF}}}$ according to equation Eq. 3.16 requires for each component the average atomic mass number A given by the weighted arithmetic mean of the atomic mass numbers of the elements and the mean atomic number Z given by the weighted root-mean-square (Chapter 3.4.1).

Fig. 4.1a shows the normalized HAADF STEM intensity for $PC_{61}BM$ and P3HT as a function of the primary electron energy up to 15 keV for a sample thickness of 100 nm, which corresponds to the thickness of the majority of samples. An intensity maximum can be observed at a specific electron energy that depends on the material. The maximum for P3HT lies at 6.25 keV and for $PC_{61}BM$ at 6.75 keV. The graph also shows that the distinction between $PC_{61}BM$ and P3HT is promising at energies above approximately 9 keV for a sample thickness of 100 nm. According to the calculations, $PC_{61}BM$ should be visible with higher image intensity than P3HT at electron energies above approximately 6.5 keV. The dependence of the HAADF STEM intensity on the P3HT thickness is shown in Fig. 4.1b for four different electron energies (4.5, 6, 10, and 15 keV), where the position of the intensity maximum shifts toward larger sample thicknesses. The general behavior of the HAADF STEM intensity as a function of the thickness can be understood in the following way. The large-angle scattering probability is low for thin samples leading to low HAADF STEM intensities. More electrons contribute to the HAADF STEM signal with increasing sample thickness because multiple scattering occurs into large scattering angles. With further increasing thickness, backscattering reduces the overall number of electrons, which are transmitted through the sample. This leads to the reduction of the HAADF (and also BF) intensity beyond the intensity maximum. A verification of the energy dependence of the calculated HAADF STEM intensity (Fig. 4.1a) for a sample thickness of 100 nm is presented in Fig. 4.2, which shows images of a P3HT:$PC_{61}BM$ absorber layer taken

material	chemical formula	density [kg/m^3]	Z_{m}	A_{m}
P3HT	$C_{10}H_{14}S$	1080	5.02	6.65
$PC_{61}BM$	$C_{72}H_{14}O_2$	1600	5.57	10.35

Table 4.1: Material parameters of P3HT and $PC_{61}BM$. The two densities were measured with helium pycnometry.

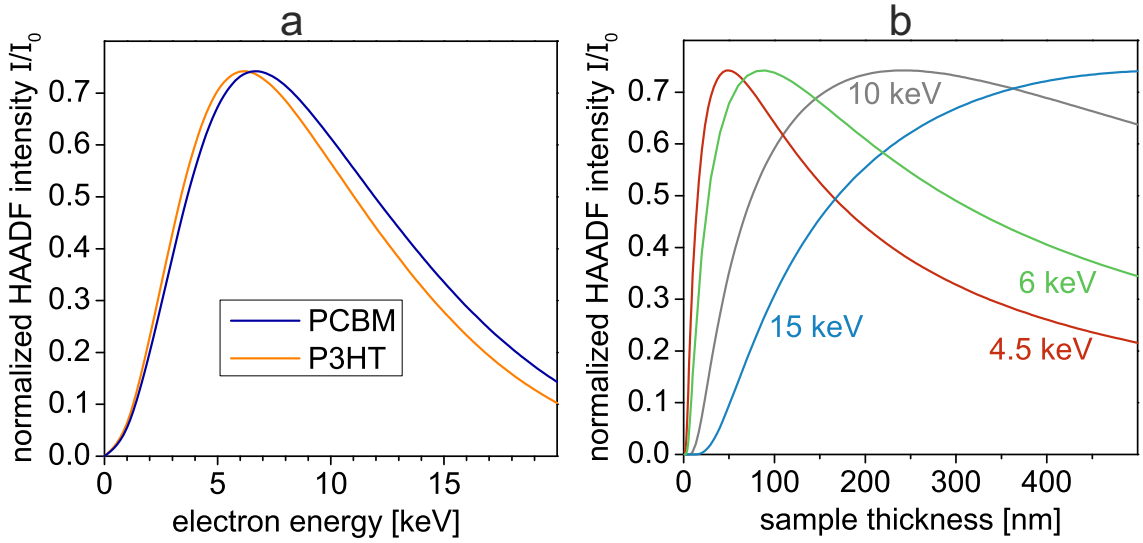

Figure 4.1: Calculated HAADF STEM intensity for a) PC$_{61}$BM and P3HT as a function of the electron energy for films with a thickness of 100 nm and b) P3HT as a function of the sample thickness for different electron energies.

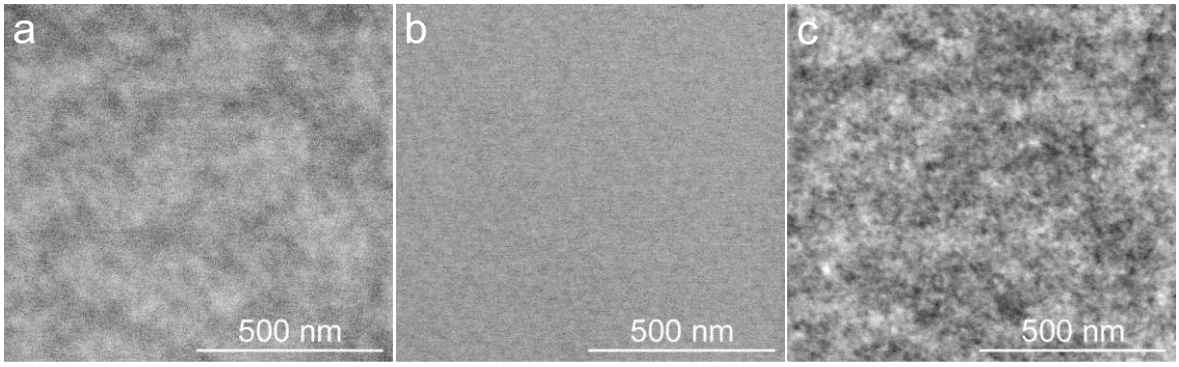

Figure 4.2: HAADF STEM images of the same region of a 50 kg/mol P3HT:PC$_{61}$BM sample annealed for 10 min at 150 °C showing the energy-dependent contrast. For 4.5 keV (a) P3HT appears brighter than PC$_{61}$BM, whereas the image intensity is reversed at 15 keV (c). Minimum contrast occurs at 6 keV (b), where P3HT and PC$_{61}$BM exhibit the same image intensity.

at 4.5, 6, and 15 keV. The contrast of these images was enhanced by postprocessing to obtain the highest possible contrast. The predicted contrast inversion is clearly visible. It is related to the superposition of material and thickness contrast inversion according to the shape of the curves in Fig. 4.1a and Fig. 4.1b for the thickness dependence. For 4.5 keV (Fig. 4.2a), slightly thicker regions of the sample (with lateral sizes between 100 and 500 nm) appear darker because of the negative slope of the curve (see Fig. 4.1b). For 15 keV (Fig. 4.2c), the slope is positive and thicker regions appear brighter. Fig. 4.2c contains in addition features related to material contrast on a scale of only a few 10 nm. These features cannot be resolved at 4.5 keV in Fig. 4.2a where the resolution is reduced compared to 15 keV. The loss of resolution is related to the larger electron-beam diameter at lower electron energy and stronger beam broadening due to smaller mean-free-path lengths for elastic and inelastic scattering. For 15 keV (Fig. 4.2c), PC$_{61}$BM appears brighter than P3HT. Minimum contrast occurs at 6 keV

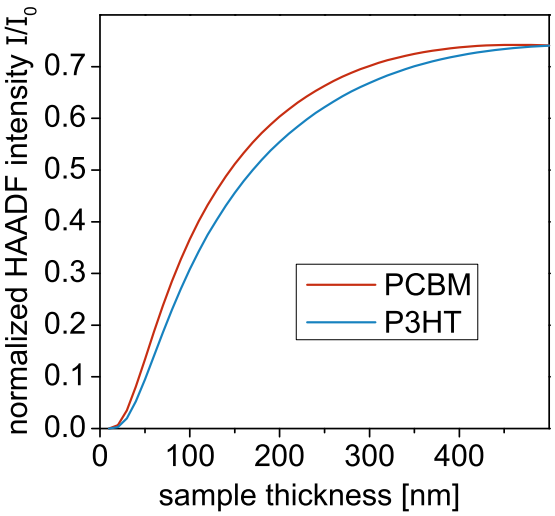

Figure 4.3: Calculated HAADF STEM intensity as a function of the sample thickness for P3HT and $PC_{61}BM$ and a fixed electron energy of 15 keV.

(Fig. 4.2b), where P3HT and $PC_{61}BM$ exhibit the same image intensity. This agrees well with the prediction from Fig. 4.1, where a crossing of the P3HT and $PC_{61}BM$ curves is observed at 6.5 keV. The small deviation between the experimental and predicted electron energy for minimum contrast can be explained by the variation of the sample thickness and the error for the determination of the electron energy at minimum contrast. Since the curves in Fig. 4.1 are relatively flat in the vicinity of the maxima and lie close together for P3HT and $PC_{61}BM$, images with low contrast are achieved over an extended energy range.

In Fig. 4.3 the calculated HAADF STEM intensity is presented as a function of the sample thickness for P3HT and $PC_{61}BM$ at 15 keV, which was the applied electron energy in this study. At this electron energy, $PC_{61}BM$ is expected to provide a higher HAADF STEM intensity compared to P3HT up to a sample thickness of 500 nm where contrast inversion occurs. Hence, $PC_{61}BM$ appears with bright contrast in a P3HT:$PC_{61}BM$ blend.

It must be emphasized that calculations of the HAADF STEM intensity are essential for the identification of different materials because contrast inversion occurs as a function of sample thickness and electron energy. Moreover, intensity changes due to sample thickness variations must be carefully distinguished from material contrast. Large-scale contrast fluctuations are emphasized, e.g., in Fig. 4.2a due to the reduction of resolution that can be correlated with thickness variations of the absorber layer. The sensitivity toward contrast contributions due to sample-thickness changes can be estimated from the gradient of the P3HT and $PC_{61}BM$ curves in Figs. 4.1b and 4.3. Minimization of contrast contributions due to thickness changes requires a small gradient of the intensity versus thickness curves in the range of relevant sample thicknesses between 70 and 150 nm. From this point of view, an electron energy of 15 keV is preferable compared to smaller electron energies. Fig. 4.1 demonstrates that sufficient contrast between P3HT and $PC_{61}BM$ can be expected at 15 keV for the relevant sample thicknesses in this study. Taking into account the degradation of resolution with decreasing electron energy, 15 keV can be considered as a good compromise between chemical contrast, (in)sensitivity toward thickness changes, and resolution. For higher electron energies the overall HAADF STEM intensity decreases, which leads to a degradation of the signal-to-noise ratio, as can be inferred from Fig. 4.1a.

4.3 Results and discussion

Fig. 4.4 presents a low-keV HAADF STEM and conventional BF TEM images to demonstrate the differences between the two imaging techniques. As segregation of $PC_{61}BM$ and P3HT should be most pronounced for low-MW P3HT after a sufficiently long annealing treatment, the 20 kg/mol sample annealed for 10 min at 150 °C was chosen. It is noted that the images shown in Fig. 4.4 are not taken at the same position. Fig. 4.4a presents a low-keV HAADF STEM image taken at 15 keV, which shows elongated dark features (encircled) and globular features. The calculation of the STEM intensity predicts a higher intensity for $PC_{61}BM$ compared to P3HT (Fig. 4.3) at 15 keV which suggests that dark features correspond to P3HT-rich regions. Practically,

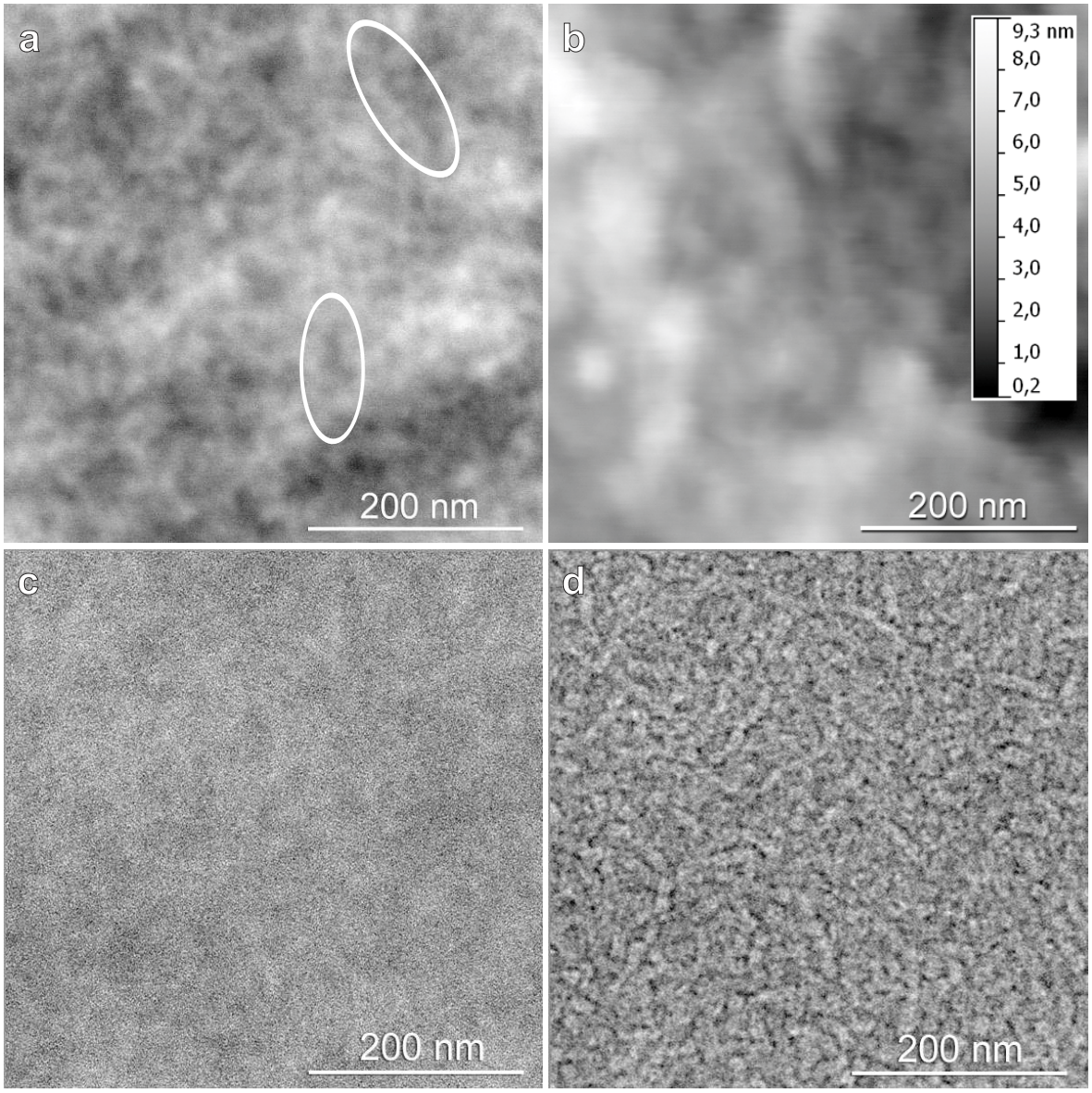

Figure 4.4: 20 kg/mol P3HT:$PC_{61}BM$ sample annealed for 10 min at 150 °C. a) HAADF STEM image taken at 15 keV with examples for P3HT nanorods encircled; b) AFM topography image; c) in-focus TEM image taken at 200 keV, and d) TEM image at 200 keV with an underfocus of 10µm.

the contrast between P3HT and $PC_{61}BM$ is reduced compared to the calculations due to the sample thickness of 92 nm and the corresponding superposition of contrast from $PC_{61}BM$ and P3HT domains along the electron-beam direction. Nevertheless, high contrast is observed between the two materials. Moreover, a distinction has to be made between small-scale and large-scale intensity fluctuations. The latter can be ascribed to thickness variations as will be further outlined in context with Fig. 4.8. Fig. 4.4b shows an AFM image of the same sample, which was acquired to exclude thickness changes as a possible cause for the small-scale intensity variations. Structures, which are significantly larger than the small-scale features in the HAADF STEM image, can be seen in the AFM topography image. The height of these structures is in the range of only a few nm. This excludes thickness variations as a cause for the small-scale contrast features in the HAADF image. Two TEM images taken at 200 keV and different defocus values Δf are shown in Figs. 4.4c and d for comparison. The in-focus TEM image (Fig. 4.4c) does not show any pronounced structural features. The elongated features become only visible at a large underfocus value of $\Delta f = -10\mu m$ (Fig. 4.4c).

The contrast of the TEM images can be understood by considering the absorber layers as weak-phase objects in a first approximation. Only a small phase shift is imposed on the electron wave due to the interaction with a sample that contains materials with small and similar densities and average atomic numbers. Large Δf values are generally

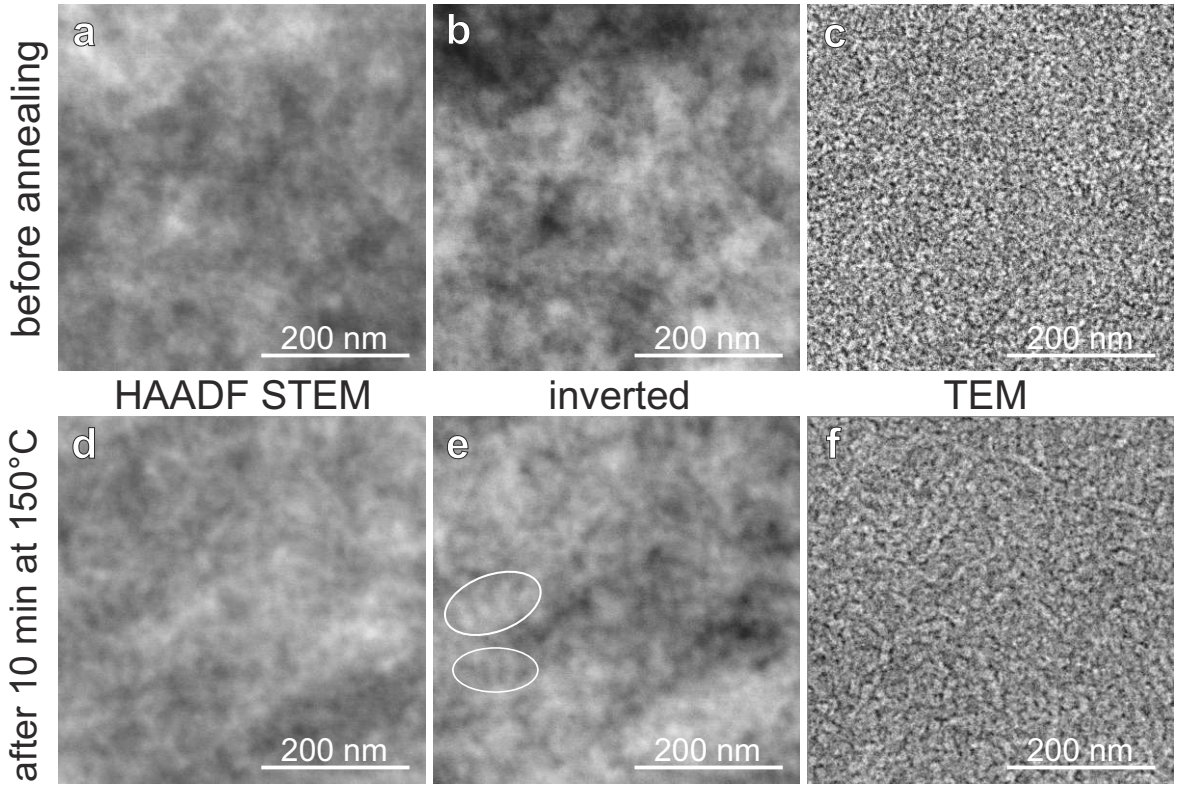

Figure 4.5: 20 kg/mol P3HT:$PC_{61}BM$ sample: a-c) show the as-cast sample, d-f) the sample annealed for 10 min at 150 °C. a) and d) HAADF STEM images taken at 15 keV (P3HT appears dark); b) and e) inverted HAADF STEM image (P3HT appears bright); c) and f) TEM images taken at 200 keV and an underfocus of 10 µm. Examples of P3HT nanorods are encircled in image e).

required to generate contrast between $PC_{61}BM$ and P3HT domains in TEM images [79]. At large defocus values the phase of the scattered electrons at small spatial frequency is shifted by about 90° with respect to unscattered electrons. The required Δf values depend on the typical feature sizes in the sample. Hence, for the examined sample the required Δf values are rather large in the range of a few µm. Choosing large Δf values degrades the resolution to a few nanometers and leads to strong delocalization of image information that impedes the interpretation of the TEM images and an accurate size determination of the structural features. Moreover, superposition of weak contrast from structural features with small size occurs along the electron-beam path. For a sample thickness of 92 nm, the distinction of the nano-scaled features in the two-dimensional projection of the TEM image is therefore even more impeded in TEM images.

The influence of annealing on the nanomorphology of low-MW P3HT:$PC_{61}BM$ samples is demonstrated in Fig. 4.5. Fig. 4.5a-c presents HAADF STEM and BF TEM images of the sample before annealing and Fig. 4.5d-f after 10 min annealing at 150 °C. In the left column HAADF STEM images taken at 15 keV are shown. For this electron energy and a sample thickness of 92 nm, P3HT appears darker than $PC_{61}BM$ (see Fig. 4.3). As the eye is more adapted to recognize bright structures, the inverted HAADF images are shown in the middle column for better visualization of the P3HT domains. In the as-spincast sample diffuse, globular P3HT domains with sizes of few 10 nm are visible, whereas nanorod-like structures indicated by circles are formed in the annealed sample. For comparison, strongly defocused TEM images taken at 200 keV are shown in the right column. The structural change induced by the annealing treatment is also visible in these images. The elongated features, which are observed in the BF TEM image (Fig. 4.5f), are commonly interpreted in the literature in terms of P3HT nanocrystallites [110][111][141]. As mentioned in Chapter 1.4.2 these crystals are formed by π-π stacking of the P3HT chains during annealing [167].

The presence of π-π stacked crystals is confirmed by electron diffraction measurements. In Fig. 4.6 the contrast-inverted diffraction patterns of the as-cast and the annealed 20 kg/mol sample are shown. A broad $PC_{61}BM$ and a sharp P3HT reflection ring is visible in both images (at 2.28 and 2.65 nm^{-1}). In Fig. 4.7 the radially-averaged intensity linescans of the diffraction patterns are displayed. The background in form of a Lorentz curve was subtracted from the original data to enhance the visibility of the

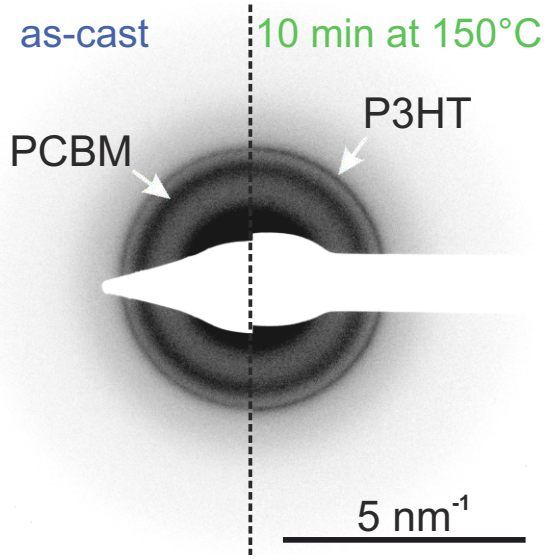

Figure 4.6: Contrast-inverted diffraction pattern of the 20 kg/mol P3HT:$PC_{61}BM$ sample before and after annealing for 10 min at 150 °C.

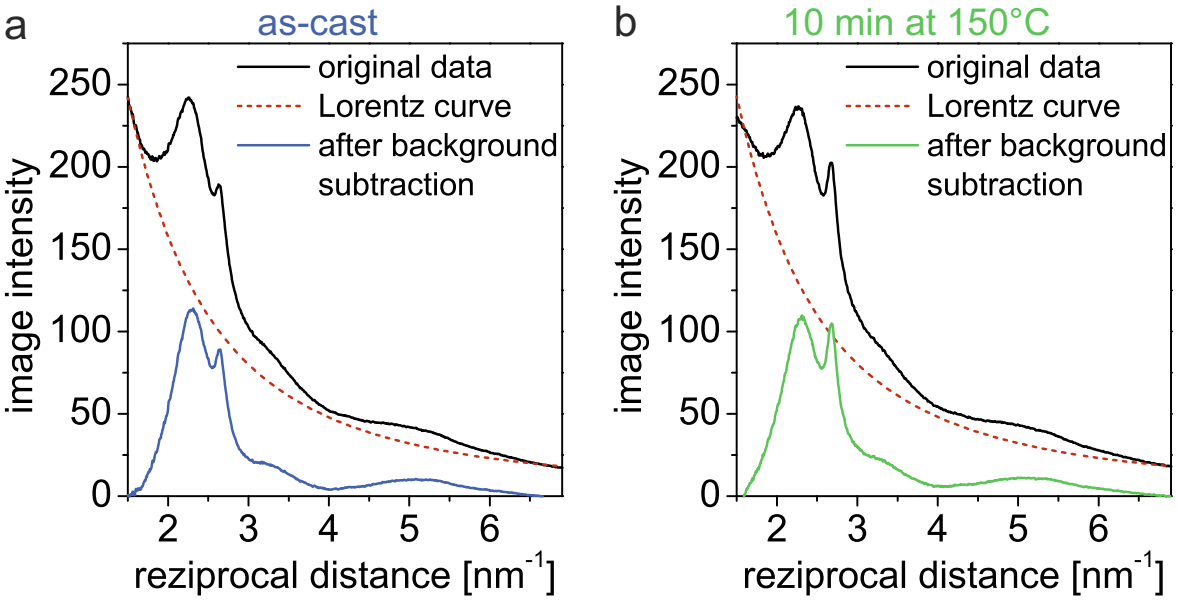

Figure 4.7: Radial linescans of the diffraction patterns of the 20 kg/mol P3HT:$PC_{61}BM$ samples: a) as-cast, b) annealed for 10 min at 150 °C.

Bragg reflections. The intensity of the P3HT reflection at 2.65 nm^{-1} increases during annealing, which confirms that the elongated features in this sample are indeed P3HT crystals. The height of the $PC_{61}BM$ peak at 2.28 nm^{-1} is unaffected by the annealing treatment, which indicates that no larger $PC_{61}BM$ crystals are formed.

In Fig. 4.8 HAADF STEM images of differently prepared 50 kg/mol P3HT:$PC_{61}BM$ films are presented. A TEM image is shown for comparison. Fig. 4.8a shows the sample prior to annealing and Fig. 4.8c after annealing at 150 °C for 30 min. The contrast of these two images was enhanced by postprocessing in the same manner to ensure comparability. Both samples exhibit small globular features with sizes of a few 10 nm that are not influenced by the annealing treatment. This indicates a low degree of phase separation with $PC_{61}BM$ and P3HT being present as a rather homogeneous mixture. The sample thickness of the as-spincast film (Fig. 4.8a) is homogeneous as can be inferred from the absence of large-scale intensity fluctuations. After annealing (Fig. 4.8c), intensity variations occur on a lateral scale larger than 100 nm, which are indicative of thickness variations. For example, the higher average intensity in the region marked by A results from a larger sample thickness compared to the darker region B. A 200 keV BF TEM image of the annealed sample is presented in Fig. 4.8d, which was taken at $\Delta f = -12\mu m$. The image shows an unspecific contrast, which is observed in a similar way for an amorphous carbon film at large underfocus values. For amorphous samples with weak density fluctuations, the BF TEM contrast is dominated by the transfer characteristics of the transmission electron microscope. The nanorod-like structures, which are observed in the low-MW P3HT:$PC_{61}BM$ sample (Fig. 4.5d-f), are clearly absent. For comparison of different fabrication processes, the morphology of a solvent-annealed 50 kg/mol sample is shown in Fig. 4.8b. The postprocessing of Fig. 4.8b differs from Fig. 4.8a and c because the HAADF STEM intensities were originally shifted toward higher gray values, which is expected for the larger layer thickness of 126 nm compared to the as-spincast and annealed samples with a thickness of 100 nm. Pronounced intensity variations on a lateral scale of 200 nm

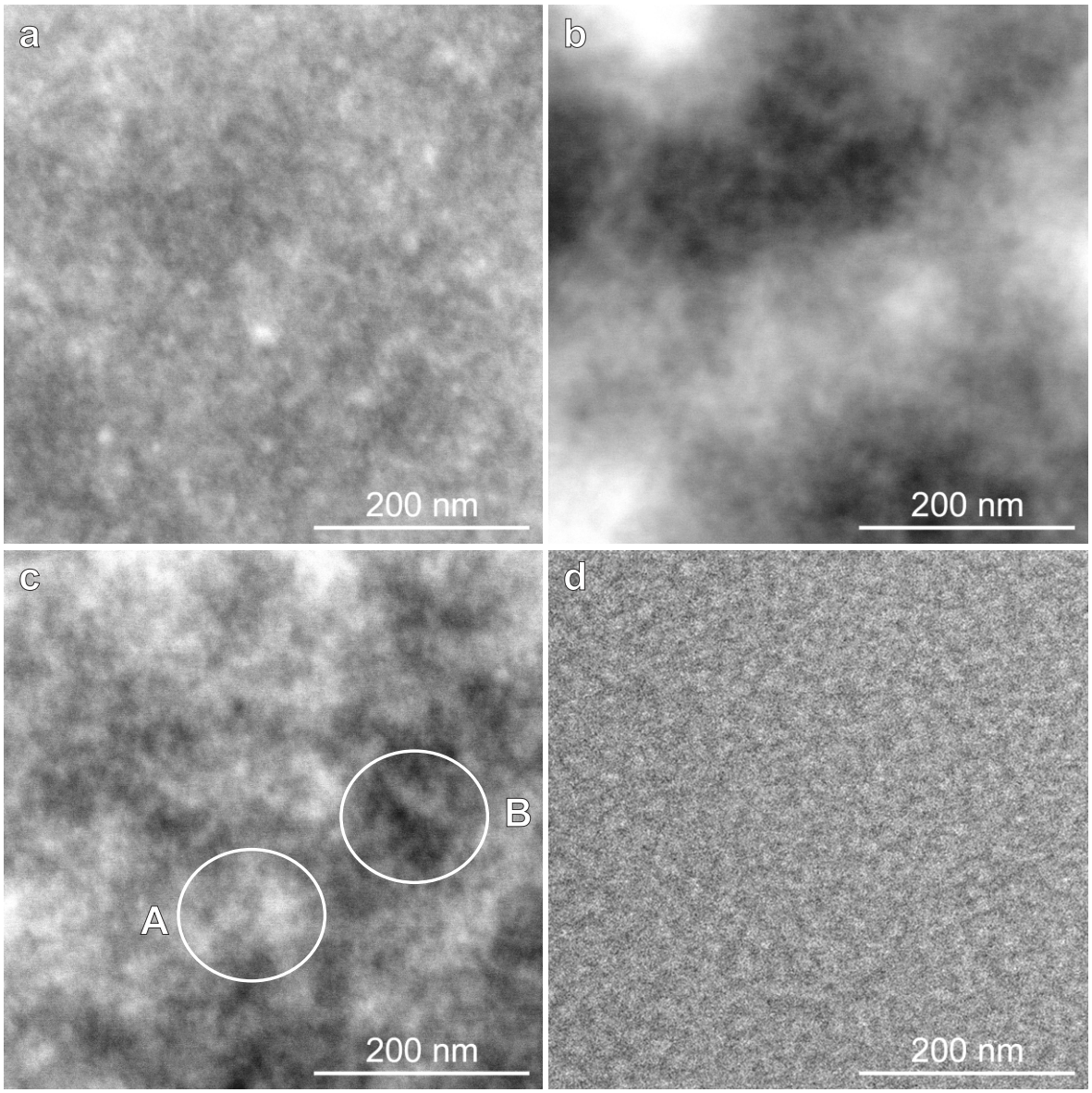

Figure 4.8: 50 kg/mol P3HT:$PC_{61}BM$ samples: HAADF STEM images taken at 15 keV of the a) as-cast sample, b) solvent annealed sample, c) annealed sample (30 min at 150 °C) with regions of larger thickness (marked by A) and smaller thickness (marked by B), and d) TEM image of the annealed sample taken at 200 keV with an underfocus of 12 µm.

can be observed in Fig. 4.8b, which are attributed to considerable fluctuations of the film thickness. As in the as-spincast (Fig. 4.8a) and annealed samples (Fig. 4.8c), a network of globular features with sizes of a few 10 nm is visible. The experiments show that the morphology of the absorber layers strongly depends on the MW of the P3HT (for a mixture of 1:1 P3HT:$PC_{61}BM$). For the low-MW P3HT:$PC_{61}BM$ samples, annealing leads to the formation of P3HT nanorod-like structures that are visible in low-keV HAADF STEM and defocused BF TEM images. In comparison, high-MW P3HT:$PC_{61}BM$ samples are characterized by globular structures with sizes of a few 10 nm, which do not show a pronounced morphological change after annealing at 150 °C for up to 30 min. BF TEM of high-MW P3HT:$PC_{61}BM$ yields images without

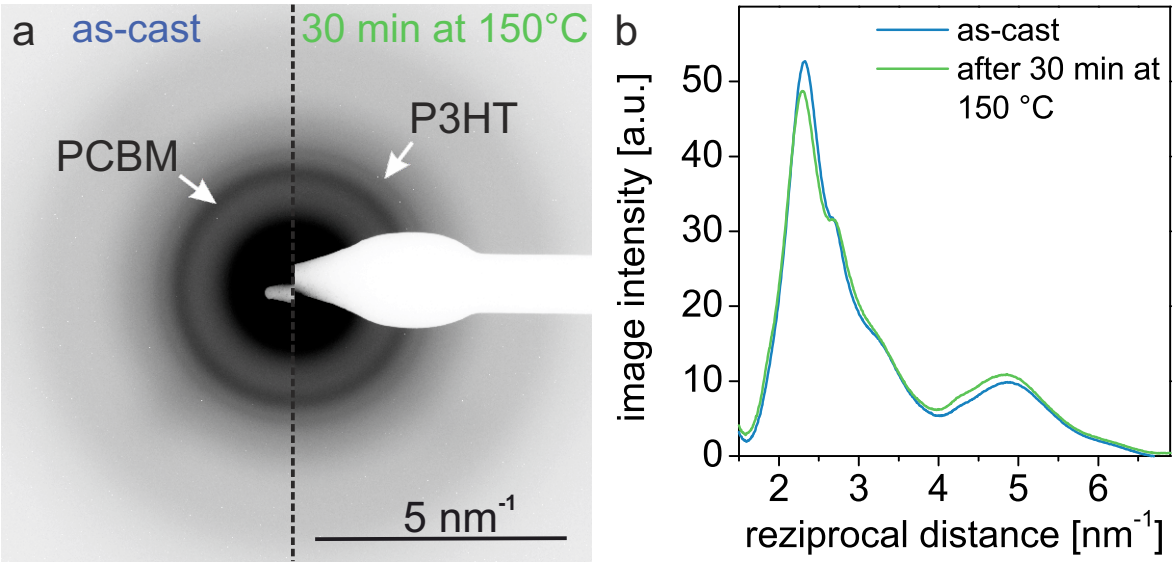

Figure 4.9: a) Contrast-inverted diffraction patterns of the 50 kg/mol P3HT:$PC_{61}BM$ samples before and after annealing for 30 min at 150 °C; b) corresponding radial intensity linescans after background (Lorentz curve) subtraction.

specific contrast, which are dominated by contrast transfer function of the transmission electron microscope. BF TEM fails if the samples contain only features that are small compared to the sample thickness. This results from the strong delocalization of image information at large defocus values and averaging along the electron-beam direction, which makes it impossible to identify distinct features and their sizes. This limitation can be overcome by applying HAADF STEM at low electron energies, which is highly sensitive with respect to small density variations. Furthermore, in-focus imaging avoids delocalization of image contrast and degradation of resolution.

In Fig. 4.9a the diffraction patterns of the as-cast and the annealed samples are displayed. It is obvious that the P3HT reflection at 2.65 nm^{-1} is much weaker for the 50 kg/mol-samples compared to the 20 kg/mol-samples (Fig. 4.6). This is also visible in the radial intensity linescan displayed in Fig. 4.9b. Instead of a peak only a small shoulder appears, indicating a lower degree of crystallinity in the high-MW samples. In addition the intensity of the P3HT π-π stacking peak is not affected by the annealing treatment. This is in accordance with the low-keV HAADF STEM images in Fig. 4.8, which also do not show a pronounced morphological change after annealing.

It is well known from literature that P3HT nanorods appear particularly in samples which contain P3HT with low MW (Chapter 1.4.1 and 1.4.2). Nicolet et al. systematically studied the nanomorphology of P3HT:$PC_{61}BM$ films using P3HT with different M_n between 6.8 and 60 kg/mol [66]. They concluded that a decreasing tendency for the formation of P3HT nanorods exists in samples with increasing MW of P3HT. They explained this behavior of high-MW P3HT molecules by longer, often entangled polymer chains, which impede the diffusion of $PC_{61}BM$ molecules and therefore the formation of large P3HT nanorods and $PC_{61}BM$ agglomerates. As a result, only small P3HT domains are formed even after annealing, which is in agreement with the observations in this work.

5 Nanomorphology of poly(3-hexylselenophene-2,5-diyl)-based organic solar cell absorber layers

In the following chapter the investigation of organic solar cell absorber layers with the conjugated polymer P3HS as donor and the fullerene derivative $PC_{61}BM$ as acceptor material is presented. P3HS is a promising donor material because its absorption covers a large part of the visible spectrum up to 730 nm. It will be shown that annealing of the absorber layers leads to the formation of nanorod-like structures, which are imaged by low-keV HAADF STEM. Comparisons with HAADF STEM intensity calculations, TEM diffraction patterns and the selective dissolution of $PC_{61}BM$ show that the nanorod-like structures consist of P3HS crystals formed by π-π stacking. Furthermore ultramicrotome cross-section samples show an increased P3HS concentration at the anode side of the absorber layer, which is beneficial for the performance of the solar cell device.
Finally the results of the electron microscopic studies are correlated with the optoelectronic device properties.

5.1 Materials and methods

The organic solar cells investigated in this chapter were built by M. Klein and M. Reinhard (LTI, KIT), who also performed the AFM measurements for surface topography measurements. The optoelectronic device properties were characterized by M. Klein and S. Valouch (LTI, KIT).

Solar cell fabrication

All steps of the solar cell fabrication were performed in a clean room. Structured ITO glass slides were cleaned with a cleaning agent, sequentially rinsed with water, acetone, and isopropyl alcohol, and then dried in a nitrogen stream. The substrates were exposed to oxygen plasma for 120 s, transferred to a glovebox and kept under nitrogen atmosphere for the entire deposition process. After spincasting a 45 nm layer of PEDOT:PSS (Clevios^{TM} VPAI4083, Heraeus) from a 2:1 water-diluted solution, residual water was removed by annealing the substrates in a vacuum oven at 120 °C. P3HS (number average molecular weight M_n=53 kg/mol, weight average molecular weight M_w=75 kg/mol, regioregularity RR >95%) and $PC_{61}BM$ were separately dissolved in chlorobenzene (Sigma-Aldrich) with a concentration of 16 mg/ml for the morphology analysis and 12 mg/ml for the TEM/low-keV STEM comparison (Fig. 5.2). As P3HS solutions tend to gel at temperatures below 60 °C [30], it was stirred on a hotplate at 80 °C. After 6 h, the solutions were mixed in a 48:52 (P3HS:$PC_{61}BM$) ratio, stirred for further 16 h and filtered (OmniporeTM, 0.45 µm, Millipore). The heated P3HS:$PC_{61}BM$ solution was spincast atop the PEDOT:PSS layer. During deposition the temperature of both, solution and substrates was varied simultaneously between 70 and 100 °C. Finally, a calcium/aluminum electrode (50/180 nm) was thermally evaporated through a shadow mask in high vacuum ($3 \cdot 10^{-6}$ mbar). The active area of each solar cell was 4 mm^2. Annealing was carried out at 150 °C for 6 min.
For the preparation of ultramicrotome cross-section samples, organic solar cells with PET substrate instead of glass were fabricated. The processing parameters were identical to the ones for the cells on glass substrate. The sample investigated in this study was deposited at 80 °C and subjected to an annealing treatment at 150 °C for 6 min. The ultramicrotome cross-sections were prepared according to the procedure described in detail in Chapter 2.1.2. The thickness of the samples was about 50 nm, estimated on the basis of the adjustment of the ultramicrotome and the color of the sample.
For P3HS density determination five pure P3HS samples with different thicknesses were prepared by varying the concentration from 10 mg/ml to 30 mg/ml. The thickness of the films was determined by FIB cross-sections according to the procedure described in Chapter 2.1.3. The measured thicknesses ranged from 31 to 180 nm.

Solar cell characterization

A spectrally monitored Oriel 300 W solar simulator was used to simulate sunlight at 0.92 suns according to the ASTM-G173-03e1 standard for hemispherical solar irradiance [168]. The current density-voltage (J-V) characteristics of the solar cells were recorded with a Keithley 238 source measure unit. After determining the electrical properties, the devices were thermally annealed on a digitally controlled hotplate at 150 °C for 6 min and measured the J-V-characteristics again.

The AFM measurements were performed with an Anfatec Level AFM. The images were recorded in non-contact mode with a line speed of 0.5 lines per second.

Electron microscopical techniques

After performing the electrical and optical characterization, the active layers of the solar cells were peeled-off from the substrate according to the procedure described in Chapter 2.1.1 and analyzed by low-keV HAADF STEM and TEM. Low-keV STEM was performed in an FEI Strata 400S dual-beam microscope. The general setup and the used STEM II detector is described in Chapter 2.3. The images presented in this chapter were taken with WD=5 mm, collecting electrons from a scattering angle interval between 0.2 and 0.7 rad. All images in this study were taken with a primary electron energy of 15 keV, a beam current of 0.58 nA and a frame time of 35.4 s. The contrast and brightness settings of the amplifier were adjusted to obtain comparable conditions for all images.
The TEM images were taken with an electron energy of 200 keV in a Philips CM200 FEG/ST transmission electron microscope.

5.2 Electron microscopical investigations

5.2.1 Determination of P3HS density

The density of P3HS was determined according to the procedure described in detail in Chapter 3.4.2. The contrast inversion energy was determined for five pure P3HS samples with different thicknesses. The results are presented in Fig. 5.1. The error bars represent the deviation of the thickness measurements at different places, i.e., the thickness variation within the film and the error for the contrast inversion energy determination. A power-law function of the form $y = a \cdot x^2$ is fitted to the measured values, with $a = (1.30 \pm 0.07) \cdot 10^{-6}$. Using Eq. 3.17 the density can be calculated, giving $\rho = 1061 \pm 81$ kg/m^3. This value is similar to the density of P3HT, which was expected because the molecules differ in only one atom.

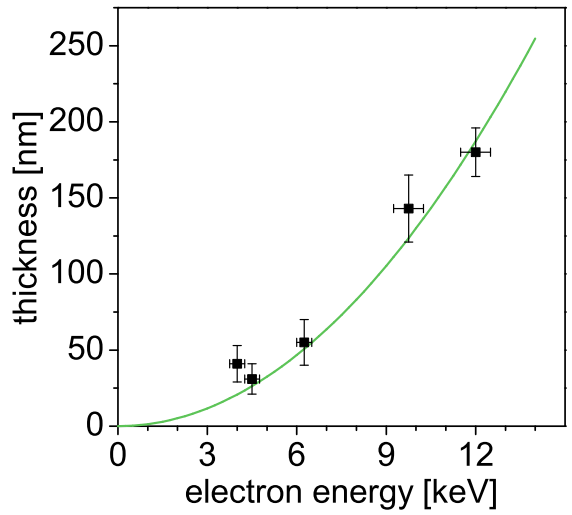

Figure 5.1: Correlation between sample thickness and electron energy at the contrast inversion point for P3HS. The green curve is a fitted power-law function of the form $y = a \cdot x^2$.

5.2.2 Comparison of low-keV STEM and TEM

To illustrate the potential of low-keV STEM for imaging P3HS:$PC_{61}BM$ blends, it is compared with conventional BF TEM at 200 keV. In Fig. 5.2a a 15 keV HAADF STEM image of a P3HS:$PC_{61}BM$ sample is shown. Fig. 5.2b and c show TEM images taken under focused conditions and with a defocus $\Delta f = -10.8$ µm, respectively. The sample with a thickness of about 100 nm was subjected to an annealing treatment at 150 °C for 6 min to induce phase separation of $PC_{61}BM$ and P3HS. Globular structural features with bright contrast are clearly visible in the HAADF STEM image Fig.5.2a. To assign these features to P3HT or $PC_{61}BM$, intensity calculations (described in Chapter 3.4.2) are required. The calculated normalized intensity is plotted in Fig. 5.3 as a function of the electron energy for P3HS and $PC_{61}BM$. For the used electron energy of 15 keV (dashed line) P3HS appears brighter than $PC_{61}BM$. It is to be noted that the contrast between P3HS and $PC_{61}BM$ is much stronger than between P3HT and $PC_{61}BM$ (Chapter 4.2). This is due to the selenium atom in P3HS which increases the mean atomic number Z_m to 7.82 and the mean atomic mass number A_m to 8.53. As described in Chapter 4.2 (in the context of the investigation of P3HT:$PC_{61}BM$ blends), the HAADF STEM intensity does not only depend on the chemical composition but also on the local sample thickness. This requires an analysis of possible

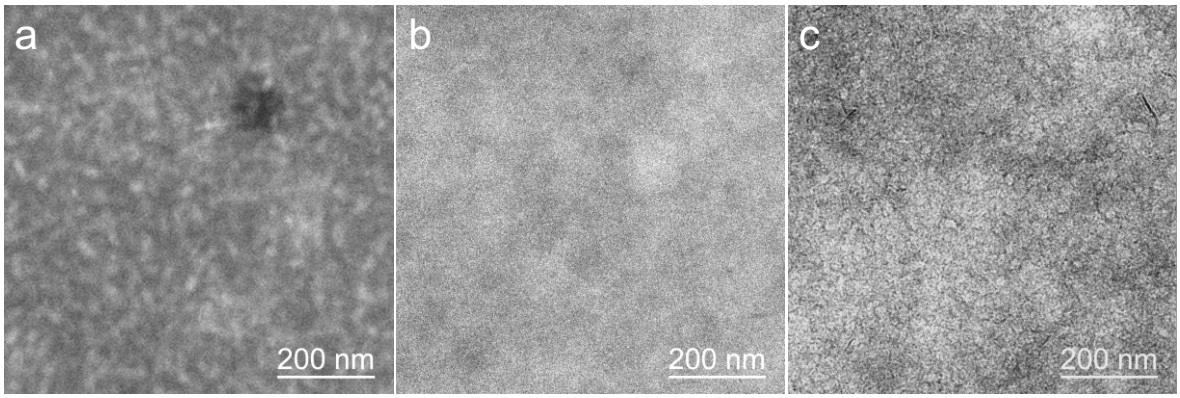

Figure 5.2: a) 15 keV HAADF STEM image of a P3HS:$PC_{61}BM$ sample after annealing for 6 min at 150 °C in comparison to b) an in-focus BF TEM image taken at 200 keV and c) a BF TEM image taken at 200 keV with a defocus of -10.8 µm (different sample position).

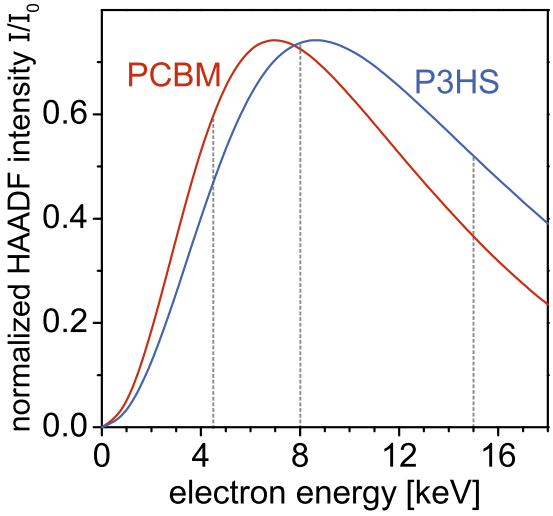

Figure 5.3:
Calculated HAADF STEM intensity for P3HS and $PC_{61}BM$ films with 100 nm thickness. The dashed lines mark the electron energies of 4.5, 8 and 15 keV, in context with the images shown in Fig. 5.5.

sample thickness changes which need to be distinguished from compositional variations. It will be shown in the next section that the bright regions are indeed not induced by small-scale local thickness fluctuations by comparison with AFM images. Regions with reduced STEM intensity and a size of about 100 nm correspond, however, to depressions in the absorber layer. An example for such a depression can be seen in the upper right corner of Fig. 5.2a. For confirmation an SE image of the sample is presented in Fig. 5.4, which shows several depressions in the surface of the film. The cause of these features is probably the formation of pores by evaporating solvent during the drying process.

The BF TEM image in Fig. 5.2b taken close to Gaussian focus shows only coarse contrast fluctuations, which can be attributed to thickness variations of the absorber layer. The bright small-scale features of the HAADF STEM image cannot be seen in Fig. 5.2b due to the small density and atomic number difference between $PC_{61}BM$ and P3HS. The BF TEM image in Fig. 5.2c was taken under defocused conditions, which induces a phase shift between the unscattered and scattered electrons to achieve phase contrast. Here, small-scale features can be observed with similar size as the bright contrast features of the HAADF STEM image. However, the resolution is strongly degraded in conventional TEM imaging due to the delocalization of image information

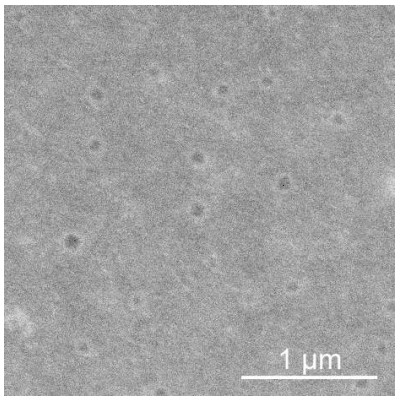

Figure 5.4: SE image taken at 2 keV of the annealed P3HS:$PC_{61}BM$ sample, showing depressions in the surface of the film.

at the required high defocus values and accurate size determination of the structural features is not possible anymore. Moreover, the 3D distribution of P3HS regions leads to a superposition of the weak P3HS contrast features along the electron-beam path through the sample. This prevents clear distinction of the P3HS domains in the 2D projection of the TEM image under the chosen strongly defocused conditions. This fact was already noted by van Bavel et al. [140], who stated that BF TEM imaging only yields sufficient contrast if 50 nm thin layers are studied, which might not necessarily reflect the morphology of real layers - even if they are fabricated under the same conditions.

Optimization of HAADF STEM imaging parameters

As shown in the previous section low-keV HAADF STEM yields images with substantially higher contrast than conventional TEM for P3HS:$PC_{61}BM$ samples. However, the imaging parameters have to be carefully selected. As discussed in Chapter 3 the HAADF STEM intensity exhibits a maximum that depends on the electron energy, the thickness and the composition of the sample. In Fig. 5.3 the intensity is plotted over the electron energy for P3HS and $PC_{61}BM$ for a sample thickness of 100 nm. Since the maxima of the two materials lie at different energies a crossing of the two curves occurs at about 8 keV. For this electron energy no contrast between P3HS and $PC_{61}BM$ can be observed. In Fig. 5.5 three HAADF STEM images of a 100 nm thin sample taken at different electron energies are displayed. In the image taken at 8 keV (Fig. 5.5b) no material contrast is visible. The very faint structures can be attributed to thickness

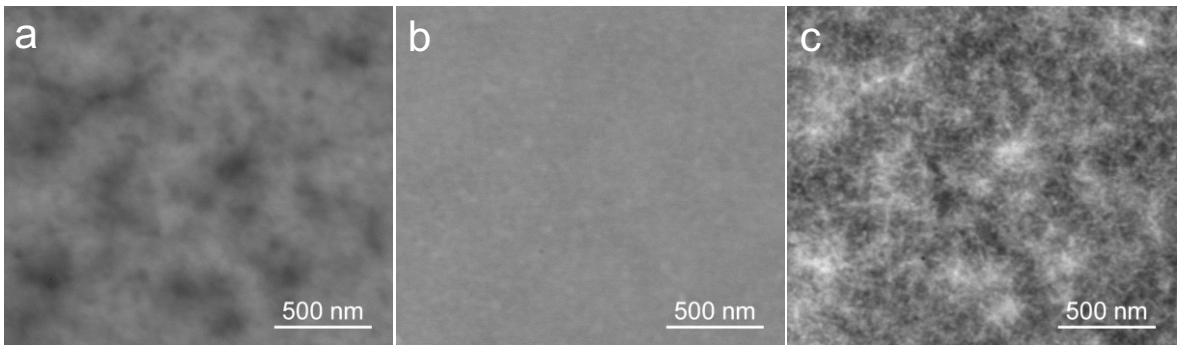

Figure 5.5: HAADF STEM images of a P3HS:$PC_{61}BM$ sample with a thickness of 100 nm after annealing at different electron energies: a) 4.5 keV, b) 8 keV and c) 15 keV.

variations. Fig. 5.5a and c are taken at 4.5 and 15 keV, respectively. A clear contrast inversion, as predicted by the intensity calculations is visible. The contrast between P3HS and PC_{61}BM is quite similar in both images. This corresponds to the calculations, in which the distance of the two intensity curves is about the same for 4.5 and 15 keV (see Fig. 5.3). Hence, concerning contrast maximization it does not make a difference if electron energies lower or higher than the contrast inversion energies are chosen. However, the resolution is degraded at 4.5 keV compared to 15 keV. Whereas in Fig. 5.5c bright needle-like features are clearly resolved, they cannot be recognized in Fig. 5.5c. The thickness dependence of the intensity (discussed in detail in connection with P3HT:PC_{61}BM blends in Chapter 4.2) is also lower for higher electron energies, even though this aspect is not very important for P3HS:PC_{61}BM since thickness variations are usually less pronounced compared to the high material contrast. Considering all these points an electron energy of 15 keV was chosen for the detailed P3HS:PC_{61}BM nanomorphology investigations, presented in the next section.

5.2.3 Nanomorphology of P3HS:PCBM bulk heterojunctions with different processing parameters

As thermal treatment is well known to influence the nanomorphology of BHJs, the solution and the substrate were heated to temperatures between 70 and 100 °C before the deposition of the active layer. The low-keV HAADF STEM images of the different samples before and after annealing for 6 min at 150 °C are displayed in Fig. 5.6. The non-annealed samples deposited at 70 and 90 °C do not show any distinct features. The weak contrast, which is visible in the images is due to thickness variations of the films or contamination caused by the electron beam (bright spots). After thermal treatment, however, the film morphology changes significantly by the formation of needle-like structures, exhibiting a high contrast as shown in Fig. 5.6b and d. The width of the needle-like structures is about 15 nm, whereas the typical length ranges between 50 and 100 nm. If the deposition temperature is further increased to 100 °C, the non-annealed layer in Fig. 5.6e shows some weak whisker-like features without any thermal post-treatment. The inset of the figure shows an enlarged and contrast-enhanced section of the image. After thermal treatment (Fig. 5.6f) the whisker density and the characteristic shape of the whiskers is comparable to those that are visible in the samples deposited at 70 and 90 °C after annealing. Further increasing the deposition temperature leads to a highly inhomogeneous film quality (not shown). Since the samples processed at 70 °C qualitatively show the same behavior as those processed at 90 °C the focus will be on the deposition temperatures T=90 °C and T=100 °C in the following.

As the needle-like structures (STEM intensity changes) could originate from either local sample thickness variations or material domains with different density and atomic number within the bulk, AFM investigations of the sample surfaces were performed. Fig. 5.7 shows as an example an AFM topography image of the annealed active layer deposited at 90 °C. The sample surface exhibits height (thickness) variations in the range of 5 nm. Occasionally very faint elongated features are visible (marked with arrows) that could be correlated with the needle-like structures in the low-keV HAADF STEM images in Fig. 5.6. However, these few features cannot be the main cause of the strong contrast of the needle-like structures in the HAADF STEM images. AFM images of annealed P3HS:PC_{61}BM samples recorded by Ballantyne et al. also do not show

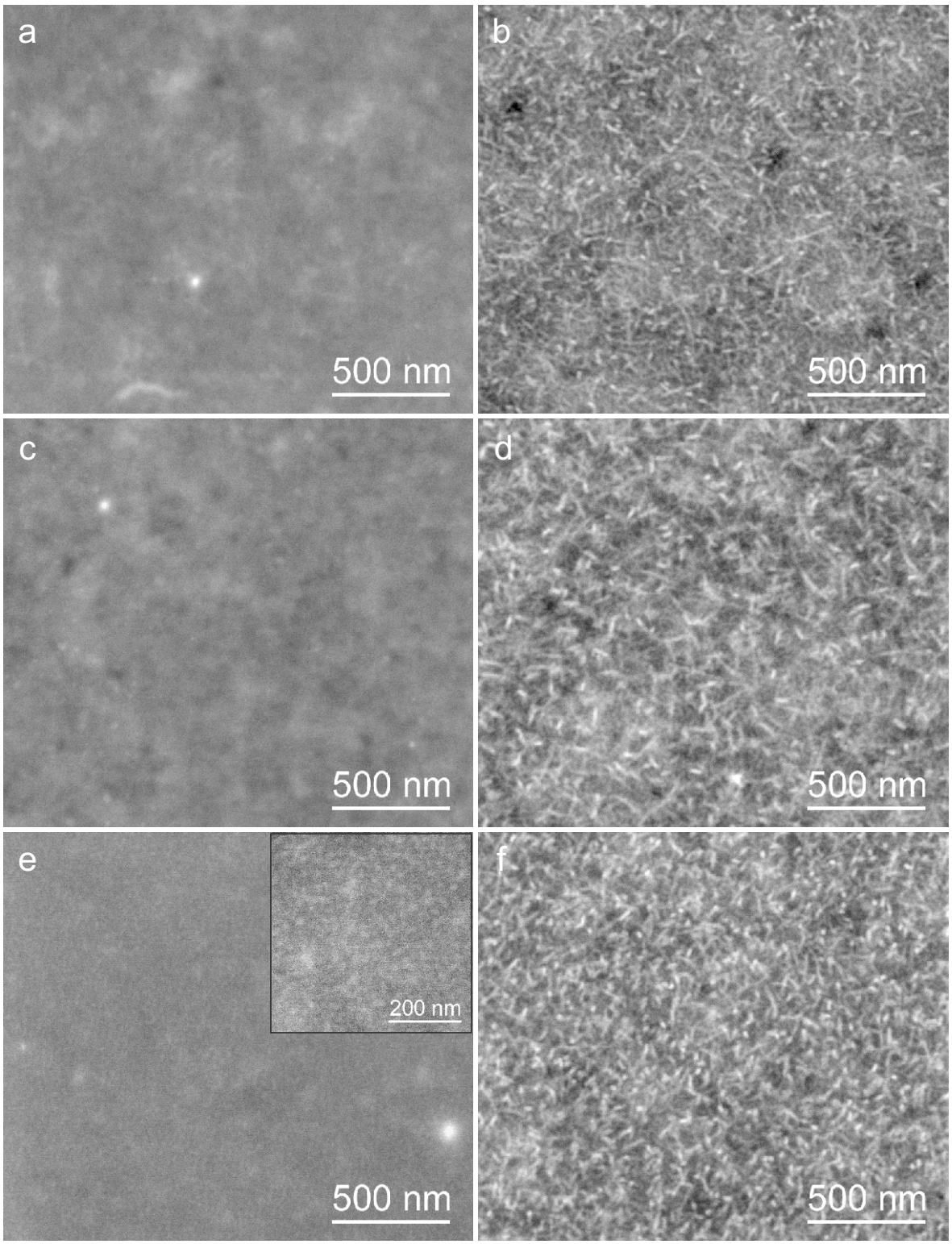

Figure 5.6: 15 keV HAADF STEM images of P3HS:PC_{61}BM films before (left column) and after annealing for 6 min at 150 °C (right column) with different deposition temperatures: a-b) 70 °C, c-d) 90 °C, e-f) 100 °C. The inset of e) shows an contrast enhanced image with a higher magnification.

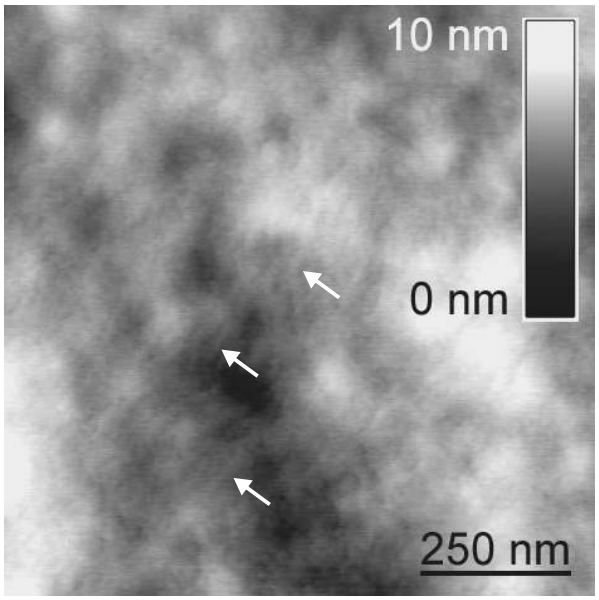

Figure 5.7: AFM topography image of the annealed P3HS:$PC_{61}BM$ sample deposited at 90 °C. Faint elongated features are marked with arrows.

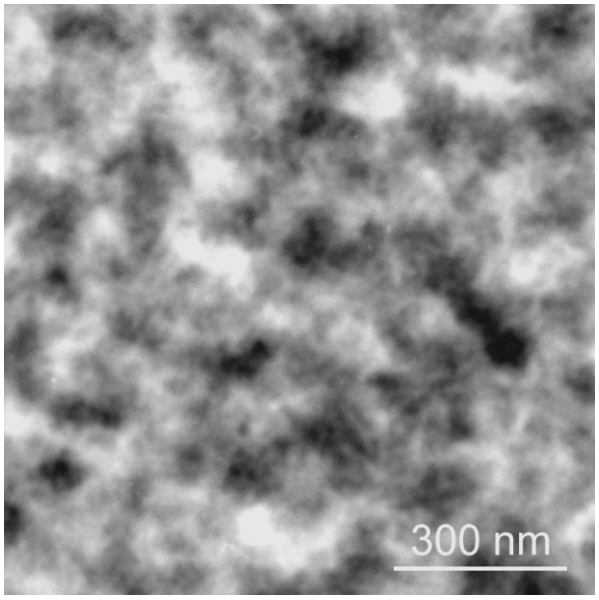

Figure 5.8: HAADF STEM image taken at 15 keV of the annealed P3HS:$PC_{61}BM$ sample rinsed with 1,8-octanedithiol (ODT).

protruding features [30]. Therefore, it can be concluded that the needle-like structures observed in the low-keV HAADF STEM images are mainly located in the bulk and not on the surface. Hence, the high image intensity of the needles in the electron micrographs can indeed be correlated with a local increase of the atomic number and density. According to the HAADF STEM intensity calculations in Chapter 5.2.2, P3HS appears brighter than $PC_{61}BM$ at an electron energy of 15 keV and a sample thickness of about 170 nm. Therefore it can be concluded that the needle-like structures consist of P3HS. This is further suggested by the molecular affinity of P3HS to P3HT, for which the formation of needle-like structures has been shown in Chapter 4. Furthermore Ballantyne et al. [30, 75] attribute P3HS a high tendency to self-organize.

To further substantiate that the needle-like structures consist of P3HS, the thermally annealed sample, deposited at 100 °C was rinsed with ODT, which selectively dissolves $PC_{61}BM$ [62]. After a rinsing time of 10 s, the remaining ODT was removed in a nitrogen gas stream. Fig. 5.8 shows a HAADF STEM image of the rinsed sample. Although the whiskers are notably superimposed by thickness variations from material

agglomeration and suffer from missing material contrast due to the absence of $PC_{61}BM$, the needle-like domain structures are still apparent.
To analyze the structure of the P3HS needles, TEM diffraction patterns were recorded. In Fig. 5.9 a diffraction pattern of the annealed sample deposited at 90 °C is displayed. Two reflection rings are visible: a broad one at 2.28 nm^{-1} and a sharper one at 2.71 nm^{-1}. The inner ring is caused by $PC_{61}BM$ (see Chapter 4.3). Hence, the outer ring can be assigned to P3HS. The reciprocal distance of the ring corresponds to a real-space distance of 0.37 nm, which is very similar to the π-π stacking distance of P3HT (0.38 nm). It can be concluded that the needle-like structures are formed by π-π stacking of the P3HS molecules and the subsequent formation of elongated crystallites.

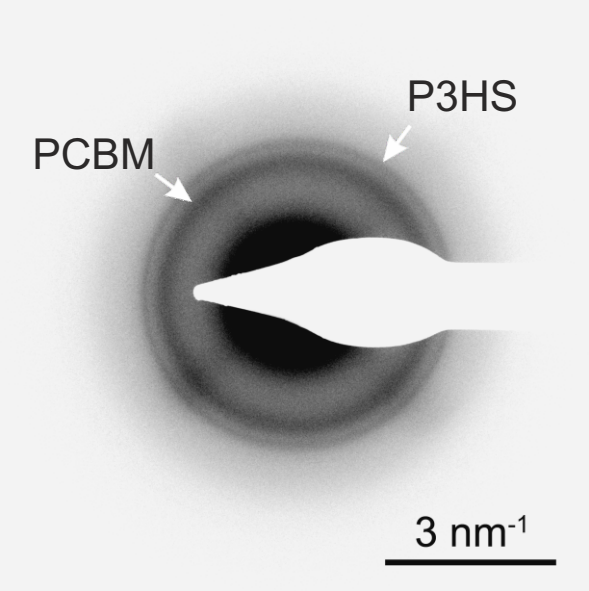

Figure 5.9: Contrast-inverted TEM diffraction pattern of the annealed P3HS:$PC_{61}BM$ sample deposited at 90 °C.

5.2.4 Vertical distribution of donor and acceptor phase

To analyze the distribution of P3HS and $PC_{61}BM$ in vertical direction, cross-section samples prepared by ultramicrotomy were investigated. In Fig. 5.10 an HAADF STEM image of the annealed sample deposited at 80 °C is presented. The epoxy resin in which the sample was embedded is visible on the left side of the film. Since the PEDOT:PSS layer was dissolved during the sample preparation process, the PEDOT:PSS and the ITO layer underneath are not visible on the right side. Like in the plan-view samples presented in the previous section, bright needle-like structures are visible in the absorber layer. The width of the needles of about 15 nm corresponds to the size measured in the plan-view samples. A slight increase of the P3HS concentration occurs at the bottom side of the absorber layer, recognizable by the higher intensity. For the standard design of organic solar cells, described in Chapter 1.3, this higher concentration of donor material at the anode side is favorable, because it decreases the probability for short circuits in the absorber layer and enhances the transport of the charge carriers to the respective electrode.

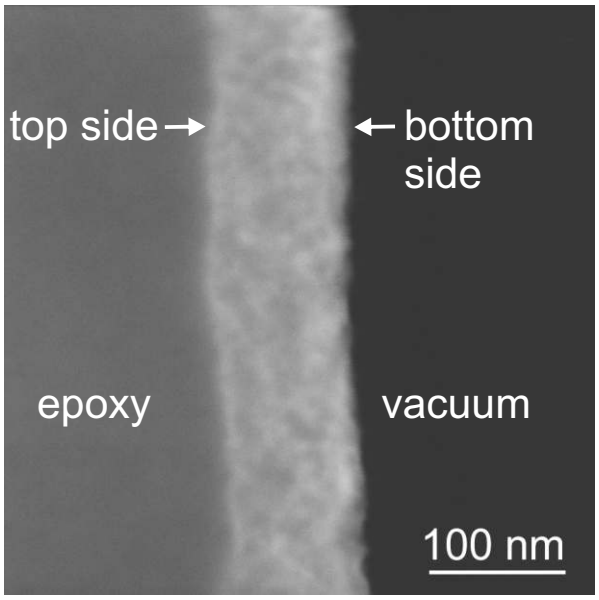

Figure 5.10: 15 keV HAADF STEM image of an ultramicrotome cross-section of the annealed P3HS:$PC_{61}BM$ absorber layer deposited at 80 °C.

5.3 Correlation with optoelectronic properties

The observations of changes in the P3HS:$PC_{61}BM$ nanomorphology in conjunction with the formation of P3HS needle-like structures have considerable impact on the optoelectronic properties of the respective photovoltaic devices.
In Table 5.1 the key parameters of the solar cells are summarized. An enhancement of the optoelectronic properties can be observed after annealing. The current-voltage characteristics and key parameters of the as-cast P3HS:$PC_{61}BM$ solar cells show only a slight variation with respect to the deposition temperature T. The open-circuit voltage of all devices was in the order of V_{OC}=0.7 V, the power conversion efficiency η=0.3% and the device short-circuit current density J_{SC}=1.1 mA/cm^2 for all non-annealed devices. After measuring the cell performance of the solar cells as deposited, they were thermally annealed and subsequently characterized again. In Fig. 5.11 the J-V curves before and after annealing are plotted. Although V_{OC} is reduced, J_{SC} and FF simultaneously improved significantly and consequently led to an increase in power conversion efficiency up to η=1.4%.
As already mentioned in Chapter 1.4.2 higher efficiencies on devices comprising P3HS have been reported before [30, 75]. However, it has to be considered that the molecular weight of the P3HS used in these studies was higher than the one of the P3HS employed in our current investigations.
The decline of V_{OC} to 0.5 V after a thermal post-treatment is likely to be caused by

	as-cast				annealed			
T_{Dep}	70 °C	80 °C	90 °C	100 °C	70 °C	80 °C	90 °C	100 °C
V_{OC} [V]	0.68	0.74	0.71	0.67	0.52	0.52	0.51	0.51
J_{SC} [mA/cm^2]	1.3	1.2	1.0	1.2	4.3	3.9	4.7	4.5
FF [%]	35	34	33	33	54	50	60	59
η [%]	0.3	0.3	0.2	0.3	1.2	1.0	1.4	1.4

Table 5.1: Solar cell key parameters of the as-cast and the annealed P3HS:$PC_{61}BM$ samples with different deposition temperatures T_{Dep}.

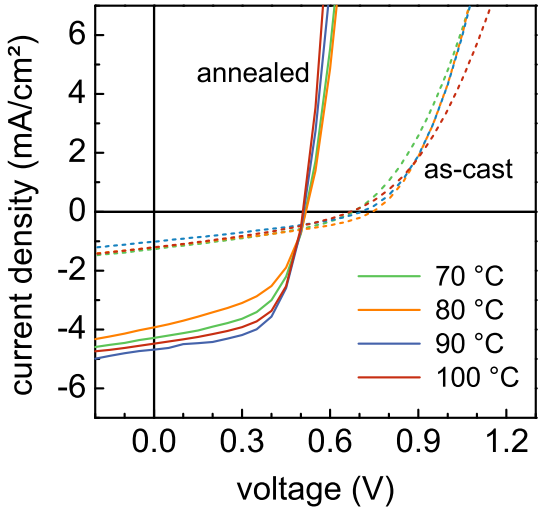

Figure 5.11: Current-voltage characteristics of the as-cast (dashed lines) and annealed (solid lines) P3HS:$PC_{61}BM$ solar cells under illumination at 92 mW/cm^2. The different colors denote the deposition temperatures of the samples.

an up-shift of the polymer's HOMO level as it has been observed for P3HT after thermal annealing earlier [169]. The equalization of the V_{OC} of devices with different deposition temperatures on annealing can be attributed to a matching of the active layer nanomorphologies as discussed in Chapter 5.2.3.
Absorption measurements show a change in the absorption spectra due to thermal annealing [170]. The maximum of the P3HS π-π^*-absorption peak is shifted to higher wavelengths and an additional shoulder appears at 680 nm. These changes are also observed for the related polymer P3HT, for which the increased interaction between the P3HT chains after annealing leads to an increased delocalization of the π electrons, and therefore a lowering of the transition energy between π and π^*.
Besides an improved photon harvesting through a broader absorption after annealing, the significant increase of the device short-circuit current density can be attributed to the formation of distinct molecule domains. The formation of needle-like P3HS crystals with a width in the order of the exciton diffusion length allows for efficient exciton dissociation. At the same time, charge carriers can be extracted more efficiently along the P3HS needles and the intermediate $PC_{61}BM$ domains. This is further positively influenced by the increased P3HS concentration at the anode side of the active layer.
Because of the formation of needle-like polymer structures a higher hole mobility can also be expected [141]. To qualitatively compare the charge carrier mobility within the active layer before and after thermal annealing, time-resolved photoresponse measurements were performed [170]. The time-dependent photo response after laser excitation shows a faster decline in current density of the annealed devices compared to pristine devices. This faster decay in current density can be directly attributed to a higher charge carrier mobility and thus a more efficient charge carrier extraction from the device leading to an enhanced current density [171].

6 Nanomorphology of organic solar cell absorber layers based on carbazole-phenylbenzotriazole copolymers

In the following chapter nanomorphology investigations of poly[*N*-9'-heptadecanyl-2,7-carbazole-*alt*-5,5-(4',7'-di-2-thienyl-2'-(3,5-difluoro-4-octyldodecyloxyphenyl)- 2'*H*-benzotriazole)] (PCDTPBt) based absorber layers are presented. Since the polymer was synthesized for the first time, the best processing parameters and an appropriate acceptor material had to be found. For this purpose different sets of organic solar cells were fabricated and characterized. Low-keV STEM investigations, which revealed the nanomorphology of the absorber layers, contributed to further enhancement of the solar cell performance.
In the course of this study the polymer was first blended with $PC_{61}BM$ and later with $PC_{71}BM$ which yields a higher efficiency due to the improved absorption of light. Furthermore it was shown that an inverted device architecture exceeds the standard design. The highest increase of the power conversion efficiency could be achieved by adding the processing additives ODT and DIO to the host solvent DCB. In this way the power conversion efficiency could be increased to 4.6% for the absorber layers with DIO as additive. These samples exhibit a finer bulk morphology of the active layer than the samples deposited only from DCB. By the comparison of the results of electron diffraction studies and GIXD measurements, it could be shown that the samples with DIO as additive exhibit a preferential face-on configuration of the PCDTPBt polymer chains which is beneficial for the vertical hole transport in the absorber layer.

6.1 Materials and methods

The copolymer PCDTPBt was synthesized by F. M. Pasker (Kekulé-Institute für Organische Chemie und Biochemie, Rheinische Friedrich-Wilhelms-Universität Bonn) while the solar cell samples were fabricated and characterized by M. Klein, D. Landerer and M. Isen (LTI, KIT) [33, 172, 173]. GIXD measurements were carried out by S. Kowarik (Institute for Physics, Humboldt University Berlin) [33].

Fabrication of solar cell devices

Organic solar cells were fabricated with a standard and an inverted architecture. For both designs ITO covered glass slides were cleaned with acetone and isopropyl alcohol and then dried in a nitrogen stream. For the standard design devices a PEDOT:PSS (Baytron AI 4083, HC Starck) layer was spincast from a 1:1 water diluted solution. Residual water was removed by annealing the substrates for 30 min in a vacuum oven at 120 °C. PCDTPBt and $PC_{61}BM$ (99.5 %, Solenne BV) or $PC_{71}BM$ (99 %, Solenne BV) were dissolved in the desired mixing ratio in DCB (anhydrous, 99 %, Sigma-Aldrich). The solution was then heated to 80 °C and subsequently spincast on top of the PEDOT:PSS layer in a nitrogen atmosphere. Finally, a calcium/aluminum electrode (20/150 nm) was thermally evaporated through a shadow mask in high vacuum.
For the inverted solar cells sol-gel ZnO was prepared according to the process described by Subbiah et al. [52]. The sol-gel ZnO was spin coated on top of the ITO glass substrate and annealed at 200 °C for 30 min. Then the substrates were swayed in acetone, rinsed with water and dried with nitrogen. The active layer was prepared like for the standard design devices.
For the samples with additives (standard and inverted design), 5 vol % ODT or 3 vol % DIO was mixed with the host solvent DCB. For all samples a MoO_3/Ag (7 nm/80 nm) electrode was vacuum deposited through a shadow mask.
Since thermal treatment of the solar cells did not show an enhanced efficiency [172], only non-annealed samples are presented in this chapter.

Preparation of electron microscopy samples

To investigate the active layers by electron microscopy it has to be detached according to the sample preparation procedure described in detail in Chapter 2.1.1. For this procedure a PEDOT:PSS layer is needed underneath the active layer. Hence the solar cells with an inverted device architecture could not be examined and additional samples with a standard device architecture but the same processing parameters had to be prepared.

Electron microscopical techniques

Low-keV HAADF STEM images were performed in the FEI Strata 400S dual-beam microscope with the STEM II detector described in Chapter 2.3. Due to the different thicknesses of the samples the contrast and brightness settings had to be adjusted for every sample. The contrast in the different images is therefore not quantitatively comparable.

6.2 Electron microscopical investigations

6.2.1 Morphology of absorber layers without additives

The influence of the PCDTPBt:$PC_{61}BM$ mixing ration on the solar cell efficiency was first studied. Experiments of M. Isen showed that solar cells with a higher $PC_{61}BM$ content show a better efficiency [172]. The highest efficiency of 1.1 % was measured for the device with a 1:4 mixing ratio. A mixing ratio of 1:2 yielded only a slighly smaller efficiency of 1.0 %, whereas for samples with a $PC_{61}BM$ content less than or equal to 50 % the efficiency was decreased below 0.5 %.
In Fig. 6.1 low-keV HAADF STEM images of samples with mixing ratios of 1:2 and 1:4 are presented. In the sample with a mixing ratio of 1:2 (Fig. 6.1a) large bright domains in the range of a few 100 nm and elongated dark structures with a width of about 50 nm and a length of several 100 nm are visible. In the sample with a mixing ratio of 1:4 (Fig. 6.1b) the number and the size of the dark phase is decreased, but gray elongated structures, with a similar shape like the dark ones in Fig.6.1a are visible. In both samples small bright spots with a size of about 10 nm are present.
For the interpretation of the images it is advisable to calculate the HAADF STEM image intensity according to the procedure described in Chapter 3.4.2. Unfortunately this was not possible due to the unknown density of PCDTPBt. Furthermore there was not enough PCDTPBt available to prepare pure films with different thicknesses, which are needed for the density determination also described in Chapter 3.4.2.
Nevertheless, to interpret the HAADF STEM images, energy dispersive X-ray spectroscopy (EDXS) analyses were carried out. In Fig. 6.2 spectra of a bright and a dark domain are presented. To record these spectra small rectangular regions were scanned, marked in the HAADF STEM image in Fig.6.2a. It has to be noted that the copper and the aluminum X-ray peaks are caused by the TEM grid and the microscope chamber, respectively. Except for the sulfur K_α-peak at 2.31 keV and the nitrogen K_α-peak at 0.39 keV, the two energy dispersive X-ray (EDX) spectra are similar. Since sulfur and

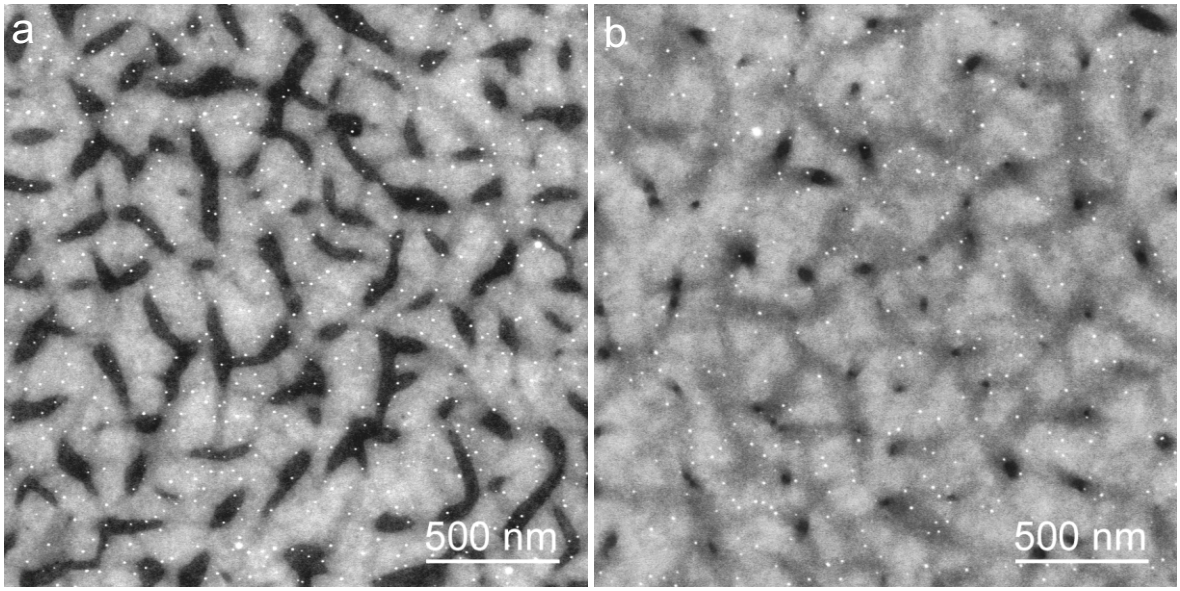

Figure 6.1: 15 keV HAADF STEM images of PCDTPBt:$PC_{61}BM$ with a mixing ratio of a) 1:2 and b) 1:4.

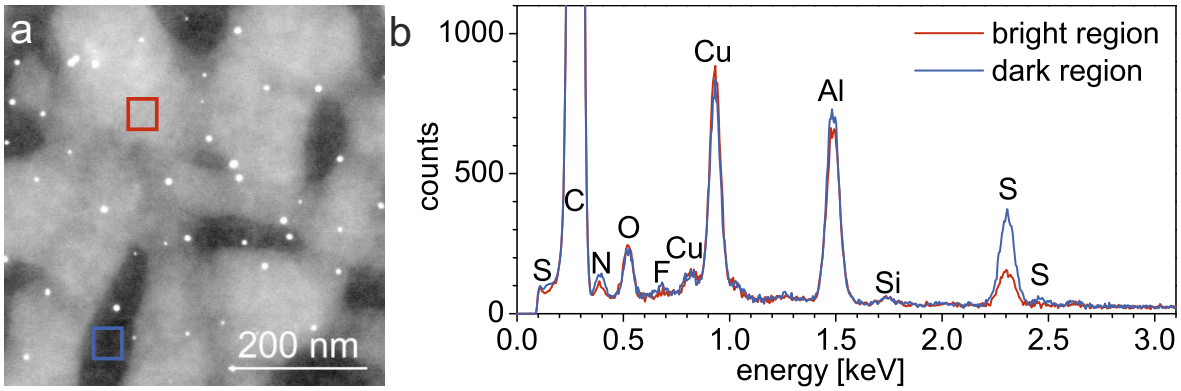

Figure 6.2: a) 15 keV HAADF STEM image of the PCDTPBt:$PC_{61}BM$ sample with a mixing ratio of 1:2; b) EDX spectra of a bright and a dark region of the sample marked in a).

nitrogen are only contained in PCDTPBt and not in $PC_{61}BM$, the higher sulfur and nitrogen signals are an indication of a higher PCDTPBt content. The dark phase can be therefore assigned to a PCDTPBt-rich phase, whereas the bright phase is $PC_{61}BM$-rich. This finding corresponds to the lower fraction of the dark phase in the sample with a mixing ratio of 1:4 (Fig. 6.1b). The gray structures in Fig. 6.1b are either due to thickness variations or due to the superposition of a dark and bright phase along the propagation direction of the electrons.

The composition of the bright nanoparticles visible in both samples, was also analyzed by EDXS. Due to the small size of the particles, the EDX signal is very low. To increase the signal-to-noise ratio and to minimize the contamination of the scanned area, five EDX spectra of areas with a particularly high number of particles were summed up. In Fig. 6.3 the resulting spectra is presented. As a reference, a spectrum from a large sample area with the same acquisition time is displayed. Two additional peaks appear in the nanoparticle spectra, which can be assigned to the palladium L_α-peak at 2.85 keV and the palladium L_β-peak at 3.00 keV. The sulfur K_α-peak is decreased in comparison to the reference spectrum. This can be attributed to the fact that the major fraction of the particles is located in the bright $PC_{61}BM$-rich phase, which contains less sulfur. The EDXS analysis reveals that the particles consist of

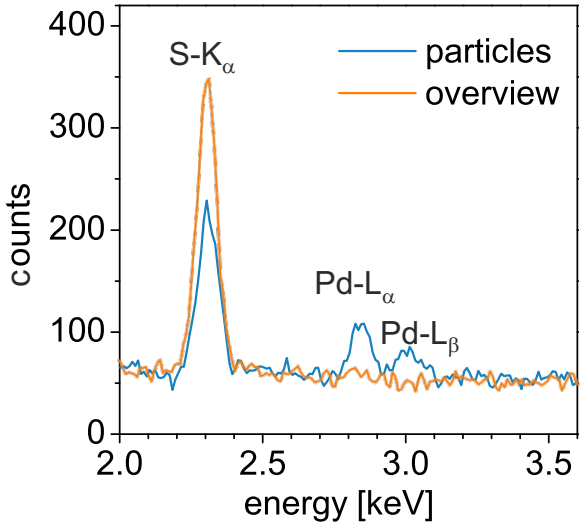

Figure 6.3: EDX spectrum of a large sample area (overview) and accumulated spectra of small areas with a particularly high number of bright particles.

palladium. Hence, the nanoparticles probably originate from the PCDTPBt synthesis, where palladium is used as a catalyst [33].
According to the measurements of M. Isen, the reason for the low efficiency of the solar cells is primarily the small short-circuit current density J_{SC} [172]. It is caused by a low absorption of the photoactive layer (which will be discussed in Section 6.2.3) and possibly by a small exciton-diffusion efficiency η_{ED}. The size of the PCDTPBt-rich domains visible in the HAADF STEM images (Fig. 6.1) is in the range of 50 nm. The typical exciton-diffusion length is 10-15 nm, which is much smaller than the domain size. As a consequence many excitons do not reach the donor/acceptor interface within their lifetime. An improvement of the efficiency can be expected from the reduction of the domain size. This can be realized, for example, by using additives, which will be described in the following section.

6.2.2 Influence of 1,8-octanedithiol as additive on the absorber layer morphology

As described in Chapter 1.4.1, the addition of a small fraction of another solvent to the polymer/fullerene solution can influence the drying-kinetics and therefore the domain sizes. M. Isen showed that samples with the additive ODT are characterized by improved device efficiencies of up to 1.5 %. This was connected with an increase of I_{SC} and FF, while V_{OC} was slightly decreased. The ideal mixing ratio for samples with ODT was found to be 1:2 [172].
In Fig. 6.4 low-keV HAADF STEM images of a reference sample without additive and a mixing ratio of 1:3 and two samples with ODT and mixing ratios of 1:3 and 1:2 are presented. The reference sample (Fig. 6.4a) is similar to the two samples without additives in the previous section. (Fig. 6.1). The fraction of the dark PCDTPBt-rich phase lies as expected between the fraction of the samples with mixing ratio 1:2 and 1:4. The two samples with ODT as additive (Fig. 6.4b and c) exhibit both smaller domain sizes. The width of the elongated dark PCDTPBt-rich structures is about 30 nm for a mixing ratio of 1:3 and 20 nm for a mixing ratio of 1:2, which is almost as small as the exciton-diffusion length. The improvement of the PCE can therefore be

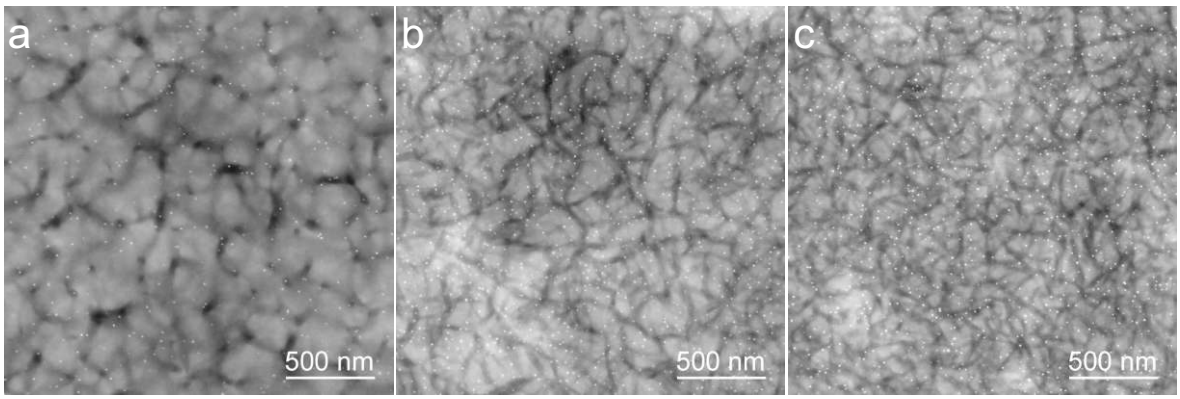

Figure 6.4: 15 keV HAADF STEM images of PCDTPBt:$PC_{61}BM$ samples with a) a mixing ratio of 1:3 and no additive; b) a mixing ratio of 1:3 and ODT as additive and c) a mixing ratio of 1:2 and ODT as additive.

assigned at least partly to the decrease of the domain size. It is also possible that the addition of ODT enhances the purity of the polymer phase and therefore increases I_{SC}.

6.2.3 Morphology of absorber layers with $PC_{71}BM$ as acceptor material

The short-circuit current density cannot only be improved by adjusting the morphology, but also by increasing the absorption of the absorber layer. For that purpose the larger fullerene derivative $PC_{71}BM$ was employed. Compared to $PC_{61}BM$ the absorption spectra is red-shifted and can therefore increase the absorption of the photoactive layer (Chapter 1.2.2). Experiments of M. Isen showed that the usage of $PC_{71}BM$ increased the short-circuit current density by over 60 %, while the open-circuit voltage stayed at a high level.
In Fig. 6.5 a 15 keV HAADF STEM image of a PCDTPBt:$PC_{71}BM$ sample with a mixing ratio of 1:3 is displayed. Compared to the sample with $PC_{61}BM$ and the same mixing ratio in Fig. 6.4a no significant change of the morphology is visible. It has to be noted that the sample thickness of the PCDTPBt:$PC_{71}BM$ is 20 nm larger than the thickness of the PCDTPBt:$PC_{61}BM$ sample. Therefore the two images are not exactly comparable. Nevertheless the increase of the short-circuit current density can be mainly assigned to the higher absorbance of the $PC_{71}BM$ and not to major morphology changes.

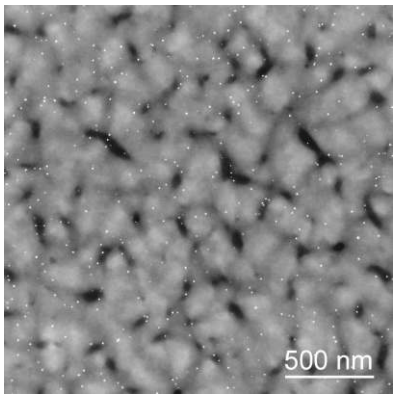

Figure 6.5: HAADF STEM image taken at 15 keV of a PCDTPBt:$PC_{71}BM$ sample with a mixing ratio of 1:3.

6.2.4 Influence of 1,8-diiodooctane as additive on the absorber layer morphology

On the basis of the findings presented in the previous section all following samples were fabricated with the fullerene derivative $PC_{71}BM$ instead of $PC_{61}BM$. Furthermore the experiments of D. Landerer showed that an inverted solar cell device architecture is beneficial for the device performance [173]. To further optimize the nanomorphology and therefore the PCE of the solar cells, the solvent DIO was employed as processing additive [33, 173]. As mentioned in Chapter 1.4.1 DIO is well known to influence the nanomorphology because it exhibits a selective solubility of the fullerene component and has a high boiling point. Experiments with ODT as additive for PCDTPBt:$PC_{71}BM$ blends did not show an enhancement of the efficiency, which was probably due to the appearance of several µm large agglomerations and associated large thickness variations [173].

solvent	J_{SC} [mA/cm^2]	V_{OC} [mV]	FF [%]	PCE [%]
DCB	4.1	840	58	2.5
DCB:DIO	6.4	820	70	4.6

Table 6.1: Solar cell key parameters of the PCDTPBt:$PC_{71}BM$ samples with and without DIO as processing additive [33].

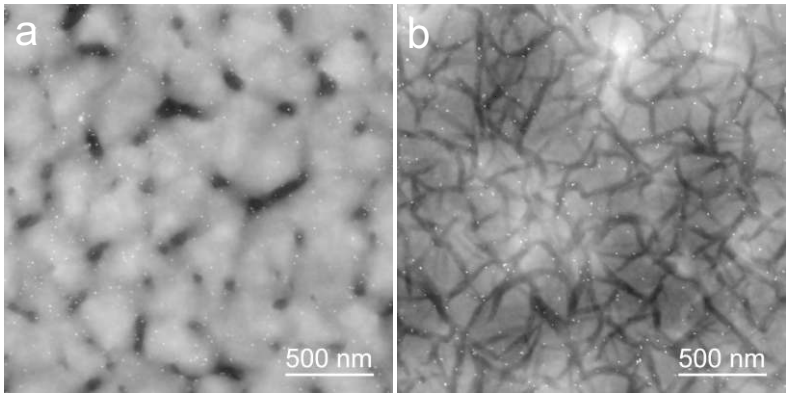

Figure 6.6:
HAADF STEM images taken at E=15 keV of PCDTPBt:$PC_{71}BM$ samples with a) a mixing ratio of 1:3 and no additive; b) a mixing ratio of 1:2 and DIO as processing additive.

To investigate the influence of DIO on the nanomorphology of PCDTPBt:$PC_{71}BM$ solar cells, two devices were built. For the reference sample a mixing ratio of 1:3 and for the sample with DIO a mixing ratio of 1:2 was chosen. In Table 6.1 the solar cell key parameters are summarized.
Adding DIO to the DCB solution increases the PCE by a factor of 1.8 to 4.6 %. The open circuit voltage V_{OC} decreases only marginally, whereas the FF and the short circuit current density J_{SC} are highly improved.
In Fig. 6.6 two 15 keV HAADF STEM images of the sample with and without DIO as procession additive are shown. The domain size is significantly decreased in the sample with DIO leading to ana increased exciton-diffusion efficiency. Furthermore an interconnected network of the dark PCDTPBt-rich phase is visible, which presumably enhances the charge transport to the electrodes. Compared to the PCDTPBt:$PC_{61}BM$ sample with ODT and a mixing ratio of 1:2 (Fig. 6.4) which showed the highest efficiency of the ODT samples, the domain size of the DIO sample is larger. This may indicate that performance of PCDTPBt:$PC_{71}BM$ solar cells could be further enhanced by decreasing the domain size.

6.2.5 Crystalline structure of PCDTPBt

To analyze the crystalline structure of the PCDTPBt-based absorber layers electron diffraction patterns of the PCDTPBt:$PC_{61}BM$ sample with ODT as additive and the PCDTPBt:$PC_{71}BM$ sample with DIO were recorded. Both samples had the same mixing ratio of 1:2.
Fig. 6.7 shows the diffraction pattern of the ODT sample. The four dark spots marked by arrows are imaging artifacts caused by an inaccurate alignment of the microscope. They are only visible due to the low overall image intensity. Since the spots lie in the inner part of the diffraction pattern, which does not contain usable information, they do not hinder the analysis of the crystalline structure. In Fig. 6.7b the radial intensity linescan of the diffraction pattern is shown. The background in form of a Lorentz curve was subtracted from the original data to enhance the visibility of the

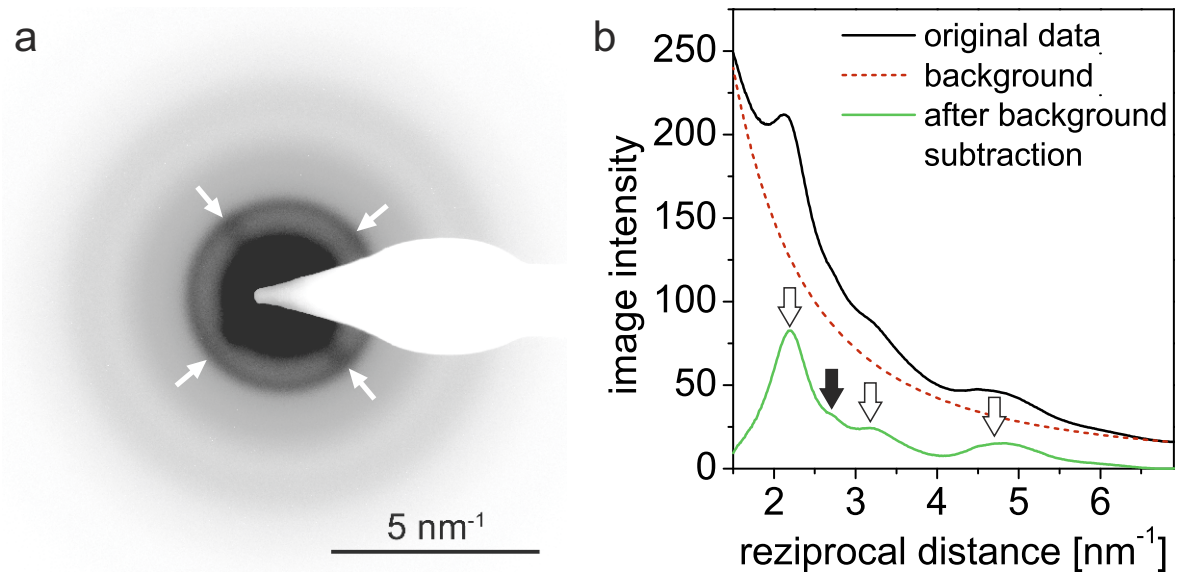

Figure 6.7: a) contrast-inverted TEM diffraction pattern of a PCDTPBt:$PC_{61}BM$ sample with a mixing ratio of 1:2 and ODT as additive. The four dark spots marked by arrows are imaging artifacts caused by an inaccurate alignment of the microscope. b) radial linescan of the diffraction pattern. The background in form of a Lorentz curve is subtracted from the original data. The white arrows mark $PC_{61}BM$ peaks, the black arrow the PCDTPBt peak.

diffraction rings. The peaks at 2.18, 3.25 and 4.70 nm^{-1} (marked by white arrows) can be assigned to $PC_{61}BM$ [72]. The small peak at 2.70 nm^{-1} marked by a black arrow corresponds to a real-space distance of 0.37 nm. This value is in accordance to the π-π stacking distance of PCDTPBt measured by GIXD by Klein et al. [33]. Based on the visibility of the PCDTPBt π-π stacking peak in the diffraction pattern it can be concluded that the sample contains PCDTPBt crystals which are oriented edge-on, which means that π-π stacking occurs parallel to the substrate surface. A scheme of the edge-on arrangement can be found in Fig. 6.8b. GIXD measurements on pure PCDTPBt samples did not indicate any edge-on configuration. The polymer chains are preferentially oriented face-on, which means that π-π stacking occurs perpendicular to the substrate surface (Fig. 6.8a). The difference in the orientation of the PCDTPBt

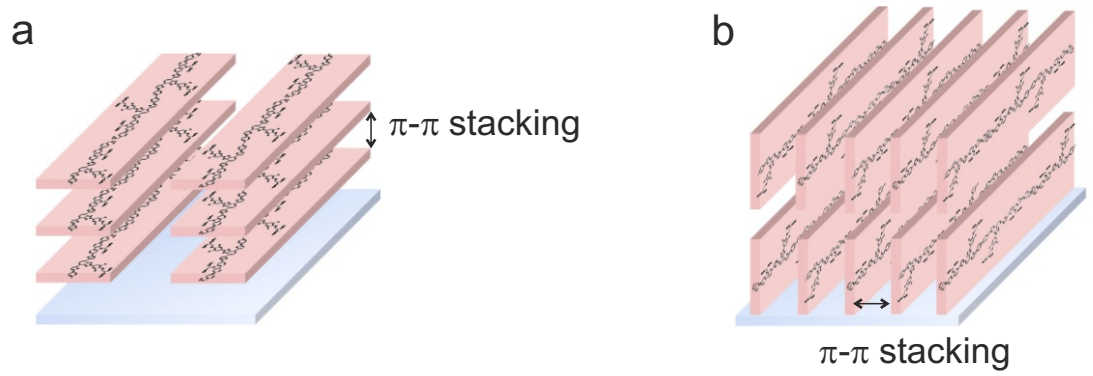

Figure 6.8: Scheme of a) face-on and b) edge-on oriented PCDTPBt polymer chains.

crystals in the PCDTPBt:$PC_{71}BM$ blend compared to the pure PCDTPBt is either caused by the addition of $PC_{71}BM$ to the polymer or by the processing additive ODT. Nevertheless it has to be noted that the overall intensity of the PCDTPBt reflections in the GIXD and SAED measurements iss very low, indicating that the crystalline domains must coexist with significant amounts of amorphous PCDTPBt.
In Fig. 6.9 the radial intensity linescan of the electron diffraction pattern of the PCDTPBt:$PC_{71}BM$ sample with DIO as additive is displayed. Except for the $PC_{71}BM$ peaks (marked by white arrows), no additional peaks are visible. The black arrow marks the expected position of the PCDTPBt π-π stacking peak. The absence of this peak indicates that the PCDTPBt polymer chains are oriented face-on, and are therefore not visible in the diffraction pattern. This is confirmed by GIXD measurements of the DIO sample [33], which also showed a preferential face-on orientation. It has to be noted that in all examined samples the fraction of crystalline PCDTPBt is low and most of the PCDTPBt is in an amorphous state. Nevertheless it can be assumed that the face-on orientation and the subsequent vertical π-π stacking improves the hole transport to the electrode and charge extraction [174]. Besides the higher absorption of $PC_{71}BM$ the preferential face-on configuration could be a reason for the higher efficiency of the solar cells with DIO compared to the cells with ODT as additive.

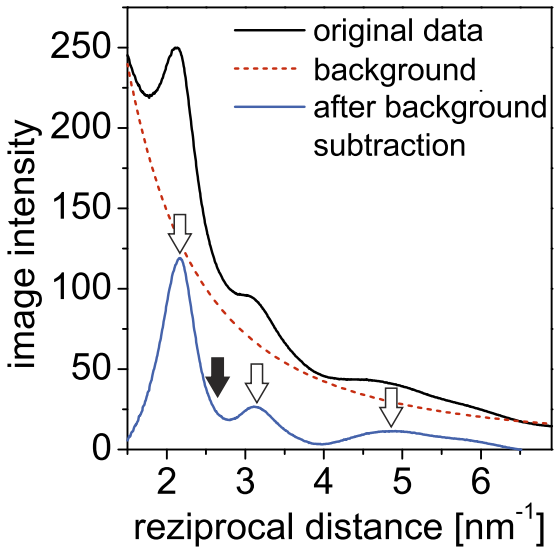

Figure 6.9: Radial intensity linescan of an electron diffraction pattern of the PCDTPBt:$PC_{71}BM$ sample with a mixing ratio of 1:2 and DIO as additive. The background in form of a Lorentz curve is subtracted from the original data. The white arrows mark $PC_{71}BM$ peaks, the black arrow the position of PCDTPBt peak (not visible).

7 Nanomorphology of fluorenyl hexa-peri-hexabenzocoronene-based organic solar cell absorber layers

In this chapter the nanomorphology of FHBC:$PC_{61}BM$ absorber layers of organic solar cells was investigated. Different electron microscopical techniques, atomic force microscopy and grazing incidence wide-angle X-ray scattering were applied for a comprehensive nanomorphology analysis. Furthermore the density of FHBC was determined by low-keV HAADF STEM.
The development of the nanomorphology upon sample annealing and the associated change of the device performance were investigated. It was shown that the annealing process induces a phase separation leading to a bulk heterojunction structure. Due to π-π stacking the FHBC molecules assemble into columnar stacks, which are already present before annealing. While the non-annealed sample consists of a mixture of homogeneously distributed $PC_{61}BM$ molecules and FHBC stacks with a preferential in-plane stack orientation, crystalline FHBC precipitates occur in the annealed samples. These crystals, which consist of hexagonal arranged FHBC stacks, grow with increased annealing time. They are distributed homogeneously over the whole volume of the absorber layer as revealed by electron tomography. The FHBC stacks - whether in the two phase mixture or in the pure crystalline precipitates - exhibit an edge-on orientation, according to results from grazing incidence wide-angle X-ray scattering (GIWAXS), DF TEM imaging and SAED. The best solar cell efficiencies were obtained after 20 and 40 s sample annealing. These annealing times provide an optimized degree of phase separation between donor and acceptor material.

7.1 Materials and methods

FHBC was synthesized by D. D. Jones and W. W. H. Wong (Bio21 Institute, University of Melbourne). Organic solar cells were fabricated and characterized by M. Klein (LTI, KIT) and J. Subbiah (Bio21 Institute, University of Melbourne). GIWAXS measurements were performed by A. Kiersnowski, S. R. Puniredd and W. Pisula (Max Planck Institute for Polymer Research, Mainz)

Solar cell fabrication

BHJ solar cells were fabricated by spin coating of 30-nm-thick layers of PEDOT:PSS; (Baytron AI 4083 from HC Starck) on patterned glass/ITO substrates which were cleaned by acetone, and 2-propanol in an ultrasonication bath and UV/ozone-treated. The PEDOT:PSS films were baked at 140 °C for 10 min in air. A blend of FHBC and $PC_{61}BM$ (99.5 % from Solenne BV) with a ratio of 1:2 was then spin coated from chlorobenzene solution with a thickness of about 75 nm. A TiOx precursor solution (1:200 in methanol) was deposited on the active layer by spin coating (2000 rpm) to form a TiOx layer with a thickness of about 10 nm. The films were exposed to air for about 20 min at room temperature for hydrolysis or baked at 150 °C for 20, 40, 60 and 120 s. The films were transferred to a evaporation chamber where aluminum (100 nm) was deposited through a shadow mask (active area: 0.06 cm^2) at approximately $1 \cdot 10^{-6}$ torr. Film thicknesses were determined by Veeco Dektak 150+ Surface Profiler. *J-V* measurements were carried out with a Keithley 2400 source measurement unit under AM1.5G (1000 W/m^2) illumination from an Oriel solar simulator. The illumination intensity was calibrated using a reference silicon solar cell (PVmeasurements Inc.) certified by the National Renewable Energy Laboratory. Device fabrication and characterizations were performed in an ambient environment without any encapsulation.
For the GIWAXS investigations, the films were spin coated on SiO_2 silicon wafers with a PEDOT:PSS layer.

Sample preparation for electron microscopy investigations

Samples without top electrode were prepared under inert conditions for the nanomorphology studies. The PEDOT:PSS layer thickness was slightly increased (≈45 nm) to facilitate the dissolution of the layer for TEM sample preparation. The samples were annealed at 150 °C for 20-120 s and 300 s. Plan-view samples of the photoactive layers were prepared by the procedure described in Chapter 2.1.1. The sample thickness was about 90 nm for all samples as determined by focused-ion-beam prepared cross-sections.

Electron microscopy

TEM images and diffraction patterns were recorded with a Philips CM200 FEG/ST at 200 keV. The EELS, EFTEM and tomography analyses were performed in an FEI TITAN^3 80-300 at 300 keV. EELS and EFTEM were performed with a Gatan Tridiem 865 HR imaging filter. EEL spectra were recorded with an energy resolution of 0.7 eV and a dispersion 0.05 eV/pixel. 1000 spectra with an exposure time of 0.01 s were acquired and summed up. For the EFTEM images the exposure time was 4 s, and

an energy slit width of 4 eV was chosen. For tomography, a tilt series of bright-field TEM images was acquired in a tilt-angle range of ±77° in steps of 1° with a 'Fischione Model 2020' tomography sample holder, resulting in 155 images. For the tilt series acquisition the software package 'FEI Xplore 3D' was used. Subsequent alignment of the image stack and reconstruction of the tomogram were performed with the 'FEI Inspect3D V3.0' software. The reconstruction of the tomogram is based on the SIRT algorithm (see Chapter 2.6) which was performed with 20 iterations. A sectioning of the tomogram's inner structure was obtained by applying a gray-level threshold to the image stack to distinguish between FHBC and $PC_{61}BM$ regions. The 'Amira/ResolveRT' software was then used to convert the tomogram into a 3D model.

Atomic force microscopy and grazing incidence wide-angle X-ray scattering

AFM topography images were taken with an Asylum Research MFP-3D in the AC mode.

GIWAXS measurements were performed using an instrument consisting of rotating anode X-ray generator (Rigaku Micromax, operated at 42 kV and 20 mA), Osmic confocal MaxFlux optics and a three X/Y slit collimation system (JJ X-ray). Samples on the top of approx. 1×1 cm silicon platelets were irradiated at the incident angle (α_i) of 0.20 °. Diffraction patterns were recorded for 3 h on a MAR345 image plate detector. The camera length (316 mm) and the q-range ($q = 4\pi\sin\theta/2 = 0.12 - 2.0$ Å^{-1}) were calibrated using silver behenate standard. The data was processed and imaged using the Datasqueeze 2.2.9 and Origin 8.6 computer programs.

7.2 Experimental results

7.2.1 Determination of FHBC density

To interpret electron microscopy image intensities the material density is required. Since this property is not known for FHBC, the density was determined according to the procedure described in detail in Chapter 3.4.2. The material parameters which are used for the analysis are summarized in Table 7.1.
The contrast inversion energy was determined for six pure FHBC samples with different thicknesses. The results are presented in Fig. 7.1. The x-error bars represent the deviation of the thickness measurements and the thickness variation within the film. The y-error is due to the inaccuracy of the contrast inversion energy determination. A power-law function $y = a \cdot x^2$ is fitted to the measured values, with $a = (3.34 \pm 0.09) \cdot 10^{-6}$. Using Eq. 3.17 the density can be calculated, giving $\rho = 1041 \pm 294$ kg/m^3.

material	chemical formula	Z_m	A_m
FHBC	$C_{100}H_{98}$	4.32	6.57
$PC_{61}BM$	$C_{72}H_{14}O_2$	5.57	10.35

Table 7.1: Composition and material parameters of FHBC and $PC_{61}BM$.

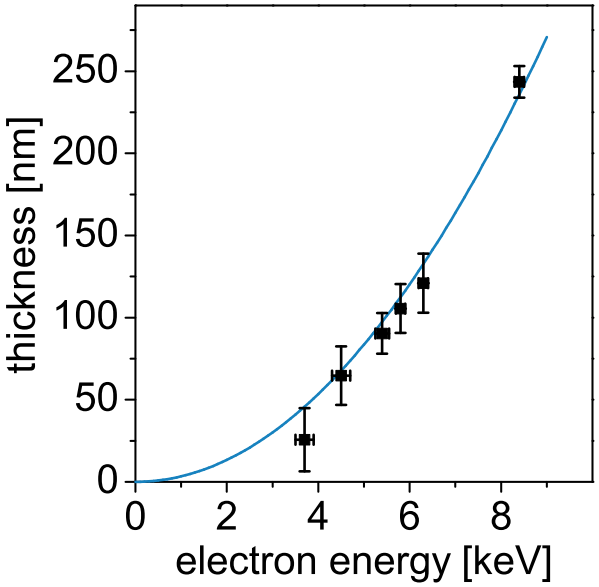

Figure 7.1: Correlation between sample thickness and electron energy at the contrast inversion point for FHBC. The blue curve is a fitted power-law function: $y = a \cdot x^2$.

7.2.2 Photovoltaic performance

To correlate the nanomorphology of the FHBC:$PC_{61}BM$ blends with the performance of the solar cells, the *J-V* characteristics of the devices were measured. The resulting curves under illumination are presented in Fig. 7.2 and the respective photovoltaic key performance data are summarized in Table 7.2.
The FHBC:$PC_{61}BM$ devices annealed for 20 and 40 s at 150 °C show the best device performance with PCEs of between 1.3 % and 1.4 %. The devices annealed for 0, 60 and 120 s exhibit a reduced PCE due to the moderate short-circuit current density J_{SC} and FF. All devices showed a high open-circuit voltage U_{OC}. These results are in agreement with those reported previously [35].

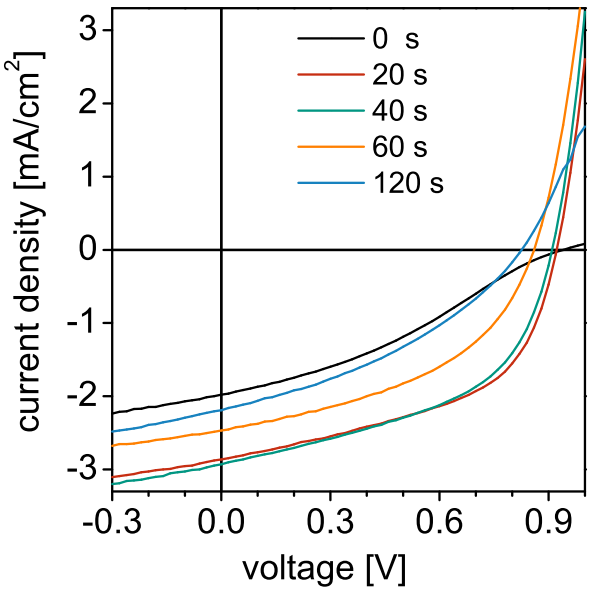

Figure 7.2: J-V characteristics under illumination of FHBC:$PC_{61}BM$ solar cells with different annealing times.

annealing time [s]	J_{SC} [mA/cm^2]	V_{OC} [V]	FF [%]	PCE [%]
0	1.96	0.93	33	0.6
20	2.86	0.92	51	1.4
40	2.93	0.90	50	1.3
60	2.47	0.86	45	1.0
120	2.19	0.82	37	0.7

Table 7.2: Photovoltaic performance of FHBC:$PC_{61}BM$ solar cells with different annealing times.

7.2.3 Nanomorphology investigations

Several electron microscopic techniques (BF TEM and DF TEM, SAED, EFTEM, TEM tomography), AFM and GIWAXS were applied to unravel the complex nanomorphology of the FHBC:$PC_{61}BM$ absorber layers and the development of the nanomorphology with increasing annealing time. First, the results of the non-annealed sample will be shown, thereafter the morphology changes induced by annealing is presented.

Non-annealed sample

Fig. 7.3 presents the results for the non-annealed sample. An AFM topography image is presented in Fig. 7.3a, which reveals depressions with a depth of about 10 nm. The depressions are surrounded by elongated structures (marked with black dashed lines). Additional height variations are visible on larger scale, which can be attributed to layer thickness fluctuations. Examples for a higher and a deeper sample region are encircled in Fig. 7.3a.

To analyze the crystalline structure of the sample, SAED patterns were recorded at 200 keV in a transmission electron microscope. Pure FHBC and $PC_{61}BM$ reference samples were additionally examined to identify the FHBC and $PC_{61}BM$ reflections. The diffraction patterns and the corresponding radial line scans are presented in Fig. 7.4. FHBC is characterized by two relatively sharp reflection rings which can be assigned to a real space distance of 0.35 nm. The inner ring corresponds to the π-π stacking distance displayed in Fig. 1.11. The outer ring at $(0.175\ \text{nm})^{-1}$ is the second order of the inner ring (compare [175]). The reflection rings of pure $PC_{61}BM$ are broad

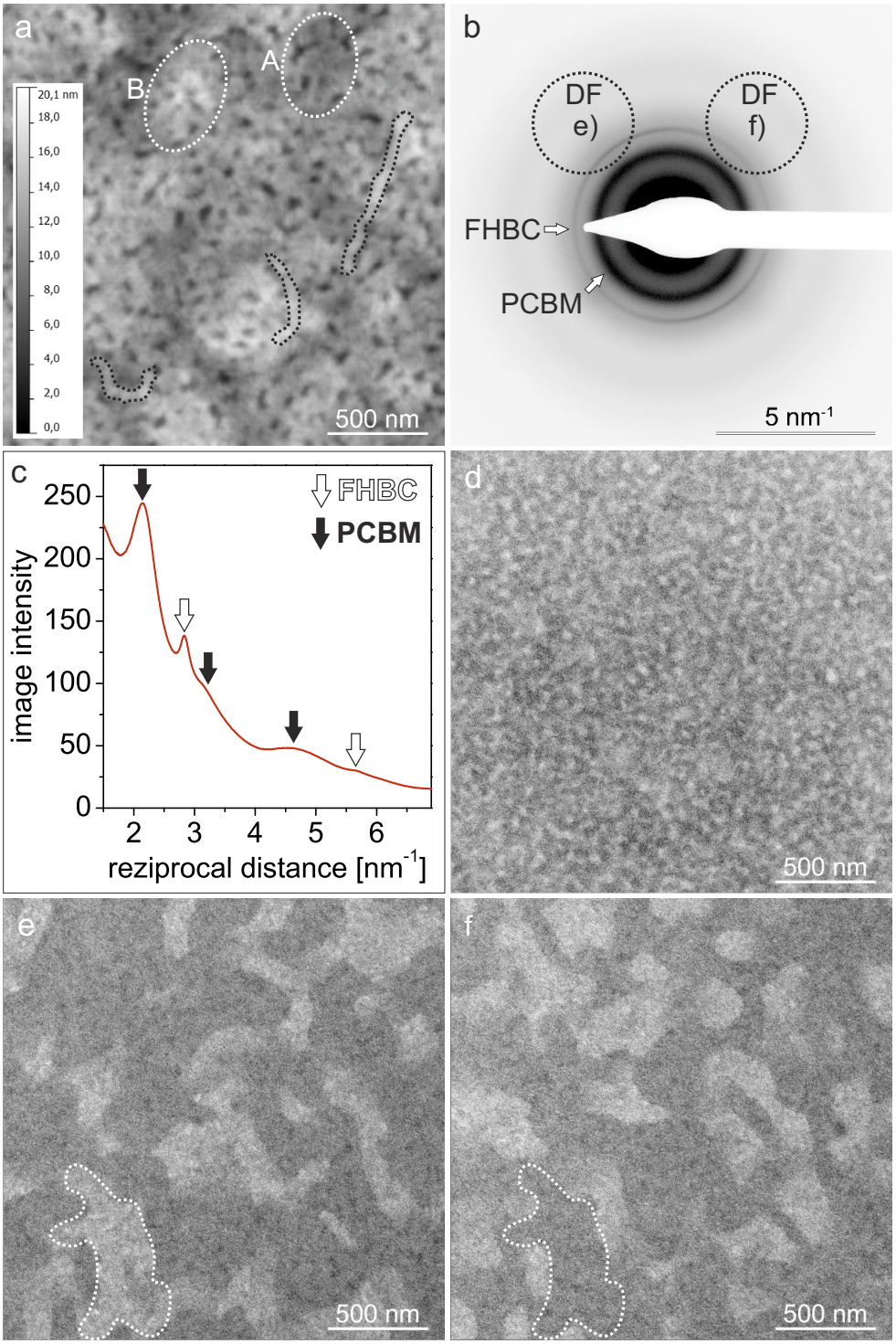

Figure 7.3: Nanomorphology of the non-annealed FHBC:$PC_{61}BM$ sample. a) AFM topography image. The dashed white circles mark a deeper (A) and a higher (B) region of the sample. The dashed black lines mark elongated surface structures; b) contrast-inverted TEM diffraction pattern and aperture positions for the DF images (dashed circles); c) radial line scan of the diffraction pattern; d) BF TEM image; e) and f) FHBC-sensitive DF TEM images taken at 200 keV corresponding to the aperture positions marked in the diffraction pattern. One grain, which shows contrast inversion, is marked in both images.

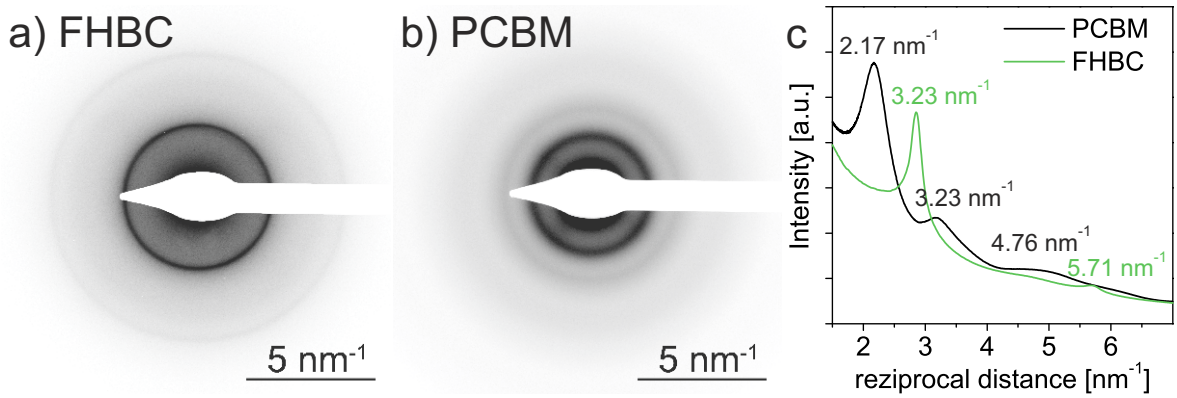

Figure 7.4: TEM diffraction patterns of a) pure FHBC and b) pure $PC_{61}BM$ samples; c) radial intensity linescan of the diffraction patterns

and can be assigned to 0.46, 0.31 and 0.21 nm distances which agree with the results of other groups [27, 72].
A diffraction pattern of the non-annealed FHBC:$PC_{61}BM$ layer is presented in Fig. 7.3b and the corresponding radial intensity linescan in Fig. 7.3c. The diffraction pattern shows three diffuse $PC_{61}BM$ rings with a weak intensity of the two outer rings. One strong and relatively sharp FHBC ring (marked in Fig. 7.3b) is observed while the second ring at $(0.175\ \text{nm})^{-1}$ is barely recognizable. The high intensity of the inner ring indicates that FHBC stacks are already present in the non-annealed sample. The absence of further reflections suggests a preferential alignment of the stack axes parallel to the layer which will be denoted as in-plane stack orientation in the following. Moreover, the inner ring intensity changes azimuthally which is indicative for an inhomogeneous in-plane distribution of FHBC stack orientations. For example, the intensity is higher in the upper left and lower right ring segment. To study the origin of the anisotropy of the FHBC ring, DF TEM images were taken with the positions of the aperture indicated by the dashed circles in Fig. 7.3b. Accordingly, mainly electrons from these specific segments of the FHBC ring contribute to the images. The resulting DF TEM micrographs for the two aperture positions are presented in Fig. 7.3e and f which show bright and dark regions with a size of a few 100 nm. The displacement of the aperture position leads to images with essentially complementary contrast. Exemplarily, one grain is marked in both DF TEM images, which appears bright in Fig. 7.3e and dark in Fig. 7.3f. This clearly indicates a preferential in-plane alignment of FHBC stacks, i.e. a texture, in regions with a few 100 nm size. A BF TEM image taken at the same sample position as Figs. 7.3e,f is presented in Fig. 7.3d. None of the large-scale structures of the DF TEM images are visible here, only small-scale structures prevail. The small bright regions can be correlated with regions of smaller sample thickness due to small-size depression which are observed in the AFM image (Fig. 7.3a).

Samples annealed for 120 s

Fig. 7.5 presents results for the sample annealed for 120 s at 150 °C. The nanomorphology of this sample is representative for all annealed samples. The AFM topography image in Fig. 7.5a shows depressions at the surface with sizes which do not depend on the annealing time. Again, elongated structures surrounding the depressions are visible (marked with black dashed lines). In contrast, the large-scale thickness variations

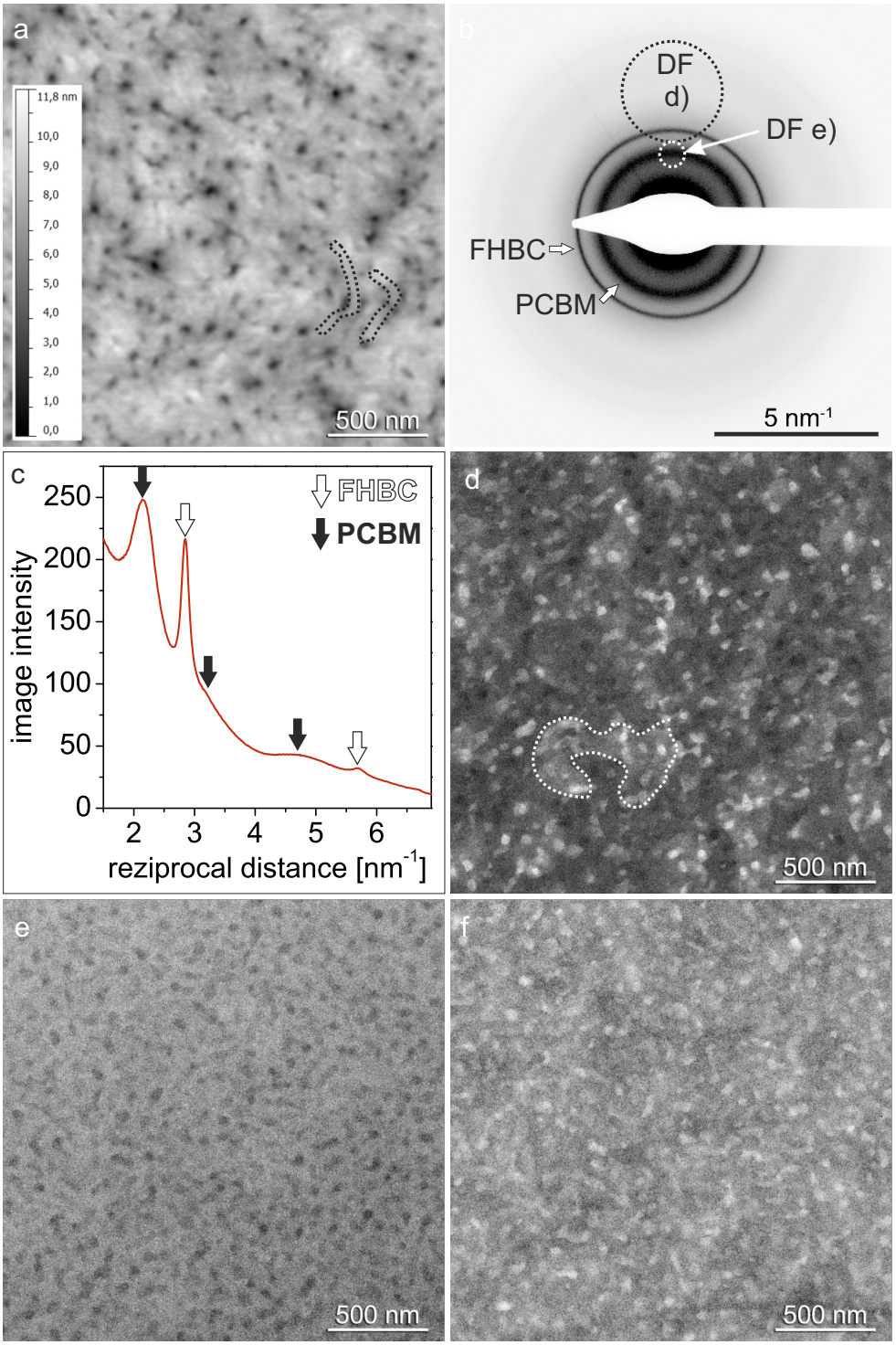

Figure 7.5: Nanomorphology of the FHBC:$PC_{61}BM$ sample annealed for 120 s. a) AFM topography image. The dashed black lines mark elongated surface structures; b) contrast-inverted TEM diffraction pattern and aperture positions for the DF images (dashed circles); c) radial line scan of the diffraction pattern; d) DF TEM image taken at 200 keV corresponding to the aperture position on the FHBC ring (marked in b)). One grain with the same preferential orientation of the FHBC stacks is marked; e) DF image corresponding to the aperture position on the $PC_{61}BM$ ring (also marked in b)) of another sample position; f) BF TEM image taken at the same sample position as the $PC_{61}BM$-sensitive DF image.

disappear almost completely due to the annealing process (note the different height scale of the two AFM images Fig. 7.3a and Fig. 7.5a).
In Fig. 7.5b and c the diffraction pattern and the corresponding radial intensity linescan are shown. In comparison to the non-annealed sample, the FHBC π-π stacking ring exhibits a higher intensity for all annealed samples indicating a higher degree of crystallinity. Azimuthal intensity variations along the FHBC reflection ring are not observed. However, this does not exclude a preferential FHBC stack alignment because the SAED pattern was taken from a relatively large area, which may contain differently textured grains. Grains with preferentially aligned FHBC stacks are indeed still present as demonstrated by the DF TEM image Fig. 7.5d which was taken with the aperture position marked by d) in Fig. 7.5b. In addition, small bright regions with a size of a few 10 nm appear in Fig. 7.5d which are absent in the non-annealed samples. The high intensity of these regions suggests crystalline FHBC precipitates. The presence of crystalline FHBC is supported by the high intensity and small width of the FHBC ring in the diffraction pattern (Figs. 7.5b,c). The DF TEM image in Fig. 7.5e was taken with the aperture position shifted to the $PC_{61}BM$ ring. A smaller aperture was chosen to exclude any contribution from FHBC and select only the intensity of the $PC_{61}BM$ ring (see Fig. 7.5b aperture position e). The $PC_{61}BM$-sensitive DF TEM image shows a homogeneous intensity apart from the interspersed dark regions which can be assigned to the FHBC precipitates. Fig. 7.5d suggests that the $PC_{61}BM$ distribution is homogeneous in the phase surrounding the FHBC precipitates. It can be concluded that a two-phase structure is present after annealing which consists of a FHBC:$PC_{61}BM$ mixture and crystalline FHBC precipitates. Within the FHBC:$PC_{61}BM$ mixture, grains are formed with a preferential alignment of FHBC stacks. The BF TEM image Fig. 7.5f shows small bright regions which can be either correlated with the FHBC precipitates or regions of smaller sample thickness. However, the grain structure with preferentially oriented FHBC stacks cannot be visualized by BF TEM.

Development of the nanomorphology during annealing

By comparing FHBC-sensitive DF TEM images of samples with different annealing times (Fig. 7.6), it becomes apparent that the crystalline FHBC precipitates are formed quickly already after only 20 s annealing time. If the annealing time is increased, the FHBC crystallites grow slightly, but the large-scale texture of FHBC stacks in the

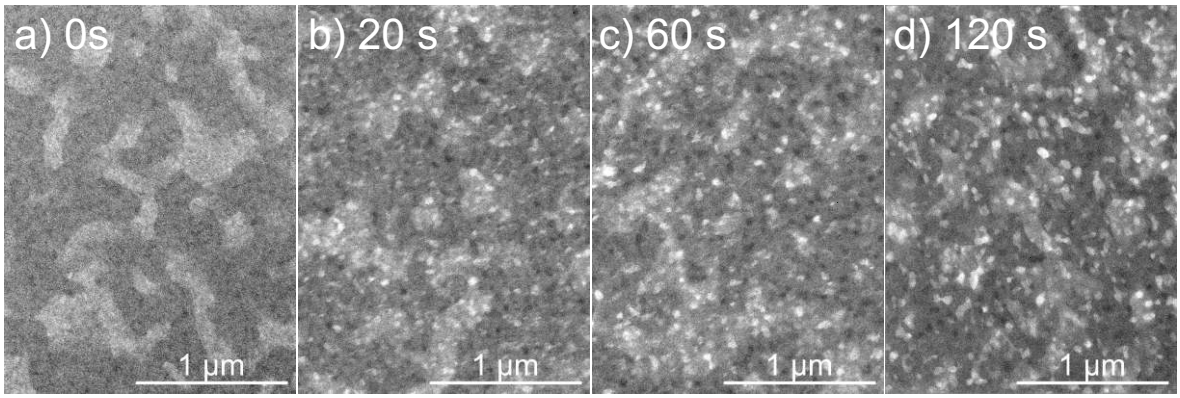

Figure 7.6: FHBC-sensitive DF TEM images of samples annealed for a) 0, b) 20, c) 60 and d) 120 s.

FHBC:$PC_{61}BM$ mixture remains.
To analyze the development of the morphology at even longer annealing times, a sample annealed for 5 min was investigated. In Fig. 7.6 a FHBC-sensitive DF TEM image is presented. The size of the FHBC-rich crystallites further increases as compared to the sample annealed for 120 s and, in addition, large $PC_{61}BM$ crystals with sizes of a few microns appear. The $PC_{61}BM$ crystal in Fig. 7.7 appears bright because some of the $PC_{61}BM$ reflexes are also selected with the aperture. The $PC_{61}BM$ crystal is surrounded by a FHBC-rich region, which appears bright if the crystalline orientation corresponds to the aperture position (marked with red arrows) and dark if not (green arrows).
The increase of the average FHBC precipitate size is plotted in Fig. 7.8 as a function of the annealing time. It increases from 42±10 nm for 20 s annealing to 83±20 nm for 300 s annealing. The error bar represents the standard deviation of the size distribution.

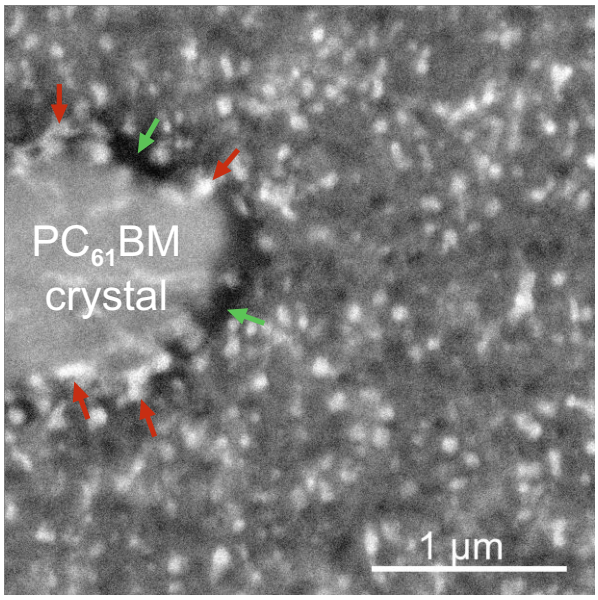

Figure 7.7: FHBC-sensitive DF TEM image of the FHBC:$PC_{61}BM$ sample annealed for 5 min. The $PC_{61}BM$ crystal is surrounded by a FHBC-rich region which appears either bright (marked with red arrows) if the crystalline orientation corresponds to the aperture position or dark (green arrows) if not.

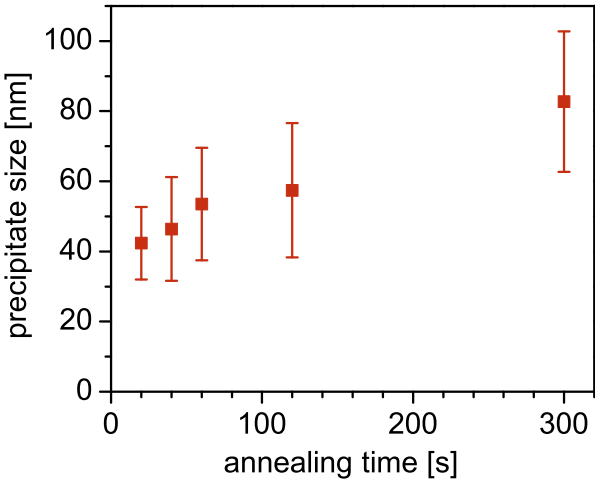

Figure 7.8: Mean FHBC precipitate size as a function of the annealing time (determined from the FHBC-sensitive DF TEM images). The error bar represents the standard derivation of the size distribution.

High-resolution transmission electron microscopy analysis

A HRTEM image of the sample annealed for 60 s is presented in Fig.7.9 which is representative for all annealed samples. Lattice fringes are observed in the regions marked by dashed lines in Fig.7.9a, which are indicative for a crystalline structure. Fig.7.9b shows the crystalline region in the dashed square with a higher magnification. To determine the distance of the lattice fringes the Fourier transform of this image was calculated (Fig.7.9c). Two bright spots are visible in addition to the zero-order beam, which correspond to a lattice fringe distance of 2.15±0.15 nm. This distance can be well correlated to the lattice plane distance in the hexagonally arranged pure FHBC stacks (Fig.1.11c). A detailed analysis will follow in the discussion section.

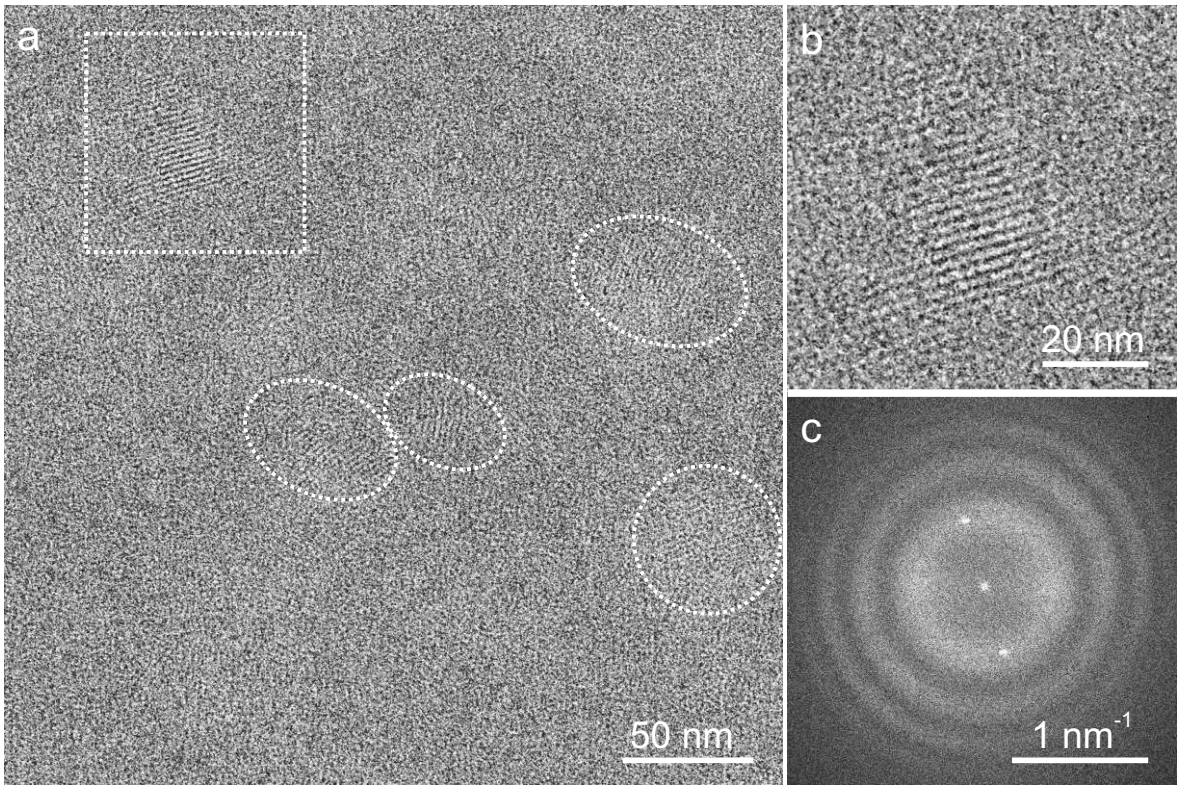

Figure 7.9: 200 keV HRTEM image of the FHBC:$PC_{61}BM$ sample annealed for 60 s. Crystalline regions are encircled, b) enlarged image of the dashed square in the HRTEM image, c) Fourier transform of HRTEM image.

Energy-filtered transmission electron microscopy investigations

To confirm the interpretation of the images in Fig. 7.5 with respect to the distribution of $PC_{61}BM$ and FHBC, EFTEM was applied. For this purpose, reference EEL spectra of pure FHBC and pure $PC_{61}BM$ were recorded which are presented in Fig. 7.10d. The maxima of the plasmon peaks are clearly different for the two materials (FHBC at an energy loss of 22.5 eV, $PC_{61}BM$ at 26.2 eV). This is exploited, to take EFTEM images at different energy losses (Fig. 7.10a-c) to reveal the distribution of FHBC and $PC_{61}BM$. The hatched rectangles in Fig. 7.10d mark the corresponding energy loss windows which were selected with a slit width of 4 eV. The EFTEM image Fig. 7.10a was taken with a slit position centered at an energy loss of 20 eV. For this energy

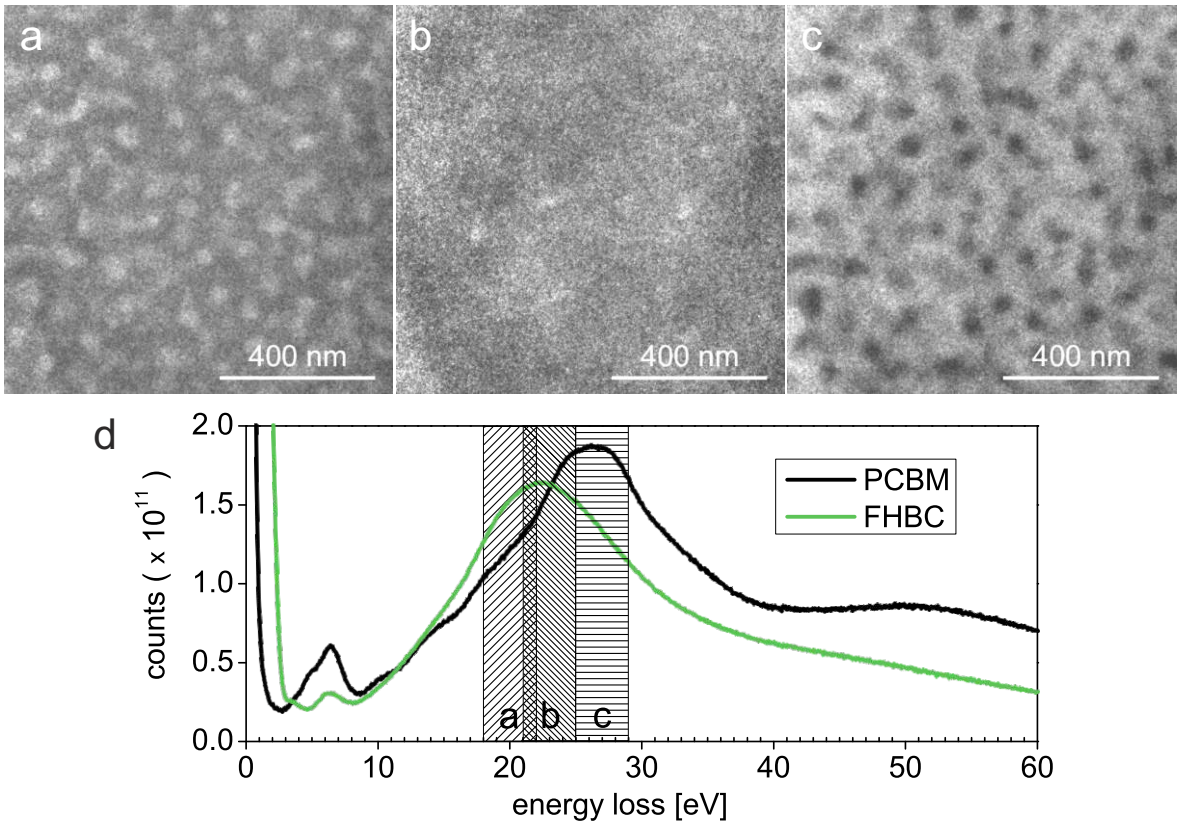

Figure 7.10: EFTEM images of the FHBC:$PC_{61}BM$ sample annealed for 60 s. The images are taken with a slit width of 4 eV centered at energy losses of a) 20 eV, b) 23 eV and c) 27 eV. d) Low-loss EEL spectra of pure $PC_{61}BM$ and FHBC. The slit positions for the EFTEM images are marked by the hatched rectangles.

loss the FHBC signal distinctly exceeds the $PC_{61}BM$ signal leading to a higher image intensity of the FHBC-rich regions. For the second slit position centered at 23 eV, the two signals have the same intensity, and changes of the image contrast in Fig. 7.10b can be interpreted in terms of thickness variations. The last slit position centered at 27 eV exhibits a higher $PC_{61}BM$ signal. The $PC_{61}BM$-rich phase appears brighter in the EFTEM image Fig. 7.10c. This image closely resembles the $PC_{61}BM$-sensitive DF TEM image (Fig. 7.5d), in which the $PC_{61}BM$ also appears brighter than the FHBC. The comparison of Fig. 7.10a and Fig. 7.10b shows complementary contrast indicating that small FHBC precipitates are embedded in a $PC_{61}BM$:FHBC blend.

Electron tomography

TEM tomography was applied to analyze the 3D structure of the sample. In Fig. 7.11 three slices extracted from the top (Fig. 7.11a), center (Fig. 7.11b) and bottom (Fig. 7.11c) of the reconstructed volume are shown. FHBC-rich regions appear dark because the image contrast was inverted for improved visibility. The dark FHBC precipitates are distributed homogeneously over the whole sample thickness, but seem to be slightly larger close to the bottom of the sample (Fig. 7.11c). Fig. 7.11a shows a slice close to the sample surface, where bright structures are visible in the upper right corner (marked with arrows). They correspond to the faint elongated structures in the AFM images (Fig. 7.3a and Fig. 7.5a) which surround the depressions. By applying a threshold

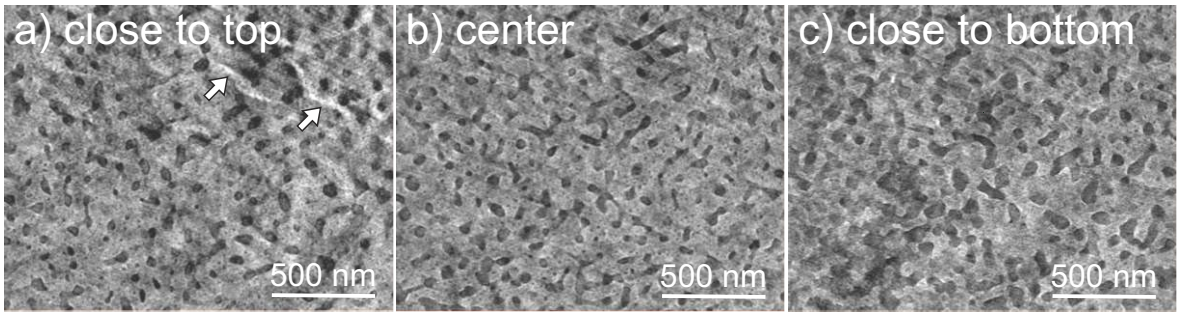

Figure 7.11: Slices extracted from the TEM tomogram of the sample annealed for 60 s. FHBC precipitates appear dark because the contrast is inverted for better visibility. a) Slice close to the top, b) slice from the center and c) slice close to the bottom of the sample. The white arrows in a) indicate elongated surface structures.

gray value to the reconstructed volume, the FHBC domains could be extracted and a 3D-model of the FHBC distribution was obtained. The video of the rotating 3D model confirms that the FHBC domains are homogeneously distributed over the whole volume of the sample.

Grazing incidence wide-angle X-ray scattering

GIWAXS was performed to study the crystalline organization of the FHBC:$PC_{61}BM$ sample after annealing at 150 °C for up to 120 s. The GIWAXS pattern of the sample before annealing (not presented) does not exhibit any reflections, indicating none or very poor order on a macroscopic scale (few cm^2) in the probed volume. Fig. 7.12a shows the GIWAXS pattern of a pure annealed FHBC sample which was processed in the same way as the FHBC:$PC_{61}BM$ blend. Three discrete reflections can be recognized

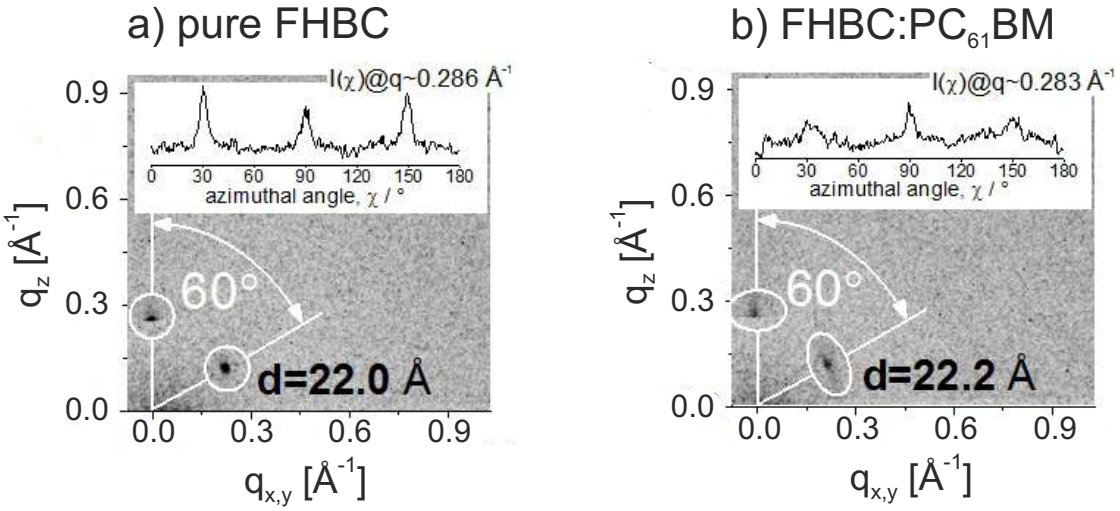

Figure 7.12: GIWAXS patterns of a) pure FHBC and b) FHBC:$PC_{61}BM$ blend after annealing at 150 °C for 120 s with indicated azimuthal angle and d-spacing. Insets show the azimuthal intensity distributions ($I(\chi)$) at the scattering vectors q corresponding to reflections of the hexagonal structure.

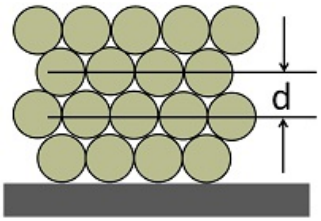

Figure 7.13: Schematic illustration of the hexagonal arrangement of FHBC stacks on the surface.

in the meridional and off-meridional planes which are characteristic for a hexagonal organization of the columnar stacks with their columnar axes oriented parallel to the surface as illustrated in Fig. 7.13. The respective distance between the FHBC stack layers corresponds to d=2.20 nm which agrees well with the lattice fringe distance of 2.15 nm in the HRTEM image of the FHBC:$PC_{61}BM$ blend after annealing (Fig. 7.9). Due to the low crystalline order on a macroscopic scale, only the 1st order reflections appear without higher order reflections. Reflections from the FHBC π-π stacking are, however, not observed though confirmed by HRTEM. This observation may indicate that, at the macroscopic scale, hexagonal ordering of the FHBC columns in the films dominates over the π-π interaction-driven assembly of the FHBC molecules within the columns. The GIWAXS pattern of the FHBC:$PC_{61}BM$ blend (sample annealed for 120 s at 150 °C) (Fig. 7.12b) resembles the GIWAXS pattern of pure FHBC (Fig. 7.12a). However, the azimuthal intensity distribution of the main reflection indicate a decrease of order if $PC_{61}BM$ is added (comparison of insets of Fig. 7.12a and b). This can be inferred from the smearing out of the reflections along the azimuthal angle in the inset of Fig. 7.12b, while these reflections are quite sharp for of pure FHBC (inset of Fig. 7.12a).

7.3 Discussion

Detailed information on the nanomorphology of the FHBC:$PC_{61}BM$ absorber layers and the effect of annealing was obtained by combining several electron microscopic techniques, AFM and GIWAXS. At first the focus will be on the nanomorphology of the FHBC:$PC_{61}BM$ blend before annealing. The images and SAED pattern in Fig. 7.3 demonstrate that the non-annealed sample consists of a homogeneous mixture of $PC_{61}BM$ and FHBC stacks. The FHBC stack axes are preferentially oriented parallel to the substrate with an additional azimuthal texture in regions with a typical size between a few 100 nm and 1 µm. The $PC_{61}BM$ molecules are homogeneously distributed and do not agglomerate to form, e.g., pure $PC_{61}BM$ crystallites. This is illustrated in Fig. 7.14a where a scheme of the nanomorphology of the non-annealed FHBC:$PC_{61}BM$ sample is shown.

The morphology of the annealed samples is schematically summarized in Fig. 7.14b. The most notable change of the nanomorphology after annealing consists in the precipitation of crystalline FHBC as demonstrated by the DF TEM (Fig. 4c, Fig. 5b-d), HRTEM (Fig. 6) and the GIWAXS data (Fig. 9). The FHBC stacks are arranged in a hexagonal symmetry as indicated in Fig. 1c and Fig. 9c. The GIWAXS data confirm that the stack axes in the precipitates are indeed preferentially oriented parallel to the substrate (Fig. 9b). $PC_{61}BM$-sensitive EFTEM (Fig. 7c) and DF TEM images (Fig. 4d) reveal a homogeneous distribution of the $PC_{61}BM$ molecules. Furthermore FHBC-sensitive DF TEM images (Fig. 4c and Fig. 5b-d) show that the surrounding $PC_{61}BM$:FHBC blend contains regions with preferentially aligned FHBC stacks as the non-annealed sample. The size of these regions does not change with increasing annealing time. In contrast, the pure FHBC precipitates grow slightly with increasing annealing time, which becomes apparent in the FHBC-sensitive DF TEM images of

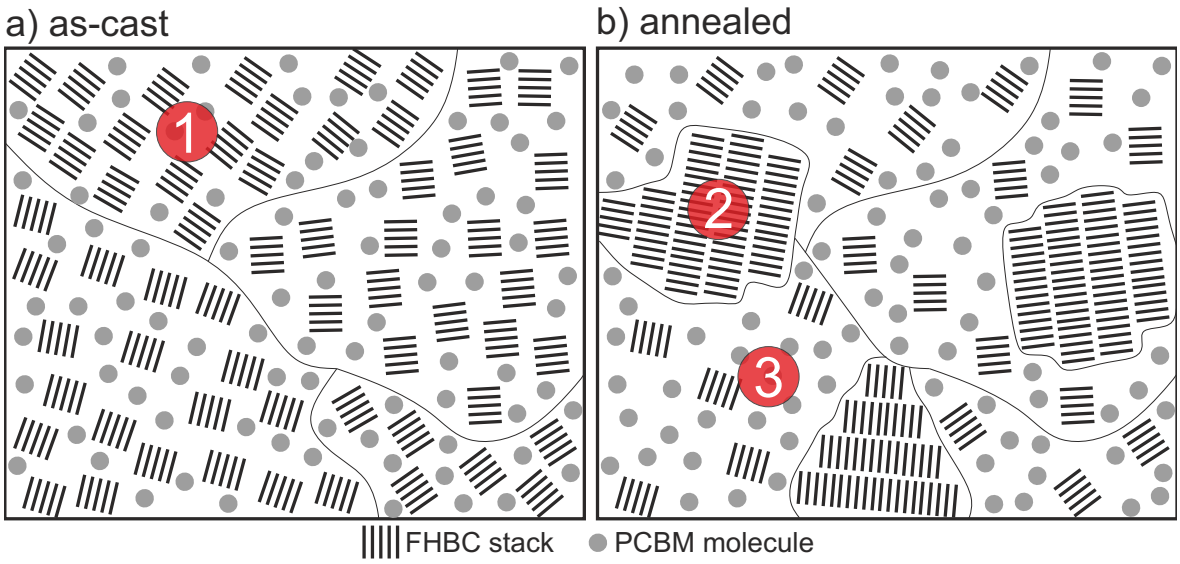

Figure 7.14: Schematic illustration of the nanomorphology of a) non-annealed and b) annealed FHBC:$PC_{61}BM$. Before annealing, the sample consists of a homogeneous mixture of FHBC and $PC_{61}BM$. Grains (1) exist with FHBC stacks which are preferentially aligned parallel to the substrate. During annealing FHBC crystals are precipitated (2) from the textured FHBC:$PC_{61}BM$ mixture (3).

the annealing series in Fig. 5 and the graph in Fig. 7.8. The growth of the FHBC precipitates leads to an FHBC depletion of the surrounding FHBC:$PC_{61}BM$ blend. For long annealing times (5 min), large $PC_{61}BM$ precipitates are formed which may be initiated by the FHBC depletion of the FHBC:$PC_{61}BM$ blend. The precipitation of large $PC_{61}BM$ crystals has been observed before for long annealing times and high $PC_{61}BM$ concentrations in other $PC_{61}BM$-based absorber layer blends, e.g., in P3HT:$PC_{61}BM$ blends [72, 73].
Electron tomography (Fig. 7.11) reveals that the FHBC precipitates are homogeneously distributed over the entire sample volume. However, the FHBC precipitate size is slightly larger close to the bottom of the layer which indicates that FHBC precipitation is slightly favored at the interface to the PEDOT:PSS. The annealing process induces only minor changes of the surface topography. The AFM image of the annealed sample (Fig. 7.5a) exhibits the same 10 nm deep depressions as the image of the non-annealed sample (Fig. 7.3a). Only the large-scale thickness variations are reduced.
The nanomorphology of the FHBC:$PC_{61}BM$ blends can be correlated with the photovoltaic performance of the respective solar cells. Annealing of the active layer is required to substantially improve the device power conversion efficiency. The *J-V* characteristic of the non-annealed device shows a pronounced S-shape. Thermal annealing of the active layer leads to the precipitation of crystalline FHBC. Large $PC_{61}BM$ crystals only appear after very long annealing times. The improved morphology leads to improved pathways for charge migration, and therefore enhances the device performance. The samples annealed for 20 and 40 s exhibit the best PCE of 1.3 % and 1.4 %, respectively. This indicates that the absorber layer is sensitive towards small changes of the FHBC precipitate size. A mean size of the crystalline FHBC precipitates in the range of 42-46 nm (obtained after 20 and 40 s of annealing at 150 °C), surrounded by a homogenous mixture of FHBC stacks and $PC_{61}BM$, yields the best exciton dissociation and charge transport among the studied samples. The moderade PCE of the cells can be attributed to the FHBC stack orientation ‘edge-on’, i.e. parallel to the substrate plane. This orientation is unfavorable for charge transport which preferentially occurs along the FHBC stack axis. Additionally, the insulation side chains of the FHBC molecules impede the charge transport perpendicular to the substrate. The effect of interface modifiers to induce a more favorable organization of the FHBC columns, where the columns are oriented perpendicular, i.e. ‘face-on’, to the absorber layer is currently being examined. This orientation would support efficient charge carrier transport to the electrodes.

Summary

This work is concerned with the analysis of the nanomorphology of organic solar cells which strongly influences their efficiency. A broad range of electron microscopic techniques was applied to image the distribution of donor and acceptor domains of absorber layers in different material systems for organic solar cells. The results of the nanomorphology studies contributed to the fundamental understanding of the correlation between nanomorphology of the absorber layer, the fabrication parameters, optoelectronic properties and the efficiency of the organic solar cell. The findings were exploited to control the nanomorphology and to finally enhance the performance of the solar cells.

The main obstacle for the application of transmission electron microscopy is often the weak contrast between donor and acceptor domains which are characterized by similar material density and average atomic number. **Low-energy high-angle annular dark-field scanning transmission electron microscopy** (low-keV HAADF STEM) performed in a scanning electron microscope at electron energies between 3 keV and 30 keV was applied for the first time on these material systems. Low-keV HAADF STEM provides strong material contrast but requires modeling of the image intensity because intuitive interpretation is not straightforward. The low-keV HAADF STEM intensity is characterized by an intensity maximum and corresponding contrast inversion which depends on the sample thickness and material properties. Monte-Carlo (MC) simulation were tested but did not always show good agreement between the HAADF STEM intensity of low-atomic number reference samples with known properties and simulated intensities. Instead, the HAADF STEM intensity can be well described by a semi-empirical formalism which is based on an equation for the mean square scattering angle suggested by Bothe. The formalism derived in this work is a powerful tool to understand and interpret low-keV HAADF STEM images. It facilitates the determination of the optimum electron energy for maximum image contrast. The formalism also allows the determination of the sample thickness (if the material properties are known) or material density (if the sample thickness and average atomic number are known).

Four different material systems were studied in the work. In the following the results of these investigations are summarized individually.

Organic solar cell absorber layers composed of **P3HT and $PC_{61}BM$** are most frequently investigated. The formation of P3HT and $PC_{61}BM$ domains with appropriate sizes is considered to be essential for the achievement of high efficiencies. The nanomorphology was analyzed as a function of the P3HT molecular weight (20 kg/mol and 50 kg/mol), solvent annealing and post-annealing treatments at 150 °C for up to 30 min. A combination of low-keV HAADF STEM, bright-field transmission electron microscopy (BF TEM), electron diffraction and atomic force microscopy (AFM) was applied to study the nanomorphology of this material system. Low-keV HAADF

STEM is well suited to reveal the domain structure in these absorber layers, despite the extremely small difference of the material properties of P3HT and $PC_{61}BM$. It could be shown that P3HT nanorods are formed during annealing only in samples containing P3HT with a low molecular weight of 20 kg/mol. P3HT:$PC_{61}BM$ films with 50 kg/mol P3HT contain only small globular structures that do not change in size after annealing at 150 °C for up to 30 min. While BF TEM is adequate to image P3HT nanorods, the small globular P3HT structures cannot be resolved by BF TEM imaging, which suggests low-keV HAADF STEM as a favorable addition to the established imaging techniques.

The nanomorphology and optoelectronic properties of organic solar cells comprising **P3HS:$PC_{61}BM$** bulk heterojunctions (BHJs) were correlated in this work. Using low-keV HAADF STEM, it was possible to clearly distinguish P3HS and $PC_{61}BM$ domains within the active layers of organic photovoltaic devices. Upon thermal annealing, the formation of P3HS nanorods was observed within the P3HS:$PC_{61}BM$ blend. Nanorod formation is attributed to self-organization in connection with improved π-π stacking of the molecules. Furthermore, low-keV STEM images of ultramicrotome cross-section samples showed an increased P3HS concentration at the anode side of the absorber layer, which is beneficial for the performance of the solar cell device.
Concerning the optoelectronic properties it could be shown that the absorption of photons with lower energies and the charge carrier mobilities are enhanced after annealing resulting in an increased current density and fill factor of the organic solar cells. Consequently, the power conversion efficiencies were improved up to about five times.

The nanomorphology of organic solar cell absorber layers based on the conjugated polymer **PCDTPBt** blended with **$PC_{61}BM$ or $PC_{71}BM$** were investigated and correlated with the optoelectronic properties of the devices. Low-keV HAADF STEM and energy dispersive X-ray spectroscopy (EDXS) investigations, which revealed the nanomorphology of the absorber layers, contributed to further enhancement of the solar cell performance. A network of PCDTPBt- and $PC_{61}BM$-rich phases was revealed in all samples, with a strong influence of the blend mixing-ratio on the domain size. The highest power conversion efficiency of 4.6% and a fill factor (FF) of 70 % could be achieved for PCDTPBt:$PC_{71}BM$-based solar cells with 1,8-diiodooctane (DIO) as processing additive. Low-keV HAADF STEM investigations revealed a finer bulk morphology of the active layer for these samples. By comparing the results of electron diffraction and grazing incident X-ray diffraction (GIXD) studies the orientation of the PCDTPBt molecules was revealed. It could be shown that in the absorber layer with DIO as processing additive the PCDTPBt molecules exhibit a face-on configuration which is beneficial for the vertical hole transport in the absorber layer.

The nanomorphology and power conversion efficiency of **FHBC:$PC_{61}BM$**-based BHJ organic solar cells was studied and correlated before and after annealing at 150 °C for up to 120 s. The application of several electron microscopic techniques, AFM and grazing incidence wide-angle X-ray scattering (GIWAXS) revealed the complex nanomorphology of the FHBC:$PC_{61}BM$ layers and its dependence on the annealing treatment. The FHBC molecules assemble into columnar stacks which are already present before annealing. Non-annealed samples consist of a mixture of homogeneously distributed $PC_{61}BM$ molecules and FHBC stacks with a preferential in-plane stack orientation.

During annealing, FHBC crystallites with a hexagonal structure are precipitated from the FHBC:$PC_{61}BM$ mixture. They exhibit the same crystalline structure like pure FHBC and grow with increasing annealing time. Electron tomography investigations further revealed that the FHBC precipitates are distributed homogeneously over the whole volume of the absorber layer. The best solar cell efficiencies were obtained for samples annealed for 20 s and 40 s. This annealing time yields the best donor/acceptor phase separation with an average domain size of about 45 nm.

Outlook

Organic solar cells will remain to be highly interesting in the future due to their potential for low-cost roll-to-roll production. An enormous increase of the organic solar cell device efficiency could be observed in the last decade [176] and many researchers are confident that in the near future efficiencies of over 15 % will be achievable [177]. Together with an improved long-term stability this would make organic solar cells competitive to anorganic thin-film solar cells.
Since the performance of organic solar cells is strongly correlated with the nanomorphology of the absorber layers, appropriate investigation techniques will be essential for further developments. Low-energy electron microscopic techniques will grow in popularity, especially for the analysis of low-density carbon-based materials, which exhibit low contrast and are sensitive towards electron beam-damage. Further developments in the field of lens aberration correction are under way. The combination of spherical and chromatic aberration correction will yield a resolution of 1 Å or better at 20 keV electron energy [178]. It also will facilitate high-resolution energy-filtered images using characteristic energy losses of the component of interest.

Acronyms

2D	two-dimensional
3D	three-dimensional
AFM	atomic force microscopy
ADF	annular dark-field
AM	air mass
ART	algebraic reconstruction technique
ASTM	American Society for Testing and Material Standards
BF	bright field
BHJ	bulk heterojunction
BSE	backscattered electron
CB	chlorobenzene
DCB	1,2-dichlorobenzene
DF	dark-field
DIO	1,8-diiodooctane
DSC	differential scanning calorimetry
EDX	energy dispersive X-ray
EDXS	energy dispersive X-ray spectroscopy
EEL	electron energy loss
EELS	electron energy loss spectroscopy
EFTEM	energy-filtered transmission electron microscopy
ESEM	environmental scanning electron microscopy
ESI	electron spectroscopic imaging
FEG	field-emission gun
FF	fill factor
FHBC	fluorenyl hexa-*peri*-hexabenzocoronene
FIB	focused ion beam
GIF	gatan imaging filter
GIS	gas injection system
GIWAXS	grazing incidence wide-angle X-ray scattering
GIXD	grazing incident X-ray diffraction
HAADF	high-angle annular dark-field
HBC	hexa-*peri*-hexabenzocoronene
high-keV STEM	high-energy scanning transmission electron microscopy
HOMO	highest occupied molecular orbital
HRTEM	high-resolution transmission electron microscopy
ITO	indium tin oxide
J-V	current density-voltage
KIT	Karlsruhe Institute of Technology
low-keV STEM	low-energy scanning transmission electron microscopy
LTI	Light Technology Institute
LUMO	lowest unoccupied molecular orbital
MC	Monte Carlo

MDMO-PPV	poly(2-methoxy-5-(3'-7'-dimethyloctyloxy)-1,4-phenylenevinylene
MPP	maximum power point
MW	molecular weight
ODT	1,8-octanedithiol
OPV	organic photovoltaic
P3HS	poly(3-hexylselenophene-2,5-diyl)
P3HT	poly(3-hexylthiophene-2,5-diyl)
$PC_{61}BM$	[6,6]-phenyl-C_{61}-butyric acid methyl ester
$PC_{71}BM$	[6,6]-phenyl-C_{71}-butyric acid methyl ester
PCDTBT	poly[N-9'-heptadecanyl-2,7-carbazole-*alt*-5,5-(4',7'-di-2-thienyl-2',1',3'-benzothiadiazole)]
PCDTPBt	poly[*N*-9'-heptadecanyl-2,7-carbazole-*alt*-5,5-(4',7'-di-2-thienyl-2'-(3,5-difluoro-4-octyldodecyloxyphenyl)-2'*H*-benzotriazole)]
PCE	power-conversion efficiency
PDI	polydispersity index
PEDOT:PSS	poly(3,4-ethylenedioxythiophene):polystyrenesulfonate
PET	polyethylene terephthalate
PTB7	poly[[4,8-bis[(2-ethylhexyl)oxy]benzo[1,2-b:4,5-b']dithiophene-2,6-diyl][3-fluoro-2-[(2-ethylhexyl)carbonyl]thieno[3,4-b]thiophenediyl]]
PVP	polyvinylpyrrolidone
RR	regioregularity
SAED	selected area electron diffraction
SE	secondary electron
SEM	scanning electron microscopy
SIMS	secondary ion mass spectrometry
SIRT	simultaneous iterative reconstruction technique
STEM	scanning transmission electron microscopy
TCO	transparent conductive oxide
TEM	transmission electron microscopy
UV	ultraviolet
WAXS	wide-angle X-ray scattering
WBP	weighted back-projection
WD	working distance
XRD	X-ray diffraction
ZnPc	zinc phthalocyanine

Symbols

A	atomic mass number
a	prefactor of the power-law fit function
a_H	Bohr radius
A_m	mean atomic mass number
α	impact angle
b	exponent of the power-law fit function
CF	correction factor
$\frac{d\sigma}{d\Omega}$	differential scattering cross section
e	elementary charge
E	energy
$\bar{E}$	mean energy
E_{loss}	energy loss
$\bar{E}_i$	mean energy for electron-hole pair excitation
E_{th}	threshold energy
ϵ_0	electric constant
ϵ_c	charge collection efficiency
FF	fill factor
G	detector gain
η_A	photon-absorption efficiency
η_c	backscattering coefficient
η_{CC}	charge-collection efficiency
η_{CT}	charge-transfer efficiency
η_{ED}	exciton-diffusion efficiency
η_{EQE}	external quantum efficiency
η_{IQE}	internal quantum efficiency
I	electron intensity
I_0	intensity of incoming electrons
I_{cc}	collection current
I_{MPP}	current at the maximum power point
I_{SC}	short-circuit current
I_{HAADF}	HAADF intensity
J	current density
J_{SC}	short-circuit current density
λ	de Broglie wavelength
Λ	mean free path length
L_{ED}	exciton diffusion-length
m	mass
M_n	number average molecular weight
M_w	weight average molecular weight
N	number of atoms per unit cell
p	number of collisions
P_{Light}	light power

P_{SC}	solar cell power
R	screening length
ρ	density
σ_t	total cross section
S_1	single scattering function
S_m	m-fold scattering function
t	sample thickness
T_{Dep}	deposition temperature
T_g	glass transition temperature
θ	scattering angle
θ_0	characteristic angle
θ_1	outer HAADF STEM detection angle
θ_2	inner HAADF STEM detection angle
$\overline{\theta^2}$	mean quadratic scattering angle
$\overline{\theta_C^2}$	mean quadratic scattering angle according to Cosslett & Thomas
$\overline{\theta_B^2}$	mean quadratic scattering angle according to Bothe
v	velocity
V	voltage
V_{MPP}	voltage at the maximum power point
V_{OC}	open-circuit voltage
x	distance
Z	atomic number
Z_m	mean atomic number

List of Figures

List of Tables

Bibliography

[1] G. Masson, M. Latour, M. Rekinger, I.-T. Theologitis, and M. Papoutsi. *Global market outlook for photovoltaics 2013-2017*. Editor: C. Winneker, European Photovoltaic Industry association (EPIA) (2013).

[2] P. Galuszka. China & India are building 4 new coal power plants - every week. `http://www.thegwpf.org` (2012).

[3] J. J. M. Halls and R. H. Friend. *Clean electricity from photovoltaics*, chapter 9: Organic photovotaic devices, pages 377–445. Series on photoconversion of solar energy 1. Imperial College Press, London (2001). ISBN: 1-86094-161-3.

[4] C. W. Tang. Two-layer organic photovoltaic cell. *Applied Physics Letters*, **48**(2), 183–185 (1986). `doi:10.1063/1.96937`.

[5] G. Yu, J. Gao, J. C. Hummelen, F. Wudl, and A. J. Heeger. Polymer photovoltaic cells: Enhanced efficiencies via a network of internal donor-acceptor heterojunctions. *Science*, **270**(5243), 1789–1791 (1995). `doi:10.1126/science.270.5243.1789`.

[6] J. Halls, C. Walsh, N. Greenham, E. Marseglia, R. Friend, S. Moratti, and A. Holmes. Efficient photodiodes from interpenetrating polymer networks. *Nature*, **376**, 498–500 (1995). `doi:10.1038/376498a0`.

[7] Heliatek. press release january 13. 2013. `http://www.heliatek.com/wp-content/uploads/2013/01/130116_PR_Heliatek_achieves_record_cell_effiency_for_OPV.pdf`.

[8] The Royal Swedish Academy of Sciences. The nobel prize in chemistry: Conductive polymers (advanced information) (2000).

[9] H. Shirakawa, E. J. Louis, A. G. MacDiarmid, C. K. Chiang, and A. J. Heeger. Synthesis of electrically conducting organic polymers: halogen derivatives of polyacetylene, $(CH)_x$. *J. Chem. Soc., Chem. Commun.*, **0**, 578–580 (1977). `doi:10.1039/C39770000578`.

[10] M. S. Freund and B. A. Deore. *Self-doped conducting polymers*. Wiley, Chichester (2007).

[11] W. Demtröder. *Atoms, molecules and photons : an introduction to atomic-, molecular- and quantum-physics*. Springer, Berlin (2006).

[12] W. H. Brütting, editor. *Physics of organic semiconductors*. Wiley-VCH, Weinheim (2005).

[13] B. A. Gregg and M. C. Hanna. Comparing organic to inorganic photovoltaic cells: Theory, experiment, and simulation. *Journal of Applied Physics*, **93**(6), 3605–3614 (2003). doi:10.1063/1.1544413.

[14] J. D. Servaites, M. A. Ratner, and T. J. Marks. Organic solar cells: A new look at traditional models. *Energy Environ. Sci.*, **4**, 4410–4422 (2011). doi:10.1039/C1EE01663F.

[15] I. Hill, A. Kahn, Z. Soos, R. Pascal, and Jr. Charge-separation energy in films of π-conjugated organic molecules. *Chemical Physics Letters*, **327**(3-4), 181–188 (2000). doi:10.1016/S0009-2614(00)00882-4.

[16] P. Peumans, A. Yakimov, and S. R. Forrest. Small molecular weight organic thin-film photodetectors and solar cells. *Journal of Applied Physics*, **93**(7), 3693–3723 (2003). doi:10.1063/1.1534621.

[17] H. Spanggaard and F. C. Krebs. A brief history of the development of organic and polymeric photovoltaics. *Solar Energy Materials and Solar Cells*, **83**(2-3), 125–146 (2004). doi:10.1016/j.solmat.2004.02.021.

[18] A. Colsmann. *Ladungstransportschichten für effiziente organische Halbleiterbauelemente*. Universitätsverlag, Karlsruhe (2009). ISBN: 978-3-86644-332-7.

[19] A. W. Hains, Z. Liang, M. A. Woodhouse, and B. A. Gregg. Molecular semiconductors in organic photovoltaic cells. *Chemical Reviews*, **110**(11), 6689–6735 (2010). doi:10.1021/cr9002984.

[20] L.-M. Chen, Z. Hong, G. Li, and Y. Yang. Recent progress in polymer solar cells: Manipulation of polymer:fullerene morphology and the formation of efficient inverted polymer solar cells. *Advanced Materials*, **21**(14-15), 1434–1449 (2009). doi:10.1002/adma.200802854.

[21] S. H. Park, A. Roy, S. Beaupré, S. Cho, N. Coates, J. S. Moon, D. Moses, M. Leclerc, K. Lee, and A. J. Heeger. Bulk heterojunction solar cells with internal quantum efficiency approaching 100 %. *Nature Photonics*, **3**(5), 297–302 (2009). doi:10.1038/nphoton.2009.69.

[22] C. J. Brabec, A. Cravino, D. Meissner, N. S. Sariciftci, T. Fromherz, M. T. Rispens, L. Sanchez, and J. C. Hummelen. Origin of the open circuit voltage of plastic solar cells. *Advanced Functional Materials*, **11**(5), 374–380 (2001). doi:10.1002/1616-3028(200110)11:5<374::AID-ADFM374>3.0.CO;2-W.

[23] C. Winder and N. S. Sariciftci. Low bandgap polymers for photon harvesting in bulk heterojunction solar cells. *J. Mater. Chem.*, **14**, 1077–1086 (2004). doi:10.1039/B306630D.

[24] P. Würfel. *Physics of solar cells, from principles to new concepts*. Wiley-VCH, Weinheim, Germany (2005). ISBN: 3-527-40428-7.

[25] C. Riordan and R. Hulstron. What is an air mass 1.5 spectrum? (solar cell performance calculations). In *Photovoltaic Specialists Conference, 1990., Conference Record of the Twenty First IEEE*, pages 1085–1088 vol.2 (1990). doi:10.1109/PVSC.1990.111784.

[26] A. Marrocchi, D. Lanari, A. Facchetti, and L. Vaccaro. Poly(3-hexylthiophene): synthetic methodologies and properties in bulk heterojunction solar cells. *Energy Environ. Sci.*, **5**, 8457–8474 (2012). doi:10.1039/C2EE22129B.

[27] W. L. Ma, C. Y. Yang, X. Gong, K. Lee, and A. J. Heeger. Thermally stable, efficient polymer solar cells with nanoscale control of the interpenetrating network morphology. *Advanced Functional Materials*, **15**(10), 1617–1622 (2005). doi:10.1002/adfm.200500211.

[28] Y. Kim, S. Cook, S. M. Tuladhar, S. A. Choulis, J. Nelson, J. R. Durrant, D. D. Bradley, M. Giles, I. McCulloch, C.-S. Ha, et al. A strong regioregularity effect in self-organizing conjugated polymer films and high-efficiency polythiophene: fullerene solar cells. *Nature Materials*, **5**(3), 197–203 (2006). doi:10.1038/nmat1574.

[29] M. Heeney, W. Zhang, D. J. Crouch, M. L. Chabinyc, S. Gordeyev, R. Hamilton, S. J. Higgins, I. McCulloch, P. J. Skabara, D. Sparrowe, and S. Tierney. Regioregular poly(3-hexyl)selenophene: a low band gap organic hole transporting polymer. *Chem. Commun.*, **0**, 5061–5063 (2007). doi:10.1039/B712398A.

[30] A. M. Ballantyne, L. Chen, J. Nelson, D. D. C. Bradley, Y. Astuti, A. Maurano, C. G. Shuttle, J. R. Durrant, M. Heeney, W. Duffy, and I. McCulloch. Studies of highly regioregular poly(3-hexylselenophene) for photovoltaic applications. *Advanced Materials*, **19**(24), 4544–4547 (2007). doi:10.1002/adma.200701265.

[31] F. M. Pasker, S. M. Le Blanc, G. Schnakenburg, and S. Höger. Thiophene-2-aryl-2h-benzotriazole-thiophene oligomers with adjustable electronic properties. *Organic Letters*, **13**(9), 2338–2341 (2011). doi:10.1021/ol2005853.

[32] L. Bian, E. Zhu, J. Tang, W. Tang, and F. Zhang. Recent progress in the design of narrow bandgap conjugated polymers for high-efficiency organic solar cells. *Progress in Polymer Science*, **37**(9), 1292 – 1331 (2012). doi:10.1016/j.progpolymsci.2012.03.001.

[33] M. F. G. Klein, F. M. Pasker, S. Kowarik, D. Landerer, M. Pfaff, M. Isen, D. Gerthsen, U. Lemmer, S. Höger, and A. Colsmann. Carbazole-phenylbenzotriazole copolymers as absorber material in organic solar cells. *Macromolecules*, **46**(10), 3870–3878 (2013). accepted. doi:10.1021/ma400440q.

[34] H. Hoppe and N. S. Sariciftci. Organic solar cells: An overview. *Journal of Materials Research*, **19**, 1924–1945 (2004). doi:10.1557/JMR.2004.0252.

[35] W. W. H. Wong, T. B. Singh, D. Vak, W. Pisula, C. Yan, X. Feng, E. L. Williams, K. L. Chan, Q. Mao, D. J. Jones, C.-Q. Ma, K. Müllen, P. Bäuerle, and A. B. Holmes. Solution processable fluorenyl hexa-peri-hexabenzocoronenes in organic field-effect transistors and solar cells. *Advanced Functional Materials*, **20**(6), 927–938 (2010). doi:10.1002/adfm.200901827.

[36] L. Schmidt-Mende, A. Fechtenkötter, K. Müllen, E. Moons, R. H. Friend, and J. D. MacKenzie. Self-organized discotic liquid crystals for high-efficiency organic photovoltaics. *Science*, **293**(5532), 1119–1122 (2001). doi:10.1126/science.293.5532.1119.

[37] T. B. Singh, X. Chen, W. W. H. Wong, T. Ehlig, P. Kemppinen, M. Chen, S. E. Watkins, K. N. Winzenberg, S. Holdcroft, D. J. Jones, and A. B. Holmes. Correlation of charge extraction properties and short circuit current in various organic binary and ternary blend photovoltaic devices. *Applied Physics A*, **108**(3), 515–520 (2012). doi:10.1007/s00339-012-7028-x.

[38] D. F. Kronholm and J. C. Hummelen. *Organic photovoltaics, materials device physics and manufacturing technologies*, chapter 5: Fullerene-based acceptor materials, pages 155–178. Wiley-VHC (2008). ISBN: 978-3-527-31675-5.

[39] B. Kraabel, D. McBranch, N. S. Sariciftci, D. Moses, and A. J. Heeger. Ultrafast spectroscopic studies of photoinduced electron transfer from semiconducting polymers to C_{60}. *Phys. Rev. B*, **50**, 18543–18552 (1994). doi:10.1103/PhysRevB.50.18543.

[40] E. von Hauff, V. Dyakonov, and J. Parisi. Study of field effect mobility in PCBM films and P3HT:PCBM blends. *Solar Energy Materials and Solar Cells*, **87**(1-4), 149–156 (2005). doi:10.1016/j.solmat.2004.06.014.

[41] J. C. Hummelen, B. W. Knight, F. LePeq, F. Wudl, J. Yao, and C. L. Wilkins. Preparation and characterization of fulleroid and methanofullerene derivatives. *The Journal of Organic Chemistry*, **60**(3), 532–538 (1995). doi:10.1021/jo00108a012.

[42] C. Liu, S. Xiao, X. Shu, Y. Li, L. Xu, T. Liu, Y. Yu, L. Zhang, H. Liu, and Y. Li. Synthesis and photovoltaic properties of novel monoadducts and bisadducts based on amide methanofullerene. *ACS Applied Materials & Interfaces*, **4**(2), 1065–1071 (2012). doi:10.1021/am2016975.

[43] J. Min, Z.-G. Zhang, M. Zhang, and Y. Li. Synthesis and photovoltaic properties of a d-a copolymer of dithienosilole and fluorinated-benzotriazole. *Polym. Chem.*, **4**, 1467–1473 (2013). doi:10.1039/C2PY20982A.

[44] E. Meijer, D. De Leeuw, S. Setayesh, E. Van Veenendaal, B.-H. Huisman, P. Blom, J. Hummelen, U. Scherf, and T. Klapwijk. Solution-processed ambipolar organic field-effect transistors and inverters. *Nature materials*, **2**(10), 678–682 (2003). doi:10.1038/nmat978.

[45] P. Boland, K. Lee, and G. Namkoong. Device optimization in PCPDTBT:PCBM plastic solar cells. *Solar Energy Materials and Solar Cells*, **94**(5), 915–920 (2010). doi:10.1016/j.solmat.2010.01.022.

[46] M. M. Wienk, J. M. Kroon, W. J. H. Verhees, J. Knol, J. C. Hummelen, P. A. van Hal, and R. A. J. Janssen. Efficient methano[70]fullerene/MDMO-PPV bulk heterojunction photovoltaic cells. *Angewandte Chemie*, **115**(29), 3493–3497 (2003). doi:10.1002/ange.200351647.

[47] M. Fahland. *Organic photovoltaics, materials device physics and manufacturing technologies*, chapter 15: Reel-to-Reel Processing of highly conductive metal oxides, pages 425–439. Wiley-VHC (2008). ISBN: 978-3-527-31675-5.

[48] A. Elschner and S. Kirchmeyer. *Organic photovoltaics, materials device physics and manufacturing technologies*, chapter 7: PEDOT-type materialy in organic solar cells, pages 213–242. Wiley-VHC (2008). ISBN: 978-3-527-31675-5.

[49] L. Groenendaal, F. Jonas, D. Freitag, H. Pielartzik, and J. R. Reynolds. Poly(3,4-ethylenedioxythiophene) and its derivatives: Past, present, and future. *Advanced Materials*, **12**(7), 481–494 (2000). doi:10.1002/(SICI)1521-4095(200004)12:7<481::AID-ADMA481>3.0.CO;2-C.

[50] A. R. bin Mohd Yusoff, H. P. Kim, and J. Jang. Inverted organic solar cells with tiox cathode and graphene oxide anode buffer layers. *Solar Energy Materials and Solar Cells*, **109**(0), 63 – 69 (2013). doi:10.1016/j.solmat.2012.09.032.

[51] Y. Sun, C. J. Takacs, S. R. Cowan, J. H. Seo, X. Gong, A. Roy, and A. J. Heeger. Efficient, air-stable bulk heterojunction polymer solar cells using MoOx as the anode interfacial layer. *Advanced Materials*, **23**(19), 2226–2230 (2011). doi:10.1002/adma.201100038.

[52] J. Subbiah, C. M. Amb, J. R. Reynolds, and F. So. Effect of vertical morphology on the performance of silole-containing low-bandgap inverted polymer solar cells. *Solar Energy Materials and Solar Cells*, **97**(0), 97 – 101 (2012). doi:10.1016/j.solmat.2011.09.028.

[53] A. J. Pearson, T. Wang, and D. G. Lidzey. The role of dynamic measurements in correlating structure with optoelectronic properties in polymer:fullerene bulk-heterojunction solar cells. *Reports on Progress in Physics*, **76**(2), 022501 (2013). doi:10.1088/0034-4885/76/2/022501.

[54] A. Haugeneder, M. Neges, C. Kallinger, W. Spirkl, U. Lemmer, J. Feldmann, U. Scherf, E. Harth, A. Gügel, and K. Müllen. Exciton diffusion and dissociation in conjugated polymer/fullerene blends and heterostructures. *Phys. Rev. B*, **59**, 15346–15351 (1999). doi:10.1103/PhysRevB.59.15346.

[55] S. Cataldo and B. Pignataro. Polymeric thin films for organic electronics: Properties and adaptive structures. *Materials*, **6**(3), 1159–1190 (2013). doi:10.3390/ma6031159.

[56] A. Pivrikas, H. Neugebauer, and N. S. Sariciftci. Influence of processing additives to nano-morphology and efficiency of bulk-heterojunction solar cells: A comparative review. *Solar Energy*, **85**(6), 1226–1237 (2011). doi:10.1016/j.solener.2010.10.012.

[57] S. E. Shaheen, C. J. Brabec, N. S. Sariciftci, F. Padinger, T. Fromherz, and J. C. Hummelen. 2.5% efficient organic plastic solar cells. *Applied Physics Letters*, **78**(6), 841–843 (2001). doi:10.1063/1.1345834.

[58] G. Li, Y. Yao, H. Yang, V. Shrotriya, G. Yang, and Y. Yang. "Solvent annealing" effect in polymer solar cells based on poly(3-hexylthiophene) and methanofullerenes. *Advanced Functional Materials*, **17**(10), 1636–1644 (2007). doi:10.1002/adfm.200600624.

[59] A. J. Moulé and K. Meerholz. Morphology control in solution-processed bulk-heterojunction solar cell mixtures. *Advanced Functional Materials*, **19**(19), 3028–3036 (2009). doi:10.1002/adfm.200900775.

[60] B. Tieke. *Makromolekulare Chemie: eine Einführung*. WILEY-VCH, Weinheim, 2nd edition (2005). ISBN: 3-527-31379-6.

[61] F. Liu, Y. Gu, J. W. Jung, W. H. Jo, and T. P. Russell. On the morphology of polymer-based photovoltaics. *Journal of Polymer Science Part B: Polymer Physics*, **50**(15), 1018–1044 (2012). doi:10.1002/polb.23063.

[62] J. K. Lee, W. L. Ma, C. J. Brabec, J. Yuen, J. S. Moon, J. Y. Kim, K. Lee, G. C. Bazan, and A. J. Heeger. Processing additives for improved efficiency from bulk heterojunction solar cells. *Journal of the American Chemical Society*, **130**(11), 3619–3623 (2008). doi:10.1021/ja710079w.

[63] G. Nagarjuna and D. Venkataraman. Strategies for controlling the active layer morphologies in OPVs. *Journal of Polymer Science Part B: Polymer Physics*, **50**(15), 1045–1056 (2012). doi:10.1002/polb.23073.

[64] S. J. Lou, J. M. Szarko, T. Xu, L. Yu, T. J. Marks, and L. X. Chen. Effects of additives on the morphology of solution phase aggregates formed by active layer components of high-efficiency organic solar cells. *Journal of the American Chemical Society*, **133**(51), 20661–20663 (2011). doi:10.1021/ja2085564.

[65] C. Müller, T. A. M. Ferenczi, M. Campoy-Quiles, J. M. Frost, D. D. C. Bradley, P. Smith, N. Stingelin-Stutzmann, and J. Nelson. Binary organic photovoltaic blends: A simple rationale for optimum compositions. *Advanced Materials*, **20**(18), 3510–3515 (2008). doi:10.1002/adma.200800963.

[66] C. Nicolet, D. Deribew, C. Renaud, G. Fleury, C. Brochon, E. Cloutet, L. Vignau, G. Wantz, H. Cramail, M. Geoghegan, and G. Hadziioannou. Optimization of the bulk heterojunction composition for enhanced photovoltaic properties: Correlation between the molecular weight of the semiconducting polymer and device performance. *Journal of Physical Chemistry B*, **115**(44), 12717–12727 (2011). doi:10.1021/jp207669j.

[67] R. C. Hiorns, R. de Bettignies, J. Leroy, S. Bailly, M. Firon, C. Sentein, A. Khoukh, H. Preud'homme, and C. Dagron-Lartigau. High molecular weights, polydispersities, and annealing temperatures in the optimization of bulk-heterojunction photovoltaic cells based on poly(3-hexylthiophene) or poly(3-butylthiophene). *Advanced Functional Materials*, **16**(17), 2263–2273 (2006). doi:10.1002/adfm.200600005.

[68] W. Ma, J. Y. Kim, K. Lee, and A. J. Heeger. Effect of the molecular weight of poly(3-hexylthiophene) on the morphology and performance of polymer bulk heterojunction solar cells. *Macromolecular Rapid Communications*, **28**(17), 1776–1780 (2007). doi:10.1002/marc.200700280.

[69] J.-M. Verilhac, G. LeBlevennec, D. Djurado, F. Rieutord, M. Chouiki, J.-P. Travers, and A. Pron. Effect of macromolecular parameters and processing conditions on supramolecular organisation, morphology and electrical transport properties in thin layers of regioregular poly(3-hexylthiophene). *Synthetic Metals*, **156**(11-13), 815–823 (2006). doi:10.1016/j.synthmet.2006.04.012.

[70] P. C. Ewbank, D. Laird, and R. D. McCullough. *Organic photovoltaics, materials device physics and manufacturing technologies*, chapter 1: Regioregular Polythiophene solar cells: material properties and performance, pages 1–55. Wiley-VHC (2008). ISBN: 978-3-527-31675-5.

[71] K. J. Ihn, J. Moulton, and P. Smith. Whiskers of poly(3-alkylthiophene)s. *Journal of Polymer Science Part B: Polymer Physics*, **31**(6), 735–742 (1993). doi:10.1002/polb.1993.090310614.

[72] A. Swinnen, I. Haeldermans, P. Vanlaeke, J. D'Haen, J. Poortmans, M. D'Olieslaeger, and J. V. Manca. Dual crystallization behaviour of polythiophene/fullerene blends. *The European Physical Journal - Applied Physics*, **36**, 251–256 (2006). doi:10.1051/epjap:2006138.

[73] A. Swinnen, I. Haeldermans, M. vande Ven, J. D'Haen, G. Vanhoyland, S. Aresu, M. D'Olieslaeger, and J. Manca. Tuning the dimensions of C_{60}-based needlelike crystals in blended thin films. *Advanced Functional Materials*, **16**(6), 760–765 (2006). doi:10.1002/adfm.200500812.

[74] N. D. Treat, A. Varotto, C. J. Takacs, N. Batara, M. Al-Hashimi, M. J. Heeney, A. J. Heeger, F. Wudl, C. J. Hawker, and M. L. Chabinyc. Polymer-fullerene miscibility: A metric for screening new materials for high-performance organic solar cells. *Journal of the American Chemical Society*, **134**(38), 15869–15879 (2012). doi:10.1021/ja305875u.

[75] A. M. Ballantyne, T. A. M. Ferenczi, M. Campoy-Quiles, T. M. Clarke, A. Maurano, K. H. Wong, W. Zhang, N. Stingelin-Stutzmann, J.-S. Kim, D. D. C. Bradley, J. R. Durrant, I. McCulloch, M. Heeney, J. Nelson, S. Tierney, W. Duffy, C. Mueller, and P. Smith. Understanding the influence of morphology on poly(3-hexylselenothiophene):PCBM solar cells. *Macromolecules*, **43**(3), 1169–1174 (2010). doi:10.1021/ma902477h.

[76] S. Lilliu, T. Agostinelli, E. Verploegen, E. Pires, M. Hampton, M. Al-Hashimi, M. J. Heeney, M. F. Toney, J. Nelson, and J. E. Macdonald. Effects of thermal annealing upon the nanomorphology of poly(3-hexylselenophene)-PCBM blends. *Macromolecular Rapid Communications*, **32**(18), 1454–1460 (2011). doi:10.1002/marc.201100330.

[77] W. C. Tsoi, D. T. James, E. B. Domingo, J. S. Kim, M. Al-Hashimi, C. E. Murphy, N. Stingelin, M. Heeney, and J.-S. Kim. Effects of a heavy atom on molecular order and morphology in conjugated polymer:fullerene photovoltaic blend thin films and devices. *ACS Nano*, **6**(11), 9646–9656 (2012). doi:10.1021/nn304024g.

[78] W. W. H. Wong, C.-Q. Ma, W. Pisula, A. Mavrinskiy, X. Feng, H. Seyler, D. J. Jones, K. Müllen, P. Bäuerle, and A. B. Holmes. Fluorenyl hexa-peri-hexabenzocoronene-dendritic oligothiophene hybrid materials: Synthesis, photophysical properties, self-association behaviour and device performance. *Chemistry - A European Journal*, **17**(20), 5549–5560 (2011). doi:10.1002/chem.201100211.

[79] G. H. Michler. *Electron Microscopy of Polymers*. Springer, Berlin, Heidelberg (2008). ISBN: 978-3-540-36350-7. doi:10.1007/978-3-540-36352-1.

[80] FEI Company. *Strata 400 (STEM) User's manual* (2007).

[81] C.-S. Kim, S.-H. Ahn, and D.-Y. Jang. Review: Developments in micro/nanoscale fabrication by focused ion beams. *Vacuum*, **86**(8), 1014 – 1035 (2012). doi:10.1016/j.vacuum.2011.11.004.

[82] J. Orloff, L. Swanson, and M. Utlaut. *High resolution focused Ion beams, FIB and its apllications*. Kluwer academic / Plenum publisher, New York (2003). ISBN: 0-306-47350-X.

[83] F. A. Stevie, L. A. Giannuzzi, and B. I. Prenitzer. *Introduction to focused ion beams - Instrumentation, Theory, Techniques and practice*, chapter 1: The focused ion beam instrument, pages 1–12. Springer (2005). ISBN: 0-387-23116-1.

[84] L. Reimer. *Scanning Electron Microscopy, Physics of Image Formation an Microanalysis*. Springer, 2nd edition (1985).

[85] L. C. Sawyer and D. T. Grubb. *Polymer Microscopy*. Chapman & Hall (1996). ISBN: 0-412-60490-6.

[86] H. Kazumori, K. Honda, M. Matsuya, M. Date, and C. Nielsen. Field emission SEM with a spherical and chromatic aberration corrector. *Microscopy and Microanalysis*, **10**, 1370–1371 (2004). doi:10.1017/S1431927604881352.

[87] T. Klein, E. Buhr, and C. G. Frase. Chapter 6 - TSEM: A review of scanning electron microscopy in transmission mode and its applications. P. W. Hawkes, editor, *Advances in Imaging and Electron Physics*, volume 171 of *Advances in Imaging and Electron Physics*, pages 297 – 356. Elsevier (2012). doi:10.1016/B978-0-12-394297-5.00006-4.

[88] J. Liu. Scanning transmission electron microscopy and its application to the study of nanoparticles and nanoparticle systems. *Journal of Electron Microscopy*, **54**(3), 251–278 (2005). doi:10.1093/jmicro/dfi034.

[89] P. Hartel, H. Rose, and C. Dinges. Conditions and reasons for incoherent imaging in STEM. *Ultramicroscopy*, **63**(2), 93 – 114 (1996). doi:10.1016/0304-3991(96)00020-4.

[90] S. Pennycook and L. Boatner. Chemically sensitive structure-imaging with a scanning transmission electron microscope. *Nature*, **336**(6199), 565–567 (1988). doi:10.1038/336565a0.

[91] B. Borries and E. Ruska. Der Einfluß der Strahlspannung auf das übermikroskopische Bild. *Zeitschrift für Physik A Hadrons and Nuclei*, **116**, 249–256 (1940). doi:10.1007/BF01337389.

[92] A. Delong. Low voltage electron microscope. In *EUREM conference papers* (2000).

[93] J. Wall, J. Langmore, M. Isaacson, and A. V. Crewe. Scanning transmission electron microscopy at high resolution. *Proceedings of the National Academy of Sciences*, **71**(1), 1–5 (1974).

[94] F. Lednický, E. Coufalová, J. Hromádková, A. Delong, and V. Kolařik. Low-voltage TEM imaging of polymer blends. *Polymer*, **41**(13), 4909 – 4914 (2000). doi:10.1016/S0032-3861(99)00711-9.

[95] S. J. Williams, D. E. Morrison, B. L. Thiel, and A. M. Donald. Imaging of semiconducting polymer blend systems using environmental scanning electron microscopy and environmental scanning transmission electron microscopy. *Scanning*, **27**(4), 190–198 (2005). doi:10.1002/sca.4950270406.

[96] J. Faucheu, L. Chazeau, C. Gauthier, J.-Y. Cavaillé, M. Goikoetxea, R. Minari, and J. M. Asua. Latex imaging by environmental STEM: Application to the study of the surfactant outcome in hybrid alkyd/acrylate systems. *Langmuir*, **25**(17), 10251–10258 (2009). doi:10.1021/la901049h.

[97] O. Guise, C. Strom, and N. Preschilla. STEM-in-SEM method for morphology analysis of polymer systems. *Polymer*, **52**(5), 1278 – 1285 (2011). doi:10.1016/j.polymer.2011.01.030.

[98] P. G. Merli, F. Corticelli, and V. Morandi. Images of dopant profiles in low-energy scanning transmission electron microscopy. *Applied Physics Letters*, **81**(24), 4535–4537 (2002). doi:10.1063/1.1528734.

[99] P. G. Merli and V. Morandi. Low-energy STEM of multilayers and dopant profiles. *Microscopy and Microanalysis*, **11**, 97–104 (2005). doi:10.1017/S1431927605050063.

[100] V. Morandi and P. G. Merli. Contrast and resolution versus specimen thickness in low energy scanning transmission electron microscopy. *Journal of Applied Physics*, **101**(11), 114917 (2007). doi:10.1063/1.2745333.

[101] T. Volkenandt, E. Müller, D. Hu, D. Schaadt, and D. Gerthsen. Quantification of sample thickness and In-concentration of InGaAs quantum wells by transmission measurements in a scanning electron microscope. *Microscopy and Microanalysis*, **16**, 604–613 (2010). doi:10.1017/S1431927610000292.

[102] S. J. Pennycook and P. P. D. Nellist. *Scanning transmission electron microscopy*. Springer (2011). ISBN: 978-1441971999.

[103] J. Loos, E. Sourty, K. Lu, G. de With, and S. v. Bavel. Imaging polymer systems with high-angle annular dark field scanning transmission electron microscopy (HAADF-STEM). *Macromolecules*, **42**(7), 2581–2586 (2009). doi:10.1021/ma8026589.

[104] E. Sourty, S. van Bavel, K. Lu, R. Guerra, G. Bar, and J. Loos. High-angle annular dark field scanning transmission electron microscopy on carbon-based functional polymer systems. *Microscopy and Microanalysis*, **15**, 251–258 (2009). doi:10.1017/S1431927609090278.

[105] L. Reimer and H. Kohl. *Transmission electron microscopy : physics of image formation*. Springer series in optical sciences ; 36. Springer, New York, 5. ed. edition (2008).

[106] D. B. Williams and C. B. Carter. *Transmission Electron Microscopy - A textbook for Materials Science*. Springer, 2nd edition (2009).

[107] L. F. Drummy and C. Kübel. Polymer microscopy: Current challenges. *Polymer Reviews*, **50**(3), 231–234 (2010). doi:10.1080/15583724.2010.493625.

[108] L. F. Drummy, J. Yang, and D. C. Martin. Low-voltage electron microscopy of polymer and organic molecular thin films. *Ultramicroscopy*, **99**(4), 247 – 256 (2004). doi:10.1016/j.ultramic.2004.01.011.

[109] D. L. Handlin and E. L. Thomas. Phase contrast imaging of styrene-isoprene and styrene-butadiene block copolymers. *Macromolecules*, **16**(9), 1514–1525 (1983). doi:10.1021/ma00243a019.

[110] T. J. Savenije, J. E. Kroeze, X. Yang, and J. Loos. The formation of crystalline P3HT fibrils upon annealing of a PCBM:P3HT bulk heterojunction. *Thin Solid Films*, **511-512**, 2–6 (2006). doi:10.1016/j.tsf.2005.12.123.

[111] P. Vanlaeke, A. Swinnen, I. Haeldermans, G. Vanhoyland, T. Aernouts, D. Cheyns, C. Deibel, J. D'Haen, P. Heremans, J. Poortmans, and J. V. Manca. P3HT/PCBM bulk heterojunction solar cells: Relation between morphology and electro-optical characteristics. *Solar Energy Materials and Solar Cells*, **90**(14), 2150–2158 (2006). doi:10.1016/j.solmat.2006.02.010.

[112] C. Lin, E.-Y. Lin, and F.-Y. Tsai. Enhanced thermal stability and efficiency of polymer bulk-heterojunction solar cells by low-temperature drying of the active layer. *Advanced Functional Materials*, **20**(5), 834–839 (2010). doi:10.1002/adfm.200901807.

[113] J. W. Jung and W. H. Jo. Annealing-free high efficiency and large area polymer solar cells fabricated by a roller painting process. *Advanced Functional Materials*, **20**(14), 2355–2363 (2010). doi:10.1002/adfm.201000164.

[114] S. Bertho, W. D. Oosterbaan, V. Vrindts, J. D'Haen, T. J. Cleij, L. Lutsen, J. Manca, and D. Vanderzande. Controlling the morphology of nanofiber-P3HT:PCBM blends for organic bulk heterojunction solar cells. *Organic Electronics*, **10**(7), 1248 – 1251 (2009). doi:10.1016/j.orgel.2009.06.018.

[115] J. Petermann, H. Moritz, U. Rieck, B. Wood, and E. Thomas. A novel TEM dark-field contrast method for semi-crystalline polymers. *Journal of Materials Science Letters*, **8**(9), 1023–1025 (1989). doi:10.1007/BF01730475.

[116] X. Zhang, S. D. Hudson, D. M. DeLongchamp, D. J. Gundlach, M. Heeney, and I. McCulloch. In-plane liquid crystalline texture of high-performance thienothiophene copolymer thin films. *Advanced Functional Materials*, **20**(23), 4098–4106 (2010). doi:10.1002/adfm.201001232.

[117] X. Zhang, L. J. Richter, D. M. DeLongchamp, R. J. Kline, M. R. Hammond, I. McCulloch, M. Heeney, R. S. Ashraf, J. N. Smith, T. D. Anthopoulos, B. Schroeder, Y. H. Geerts, D. A. Fischer, and M. F. Toney. Molecular packing of high-mobility diketo pyrrolo-pyrrole polymer semiconductors with branched alkyl side chains. *Journal of the American Chemical Society*, **133**(38), 15073–15084 (2011). doi:10.1021/ja204515s.

[118] M. Brinkmann, C. Contal, N. Kayunkid, T. Djuric, and R. Resel. Highly oriented and nanotextured films of regioregular poly(3-hexylthiophene) grown by epitaxy on the nanostructured surface of an aromatic substrate. *Macromolecules*, **43**(18), 7604–7610 (2010). doi:10.1021/ma101313m.

[119] X. Yang, J. Loos, S. C. Veenstra, W. J. H. Verhees, M. M. Wienk, J. M. Kroon, M. A. J. Michels, and R. A. J. Janssen. Nanoscale morphology of high-performance polymer solar cells. *Nano Letters*, **5**(4), 579–583 (2005). doi:10.1021/nl048120i.

[120] B. J. Campo, D. Bevk, J. Kesters, J. Gilot, H. J. Bolink, J. Zhao, J.-C. Bolsée, W. D. Oosterbaan, S. Bertho, J. D'Haen, J. Manca, L. Lutsen, G. V. Assche, W. Maes, R. A. Janssen, and D. Vanderzande. Ester-functionalized poly(3-alkylthiophene) copolymers: Synthesis, physicochemical characterization and performance in bulk heterojunction organic solar cells. *Organic Electronics*, **14**(2), 523 – 534 (2013). doi:10.1016/j.orgel.2012.11.021.

[121] T. Heiser, G. Adamopoulos, M. Brinkmann, U. Giovanella, S. Ould-Saad, C. Brochon, K. van de Wetering, and G. Hadziioannou. Nanostructure of self-assembled rod-coil block copolymer films for photovoltaic applications. *Thin Solid Films*, **511-512**(0), 219 – 223 (2006). doi:10.1016/j.tsf.2005.12.134.

[122] D. C. Martin, J. Chen, J. Yang, L. F. Drummy, and C. Kübel. High resolution electron microscopy of ordered polymers and organic molecular crystals: Recent developments and future possibilities. *Journal of Polymer Science Part B: Polymer Physics*, **43**(14), 1749–1778 (2005). doi:10.1002/polb.20419.

[123] G. Kalita, M. Masahiro, W. Koichi, and M. Umeno. Nanostructured morphology of P3HT:PCBM bulk heterojunction solar cells. *Solid-State Electronics*, **54**(4), 447 – 451 (2010). doi:10.1016/j.sse.2009.11.010.

[124] M. Reyes-Reyes, R. López-Sandoval, J. Arenas-Alatorre, R. Garibay-Alonso, D. Carroll, and A. Lastras-Martinez. Methanofullerene elongated nanostructure formation for enhanced organic solar cells. *Thin Solid Films*, **516**(1), 52 – 57 (2007). doi:10.1016/j.tsf.2007.04.166.

[125] L. F. Drummy, R. J. Davis, D. L. Moore, M. Durstock, R. A. Vaia, and J. W. P. Hsu. Molecular-scale and nanoscale morphology of P3HT:PCBM bulk heterojunctions: Energy-filtered TEM and low-dose HREM . *Chemistry of Materials*, **23**(3), 907–912 (2011). doi:10.1021/cm102463t.

[126] A. Du Chesne. Energy filtering transmission electron microscopy of polymers - benefit and limitations of the method. *Macromolecular Chemistry and Physics*, **200**(8), 1813–1830 (1999). doi:10.1002/(SICI)1521-3935(19990801)200:8<1813::AID-MACP1813>3.0.CO;2-N.

[127] D. R. Kozub, K. Vakhshouri, L. M. Orme, C. Wang, A. Hexemer, and E. D. Gomez. Polymer crystallization of partially miscible polythiophene/fullerene mixtures controls morphology. *Macromolecules*, **44**(14), 5722–5726 (2011). doi:10.1021/ma200855r.

[128] A. A. Herzing, L. J. Richter, and I. M. Anderson. 3D nanoscale characterization of thin-film organic photovoltaic device structures via spectroscopic contrast in the TEM. *The Journal of Physical Chemistry C*, **114**(41), 17501–17508 (2010). doi:10.1021/jp105883p.

[129] M. Pfannmöller, H. Flügge, G. Benner, I. Wacker, C. Sommer, M. Hanselmann, S. Schmale, H. Schmidt, F. A. Hamprecht, T. Rabe, W. Kowalsky, and R. R. Schröder. Visualizing a homogeneous blend in bulk heterojunction polymer solar cells by analytical electron microscopy. *Nano Letters*, **11**(8), 3099–3107 (2011). arXiv:http://pubs.acs.org/doi/pdf/10.1021/nl201078t, doi:10.1021/nl201078t.

[130] J. A. Amonoo, E. Glynos, X. C. Chen, and P. F. Green. An alternative processing strategy for organic photovoltaic devices using a supercritical fluid. *The Journal of Physical Chemistry C*, **116**(39), 20708–20716 (2012). doi:10.1021/jp304976x.

[131] W. Schindler, M. Wollgarten, and K. Fostiropoulos. Revealing nanoscale phase separation in small-molecule photovoltaic blends by plasmonic contrast in the TEM. *Organic Electronics*, **13**(6), 1100 – 1104 (2012). doi:10.1016/j.orgel.2012.03.008.

[132] S. S. van Bavel and J. Loos. Volume organization of polymer and hybrid solar cells as revealed by electron tomography. *Advanced Functional Materials*, **20**(19), 3217–3234 (2010). doi:10.1002/adfm.201000745.

[133] R. Leary, P. A. Midgley, and J. M. Thomas. Recent advances in the application of electron tomography to materials chemistry. *Accounts of Chemical Research*, **45**(10), 1782–1791 (2012). doi:10.1021/ar3001102.

[134] P. W. Hawkes. The electron microscope as a structure projector. J. Frank, editor, *Electron Tomography, Three-dimensional imaging with the transmission electron microscope*, pages 17–38. Plenum Press (1992). ISBN: 0-306-43995-6.

[135] K. Lu, E. Sourty, R. Guerra, G. Bar, and J. Loos. Critical comparison of volume data obtained by different electron tomography techniques. *Macromolecules*, **43**(3), 1444–1448 (2010). doi:10.1021/ma901998r.

[136] P. Gilbert. Iterative methods for the three-dimensional reconstruction of an object from projections. *Journal of Theoretical Biology*, **36**(1), 105–117 (1972). doi:10.1016/0022-5193(72)90180-4.

[137] M. Radermacher. Weighted back-projection methods. J. Frank, editor, *Electron Tomography, Three-dimensional imaging with the transmission electron microscope*, pages 91–115. Plenum Press (1992). ISBN: 0-306-43995-6.

[138] R. H. M. Schoenmakers, R. A. Perquin, T. F. Fliervoet, and W. Voorhout. High resolution, high throughput electron tomography reconstruction. *Microscopy and Microanalysis*, **11**, 312–313 (2005). doi:10.1017/S1431927605506330.

[139] S. S. van Bavel, E. Sourty, G. d. With, and J. Loos. Three-dimensional nanoscale organization of bulk heterojunction polymer solar cells. *Nano Letters*, **9**(2), 507–513 (2009). doi:10.1021/nl8014022.

[140] S. van Bavel, E. Sourty, G. de With, K. Frolic, and J. Loos. Relation between photoactive layer thickness, 3D morphology, and device performance in P3HT/PCBM bulk-heterojunction solar cells. *Macromolecules*, **42**(19), 7396–7403 (2009). doi:10.1021/ma900817t.

[141] S. S. van Bavel, M. Bärenklau, G. de With, H. Hoppe, and J. Loos. P3HT/PCBM bulk heterojunction solar cells: Impact of blend composition and 3D morphology on device performance. *Advanced Functional Materials*, **20**(9), 1458–1463 (2010). doi:10.1002/adfm.200902247.

[142] S. van Bavel, E. Sourty, G. de With, S. Veenstra, and J. Loos. Three-dimensional nanoscale organization of polymer solar cells. *J. Mater. Chem.*, **19**, 5388–5393 (2009). doi:10.1039/B900901A.

[143] H. Azimi, D. Fournier, M. Wirix, E. Dobrocka, T. Ameri, F. Machui, S. Rodman, G. Dennler, M. C. Scharber, K. Hingerl, J. Loos, C. J. Brabec, and M. Morana. Nano-morphology characterization of organic bulk heterojunctions based on mono and bis-adduct fullerenes. *Organic Electronics*, **13**(8), 1315 – 1321 (2012). doi:10.1016/j.orgel.2012.03.031.

[144] L. Hou, E. Wang, J. Bergqvist, B. V. Andersson, Z. Wang, C. Müller, M. Campoy-Quiles, M. R. Andersson, F. Zhang, and O. Inganäs. Lateral phase separation gradients in spin-coated thin films of high-performance polymer:fullerene photovoltaic blends. *Advanced Functional Materials*, **21**(16), 3169–3175 (2011). doi:10.1002/adfm.201100566.

[145] J. D. Roehling, K. J. Batenburg, F. B. Swain, A. J. Moulé, and I. Arslan. Three-dimensional concentration mapping of organic blends. *Advanced Functional Materials*, **23**(17), 2115–2122 (2013). doi:10.1002/adfm.201202190.

[146] F. Banhart. Irradiation effects in carbon nanostructures. *Reports on Progress in Physics*, **62**(8), 1181 (1999). doi:10.1088/0034-4885/62/8/201.

[147] R. Egerton, S. Lazar, and M. Libera. Delocalized radiation damage in polymers. *Micron*, **43**(1), 2 – 7 (2012). doi:10.1016/j.micron.2011.05.007.

[148] L. Reimer and M. Wächter. Contribution to the contamination problem in transmission electron microscopy. *Ultramicroscopy*, **3**(0), 169 – 174 (1978). doi:10.1016/S0304-3991(78)80023-0.

[149] P. Hirsch, M. Kässens, M. Püttmann, and L. Reimer. Contamination in a scanning electron microscope and the influence of specimen cooling. *Scanning*, **16**(2), 101–110 (1994). doi:10.1002/sca.4950160207.

[150] E. Rutherford. LXXIX. the scattering of α and β particles by matter and the structure of the atom. *Philosophical Magazine Series 6*, **21**(125), 669–688 (1911). doi:10.1080/14786440508637080.

[151] H. S. W. Mott, N.F. Massey. *The theory of atomic collisions*. Clarendon Press, 3rd edition (1965).

[152] R. Browning, T. Z. Li, B. Chui, J. Ye, R. F. W. Pease, Z. Czyzewski, and D. C. Joy. Low-energy electron/atom elastic scattering cross sections from 0.1-30 keV. *Scanning*, **17**(4), 250–253 (1995). doi:10.1002/sca.4950170406.

[153] R. Shimizu and D. Ze-Jun. Monte carlo modelling of electron-solid interactions. *Reports on Progress in Physics*, **55**(4), 487 (1992). doi:10.1088/0034-4885/55/4/002.

[154] Z. Czyżewski, D. O. MacCallum, A. Romig, and D. C. Joy. Calculations of Mott scattering cross section. *Journal of Applied Physics*, **68**(7), 3066 –3072 (1990). doi:10.1063/1.346400.

[155] C. Møller. Zur Theorie des Durchgangs schneller Elektronen durch Materie. *Annalen der Physik*, **406**(5), 531–585 (1932). doi:10.1002/andp.19324060506.

[156] S. Goudsmit and J. L. Saunderson. Multiple scattering of electrons. *Physical Review*, **57**, 24–29 (1940). doi:10.1103/PhysRev.57.24.

[157] C. Negreanu, X. Llovet, R. Chawla, and F. Salvat. Calculation of multiple-scattering angular distributions of electrons and positrons. *Radiation Physics and Chemistry*, **74**(5), 264 – 281 (2005). doi:10.1016/j.radphyschem.2005.07.006.

[158] V. E. Cosslett and R. N. Thomas. Multiple scattering of 5-30 keV electrons in evaporated metal films: I. total transmission and angular distribution. *British Journal of Applied Physics*, **15**(8), 883 (1964). doi:10.1088/0508-3443/15/8/303.

[159] W. Bothe. Durchgang von Elektronen durch Materie. W. Geiger, H. Bothe, editor, *Handbuch der Physik 22,2: Negative und positive Strahlen*, pages 1–74. Springer, Berlin (1933).

[160] J. A. Crowther. On the scattering of homogeneous β-rays and the number of electrons in the atom. *Proceedings of the Royal Society of London. Series A, Containing Papers of a Mathematical and Physical Character*, **84**(570), pp. 226–247 (1910).

[161] P. Merli, V. Morandi, and F. Corticelli. Backscattered electron imaging and scanning transmission electron microscopy imaging of multi-layers. *Ultramicroscopy*, **94**(2), 89 – 98 (2003). doi:10.1016/S0304-3991(02)00217-6.

[162] N. W. M. Ritchie. A new monte carlo application for complex sample geometries. *Surface and Interface Analysis*, **37**(11), 1006–1011 (2005). doi:10.1002/sia.2093.

[163] H. Bethe. Zur Theorie des Durchgangs schneller Korpuskularstrahlen durch Materie. *Annalen der Physik*, **397**(3), 325–400 (1930). doi:10.1002/andp.19303970303.

[164] D. C. Joy and S. Luo. An empirical stopping power relationship for low-energy electrons. *Scanning*, **11**(4), 176–180 (1989). doi:10.1002/sca.4950110404.

[165] R. Weast, editor. Chemical Rubber Company Handbook of Chemistry and Physics 59th edn. Taylor & Francis (1978).

[166] J. Mårdalen, E. Samuelsen, O. Gautun, and P. Carlsen. Chain configuration of poly(3-hexylthiophene) as revealed by detailed x-ray diffraction studies. *Solid State Communications*, **77**(5), 337 – 339 (1991). doi:10.1016/0038-1098(91)90745-H.

[167] L. F. Drummy, R. J. Davis, D. L. Moore, M. Durstock, R. A. Vaia, and J. W. P. Hsu. Molecular-scale and nanoscale morphology of P3HT:PCBM bulk heterojunctions: Energy-filtered TEM and low-dose HREM. *Chemistry of Materials*, **23**(3), 907–912 (2010). doi:10.1021/cm102463t.

[168] Ch. 03e1 standard tables for reference solar spectral irradiances: direct normal and hemispherical on 37° tilted surface (2006). doi:10.1520/G0173-03E01.

[169] W. C. Tsoi, S. J. Spencer, L. Yang, A. M. Ballantyne, P. G. Nicholson, A. Turnbull, A. G. Shard, C. E. Murphy, D. D. C. Bradley, J. Nelson, and J.-S. Kim. Effect of crystallization on the electronic energy levels and thin film morphology of P3HT:PCBM blends. *Macromolecules*, **44**(8), 2944–2952 (2011). doi:10.1021/ma102841e.

[170] M. F. G. Klein, M. Pfaff, E. Müller, J. Czolk, M. Reinhard, S. Valouch, U. Lemmer, A. Colsmann, and D. Gerthsen. Poly(3-hexylselenophene) solar cells: Correlating the optoelectronic device performance and nanomorphology imaged by low-energy scanning transmission electron microscopy. *Journal of Polymer Science Part B: Polymer Physics*, **50**(3), 198–206 (2012). doi:10.1002/polb.22394.

[171] N. S. Christ, S. W. Kettlitz, S. Valouch, S. Zufle, C. Gartner, M. Punke, and U. Lemmer. Nanosecond response of organic solar cells and photodetectors. *Journal of Applied Physics*, **105**(10), 104513 (2009). doi:10.1063/1.3130399.

[172] M. Isen. Dithienyl-2-aryl-2H-benzotriazol- und Carbazolderivate als Absorbermaterialien für Polymersolarzellen. Studienarbeit (student research project), Light technology institute, Karlsruhe Institute of Technology (KIT) (2011).

[173] D. Landerer. Untersuchung verschiedener Benzotriazol-Akzeptoren in Donor-Akzeptor-Copolymeren für die organische Photovoltaik. Bachelorthesis, Light Technology Institute, Karlsruhe Institute of Technology (KIT) (2012).

[174] B. Schmidt-Hansberg, M. F. G. Klein, M. Sanyal, F. Buss, G. Q. G. de Medeiros, C. Munuera, A. Vorobiev, A. Colsmann, P. Scharfer, U. Lemmer, E. Barrena, and W. Schabel. Structure formation in low-bandgap polymer:fullerene solar cell blends in the course of solvent evaporation. *Macromolecules*, **45**(19), 7948–7955 (2012). doi:10.1021/ma300945k.

[175] A. van de Craats, N. Stutzmann, O. Bunk, M. Nielsen, M. Watson, K. Müllen, H. Chanzy, H. Sirringhaus, and R. Friend. Meso-epitaxial solution-growth of self-organizing discotic liquid-crystalline semiconductors. *Advanced Materials*, **15**(6), 495–499 (2003). doi:10.1002/adma.200390114.

[176] M. A. Green, K. Emery, Y. Hishikawa, W. Warta, and E. D. Dunlop. Solar cell efficiency tables (version 41). *Progress in Photovoltaics: Research and Applications*, **21**(1), 1–11 (2013). doi:10.1002/pip.2352.

[177] R. F. Service. Outlook brightens for plastic solar cells. *Science*, **332**(6027), 293 (2011). doi:10.1126/science.332.6027.293.

[178] SALVE I-II, the low-voltage sub angstrom electron microscopy project. http://www.salve-project.de/home.html.

Own publications and contributions to conferences

Reviewed publications

- M. Pfaff, E. Müller, M. F. G. Klein, A. Colsmann, U. Lemmer, V. Krzyzanek, R. Reichelt and D. Gerthsen. Low-energy electron scattering in carbon-based materials analyzed by scanning transmission electron microscopy and its application to sample thickness determination. *Journal of Microscopy* **243**, 31-39 (2011). doi: 10.1111/j.1365-2818.2010.03475.x

- B. Schmidt-Hansberg, M. Sanyal, M. F. G. Klein, M. Pfaff, N. Schnabel, S. Jaiser, A. Vorobiev, E. Müller, A. Colsmann, P. Scharfer, D. Gerthsen, U. Lemmer, E. Barrena and W. Schabel. Moving through the Phase Diagram: Morphology Formation in Solution Cast Polymer-Fullerene Blend Films for Organic Solar Cells. *ACS Nano* **5**, 8579-8590 (2011). doi: 10.1021/nn2036279

- M. F. G. Klein, M. Pfaff, E. Müller, J. Czolk, M. Reinhard, S. Valouch, U. Lemmer, A. Colsmann and D. Gerthsen. Poly(3-hexylselenophene) solar cells: Correlating the optoelectronic device performance and nanomorphology imaged by low-energy scanning Transmission electron microscopy. *Journal of Polymer Science Part B: Polymer Physics* **50**, 198-206 (2012). doi: 10.1002/polb.22394

- M. Pfaff, M. F. G. Klein, E. Müller, P. Müller, A. Colsmann, U. Lemmer, and D. Gerthsen. Nanomorphology of P3HT:PCBM-based absorber layers of organic solar cells after different processing conditions analyzed by low-energy scanning transmission electron microscopy. *Microscopy & Microanalysis* **18**, 1380-1388 (2012). doi: 10.1017/S143192761201344X

- M. F. G. Klein, F. M. Pasker, S. Kowarik, D. Landerer, M. Pfaff, M. Isen, D. Gerthsen, U. Lemmer, S. Höger and A. Colsmann. Carbazole-phenylbenzotriazole copolymers as absorber material in organic solar cells. *Macromolecules* **46**, 3870-3878 (2013). doi: 10.1021/ma400440q.

- S. Höfle, H. Do, E. Mankel, M. Pfaff, Z. Zhang, D. Bahro, W. Jaegermann, D. Gerthsen, C. Feldmann, U. Lemmer and A. Colsmann. Molybdenum oxide anode buffer layers for solution processed, blue phosphorescent small molecule organic light emitting diodes. *Organic Electronics* **14**, 1820-1824 (2013). doi: 10.1016/j.orgel.2013.04.017

- M. Pfaff, P. Müller, P. Bockstaller, E. Müller, J. Subbiah, W. W. H. Wong, M. F. G. Klein, W. Pisula, A. Kiersnowski, S. R. Puniredd, W. Pisula, A. Colsmann, D. Gerthsen and D. J. Jones. Bulk heterojunction nanomorphology of fluorenyl hexa-*peri*-hexabenzocoronene-fullerene blend films. *ACS Applied Materials and Interfaces*, published online (2013) doi: 10.1021/am4044085.

- S. Höfle, M. Pfaff, H. Do, C. Bernhard, D. Gerthsen, U. Lemmer and Alexander Colsmann. Suppressing molecular aggregation in solution processed small molecule organic light emitting diodes. *Organic Electronics*, published online (2013) doi: 10.1016/j.orgel.2013.11.015.

Contributions to scientific conferences

- M. Pfaff, E. Müller, D. Gerthsen, M. F. G. Klein, A. Colsmann, U. Lemmer. Low-energy electron transmission measurements of thin polymer films in a scanning electron microscope. (Poster) *Microscopy Conference MC 2009*, Graz, Austria, August 30-September 4 (2009).

- M.F.G. Klein, M. Pfaff, M. Reinhard, J. Czolk, S. Valouch, E. Müller, A. Colsmann, D. Gerthsen and U. Lemmer. Nano-morphology studies of organic solar cells by low-energy electron transmission microscopy. (Poster) *SPIE Photonics Europe 2010*, Brussels, Belgium, April 16-19 (2010).

- M.F.G. Klein, A. Pütz, M. Pfaff, J. Czolk, M. Reinhard, E. Müller, A. Colsmann, D. Gerthsen and U. Lemmer. Highly efficient organic solar cells based on a PSBTBT: fullerene blend with extended absorption to the infrared. (Talk) *SPIE Photonics Europe 2010*, Brussels, Belgium, April 16-19 (2010).

- M. Pfaff, E. Müller and D. Gerthsen. Semi-empirical equation for electron scattering in thin films of light elements (Talk), *E-MRS Spring Meeting 2010*, Strasbourg, France, June 7-11 (2010).

- A. Colsmann, J. Czolk, M. Pfaff, M.F.G. Klein, M. Reinhard, U. Lemmer, D. Gerthsen, Morphology analysis of the absorbing layer in poly-(3-hexylselenophene) solar cells. *SPIE Optics + Photonics*, San Diego, USA, August 1-5 (2010).

- M. Pfaff, E. Müller, M. F. G. Klein, A. Colsmann, U. Lemmer and D. Gerthsen. Low-energy scanning electron transmission measurements of thin polymer films employed in organic solar cells (Poster) *Microscopy & Microanalysis*, Portland, USA, August 1-5 (2010).

- E. Müller, M. Pfaff, T. Volkenandt, H. Blank, F. Bleimund and D. Gerthsen. Quantitative scanning transmission electron microscopy at low electron energies. (Poster) *DPG Frühjahrstagung*, Dresden, Germany, March 13-18 (2011).

- M Pfaff, E. Müller, M. F. G. Klein, A. Colsmann, U. Lemmer and D. Gerthsen. Imaging the morphology of bulk-heterojunction based organic solar cells by low-energy scanning transmission electron microscopy (Talk). *4th International Symposium on Flexible Organic Electronics*, Thessaloniki, Greece, July 10-13 (2011).

- M. Pfaff, S. Hettler, E. Müller, M. F. G. Klein, A. Colsmann, U. Lemmer and D. Gerthsen. Imaging the morphology of organic solar cells by low-keV scanning transmission electron microscopy (Talk). *Microscopy Conference MC 2011*, Kiel, Germany, August 28-September 2 (2011).

- M. Pfaff, M. F. G. Klein, E. Müller, P. Müller, A. Colsmann, U. Lemmer, and D. Gerthsen. Nanomorphology of P3HT:PCBM-based Organic Solar Cells Analyzed by Low-Energy Scanning Transmission Electron Microscopy (Poster). *Microscopy & Microanalysis 2012*, Phoenix, USA, July 29-August 2 (2012). doi: 10.1017/S1431927612008021

- M. Pfaff, M. F. G. Klein, J. Subbiah, E. Müller, P. Müller, A. Colsmann, W. W. H. Wong, A. B. Holmes, U. Lemmer, D. J. Jones, and D. Gerthsen. Nanomorphology of fluorenyl hexa-peri-hexabenzocoronene-based absorber layers of organic solar cells (Talk). *The 15th European Microscopy Congress*, Manchester, United Kingdom, September 16-21 (2012).

- M. Pfaff, M. F. G. Klein, E. Müller, P. Müller, A. Colsmann, U. Lemmer, and D. Gerthsen. Low-energy scanning transmission electron microscopy studies of P3HT:PCBM-based organic solar cell absorber layers (Poster). *The 15th European Microscopy Congress*, Manchester, United Kingdom, September 16-21 (2012).

- M. Pfaff, M. F. G. Klein, E. Müller, P. Müller, A. Colsmann, U. Lemmer, and D. Gerthsen. Nanomorphology of P3HT:PCBM-based Organic Solar Cells Analyzed by Low-Energy Scanning Transmission Electron Microscopy (Poster). *CFN Summerschool 2012 on Nano-Energy*, Bad Herrenalb, Germany, September 14-17 (2012).

- T. Vokenandt, E. Müller, M. Pfaff and D. Gerthsen. Sample thickness determination by low-energy scanning transmission electron microscopy (Poster). *MC 2013*, Regensburg, Germany, August 25-30 (2013).

- M. Pfaff, E. Müller, T. Vokenandt and D. Gerthsen. Applications of low-energy scanning transmission electron microscopy for the investigation of carbon-based materials (Poster). *MC 2013*, Regensburg, Germany, August 25-30 (2013).

Awards and Scholarships

- Young Scientist Award at the EMRS conference 2010 in Strasbourg.

- MSA Presidential Student Award at the M&M conference 2012 in Phoenix.

- Doctoral scholarship from the 'Landesgraduiertenförderung' of the state Baden-Württemberg.

Danksagung

Zunächst möchte ich mich sehr herzlich bei Frau Prof. Gerthsen für die hervorragende Betreuung bedanken. Mit ihren kompetenten Ratschlägen und ihrem umfangreichen Fachwissen trug sie maßgeblich zum Gelingen dieser Arbeit bei. Danke auch für die Möglichkeit an vielen internationalen Tagungen teilzunehmen.

Ich danke Prof. Uli Lemmer für die Übernahme des Korreferates und die Unterstützung während meiner Diplomarbeits- und Promotionszeit. Sehr bedanken möchte ich mich außerdem für die einmalige Chance an der Solarenergieexkursion in Kalifornien teilzunehmen.

Erich Müller danke ich für die fachliche Unterstützung und die vielen ermutigenden Worte. Bei komplexen mikroskopischen und physikalischen Fragestellungen war er mit seinem umfangreichen Wissen immer mein erster Ansprechpartner. In den von ihm ins Leben gerufenen ddates der 'Laschies' gab es oft kontroverse, aber stets interessante Diskussionen und manchmal am Ende sogar Antworten auf die wir uns einigen konnten... ;-)

Michael Klein und Alexander Colsmann vom LTI danke ich für die gute Zusammenarbeit und die produktiven Diskussionen. Sie hatten immer wieder gute Ideen für weitere Experimente. Vor allem Michael danke ich für die vielen Stunden die er im Reinraum verbracht hat um Solarzellen für unsere Projekte herzustellen.

Besonders herzlich möchte ich mich bei Frau Sauter bedanken. Neben kompetenter Hilfe (nicht nur bei Verwaltungsangelegenheiten) gab es auch immer ein paar nette und aufmunternde Worte.

Ein großes Danke geht auch an meine Kollegen am LEM, die mich nicht nur fachlich unterstützen, sondern auch dafür sorgten, dass ich immer gerne an meine Promotionszeit zurück denken werde. Besonderen Dank haben hierbei die Mitglieder der LEM-Lauffreunde und natürlich die Backstubenbäcker verdient.

Bedanken möchte ich mich außerdem bei allen mit denen ich im Laufe meiner Promotion gerne zusammengearbeitet habe: Manuel Rheinhard, Jens Czolk, Hung Do, Stefan Höfle, Dominik Landerer, Felix Pasker, Benedikt Brenneis und Benjamin Schmitt-Hansberg.

I also thank David Jones for giving me the possibility to visit the Bio21 institute in Melbourne. Thanks also to Wallace Wong, and especially to Kuan Sun for the good cooperation and the great hospitality.

Ein weiterer Dank geht an meine Freunde und vor allem die BLAZ, ohne die das Studium nicht halb so lustig gewesen wäre :-)

Herzlicher Dank geht an meine Familie für die Unterstützung nicht nur während der Promotionszeit.

Zu guter Letzt ein riesiges Dankeschön an Philipp. Ich liebe dich!